



**Max-Planck-Institut für Metallforschung
Stuttgart**

***In Situ* Tensile Testing at the Limits of X-Ray
Diffraction – A New Synchrotron-Based Technique**

Jochen Böhm

Dissertation
an der
Universität Stuttgart

Bericht Nr. 149
Juni 2004

***In Situ* Tensile Testing at the Limits of X-ray Diffraction –
A new Synchrotron–Based Technique**

Von der Fakultät für Chemie der Universität Stuttgart
zur Erlangung der Würde eines Doktors der
Naturwissenschaften (Dr. rer. nat.) genehmigte Abhandlung

Vorgelegt von
Dipl.-Ing. Jochen Böhm
aus Stuttgart

Hauptberichter: Prof. Dr. phil. Eduard Arzt
Mitberichter: Prof. Dr. rer. nat. Alexander Wanner
Tag der mündlichen Prüfung: 08.06.2004

Institut für Metallkunde der Universität Stuttgart und
Max-Planck-Institut für Metallforschung Stuttgart

Stuttgart, Juni 2004.

Jochen Böhm

In Situ Tensile Testing at the Limits of X-ray Diffraction –
A new Synchrotron-Based Technique

Institute of Physical Metallurgy, University of Stuttgart and
Max-Planck-Institute for Metals Research Stuttgart, 2003.

130 pages, 56 figures, 6 tables.

Abstract

Stress measurements in crystalline solids by diffraction techniques are limited so far by measuring time, gauge volume or penetration depth. To improve this situation, a new synchrotron-based X-ray diffraction technique allowing *in situ* tensile tests has been developed. This method is capable of producing non-destructive stress- and strain information at the limits of X-ray diffraction. A new procedure for data acquisition was established which accelerates the measurements by orders of magnitude (seconds or minutes compared to several hours per data point). The technique reported in this work uses high-energy synchrotron radiation which penetrates the bulk within the range of several millimeters. It is shown experimentally that even coarse-grain materials can be investigated if an enlarged experimental setup is used. Such a setup allows for performing fast *in situ* experiments with excellent time and strain resolution. High-temperature *in situ* tensile tests have been performed on a TiAl-based material.

The method is capable of recording strains deep in the bulk as well as in ultrathin metallic films. A new approach is presented which uses tunable low-energy synchrotron radiation in combination with a CCD area detector. With this technique the evolution of the biaxial stress state in ultrathin film was measured during deformation with one single X-ray exposure per data point. *In situ* tensile tests were carried out on copper and gold films with film thicknesses below 100 nm. A high stress resolution in longitudinal- and transverse direction was achieved. The strain rate of tensile tests was increased at least by a factor of 6 compared to laboratory X-rays.

The high-energy experiments were carried out at the Hamburger Synchrotronstrahlungslabor (HASYLAB, Hamburg, Germany), low-energy X-rays were used at the dedicated MPI-MF beamline at ANKA (Angströmquelle Karlsruhe) located at the Forschungszentrum Karlsruhe (Germany).

Jochen Böhm

In situ Zugversuche am Limit der Röntgenbeugung – eine neue Synchrotronmethode

Institut für Metallkunde der Universität Stuttgart und
Max-Planck-Institut für Metallforschung Stuttgart, 2003.
130 Seiten, 56 Abbildungen, 6 Tabellen.

Kurzzusammenfassung

Spannungsmessungen in kristallinen Materialien mit Beugungsmethoden waren bisher beschränkt durch Messzeit, Beugungsvolumen oder Eindringtiefe. Um dies zu verbessern wurde eine neue auf Synchrotronstrahlung basierende Röntgenmethode entwickelt, die es ermöglicht *in situ* Zugversuche durchzuführen. Diese Methode ermöglicht es zerstörungsfrei Spannungen und Dehnungen am Limit der Röntgenbeugung zu messen. Die Messzeiten wurde um Größenordnungen verkürzt (Sekunden oder Minuten im Vergleich zu einigen Stunden pro Datenpunkt). Die in dieser Arbeit vorgestellte Technik verwendet hochenergetische Synchrotronstrahlung die Materialien bis in die Tiefe von mehreren Millimetern durchdringt. Es wird experimentell gezeigt, dass sogar grobkörnige Werkstoffe untersucht werden können wenn ein vergrößerter Versuchsaufbau verwendet wird. Mit solch einem Aufbau können schnelle *in situ* Experimente mit hervorragender Zeit- und Dehnungsauflösung durchgeführt werden. Hochtemperaturzugversuche wurden an einer TiAl-Legierung durchgeführt.

Die Methode ist weiterhin für Spannungsmessungen in ultradünnen Schichten geeignet. Für derartige Messungen wird ein neuer Ansatz gezeigt, bei dem abstimmbare niedrigenergetische Synchrotronstrahlung in Kombination mit einem CCD Flächendetektor zum Einsatz kommt. Damit konnte der Verlauf des biaxialen Spannungszustands in ultradünnen Schichten während der Verformung mit nur einer Röntgenaufnahme pro Datenpunkt gemessen werden. *In situ* Zugversuche wurden an Kupfer- und Gold Dünnschichten im Schichtdickenbereich unter 100 nm durchgeführt. Dabei wurde eine hohe Spannungsauflösung sowohl in Longitudinal- als auch in Transversalrichtung erreicht. Die Dehnrate wurde im Vergleich zur Laborquelle mindestens um den Faktor 6 erhöht.

Die Hochenergie-Experimente wurden am Hamburger Synchrotronstrahlungslabor (HASYLAB) durchgeführt, niedrigenergetische Röntgenstrahlung kam an der MPI-MF Beamline bei ANKA (Angströmquelle Karlsruhe) im Forschungszentrum Karlsruhe zum Einsatz.

Danksagung

Die vorliegende Arbeit wurde im Rahmen des Sonderforschungsbereichs SFB 381 am Institut für Metallkunde der Universität Stuttgart sowie am Max-Planck-Institut für Metallforschung in Stuttgart in der Zeit von Februar 2001 bis Januar 2004 in der Abteilung von Prof. Dr. Eduard Arzt angefertigt. Ich möchte mich bei Herrn Prof. Dr. Eduard Arzt für die Möglichkeit in seiner Abteilung zu promovieren und sein Interesse am Fortgang der Arbeit ganz herzlich bedanken.

Mein besonderer Dank gilt Prof. Dr. Alexander Wanner für die Übernahme des Mitberichts sowie die besonders interessante Themenstellung der Arbeit, die vielen fruchtbaren Diskussionen, seine unerschöpfliche Geduld und seine wertvollen Ratschläge, die zum Gelingen der Arbeit beigetragen haben. Die Strahlzeiten am Synchrotron werden mir sicherlich sehr lange in freudiger Erinnerung bleiben.

Bedanken möchte ich mich bei Dr. Ralph Spolenak sowie bei Patric Gruber für ihre Unterstützung und die gute Zusammenarbeit auf dem Gebiet der dünnen Schichten sowie die gute Atmosphäre während der Messzeiten bei ANKA.

Der Hochtemperatur-Zugofen wurde von Dr. Alain Jacques und Olivier Ferry zur Verfügung gestellt und während den Messungen bei DESY betrieben. Ich möchte mich für die gute Zusammenarbeit und die angenehme Zeit bei den Synchrotronmessungen ganz herzlich bedanken.

Mein Dank gilt weiterhin all denen, die mich bei den Messungen am Synchrotron in verschiedenster Hinsicht unterstützt haben: Prof. Dr. Helmut Clemens, Dr. Hermann Franz, Dr. Reinhard Kampmann, Dr. Nikolai Kaspar, Dr. Thomas Lippmann, Dr. Klaus-Dieter Liss, Dr. Adrian Rühm, Linda Sauter, Prof. Dr. Andreas Schreyer, Dr. Andreas Stierle, Dr. Leszec Weislak sowie Ralf Weigel.

Bei Natascha Tomic bedanke ich mich für die Präparation der Vollmaterial-Zugproben, sowie bei Dr. Thomas Wagner und Frank Thiele für die Herstellung der dünnen Metallschichten.

Ich möchte mich bei allen Kolleginnen und Kollegen der Abteilung Arzt für das angenehme Arbeitsklima und die sehr schöne Zeit am Max-Planck-Institut Stuttgart bedanken.

Contents

1 Introduction	1
1.1 Scope of this Dissertation	4
2 Literature	7
2.1 Theory of Elasticity	7
2.1.1 Terms and Definitions	7
2.1.2 Orientation Dependence of Young's modulus	10
2.1.3 Polycrystal Deformation	11
2.2 Stress and Strain Analysis by X-ray Diffraction	12
2.2.1 X-Ray Sources	13
2.2.2 Why Synchrotron X-rays?	15
2.2.3 Fundamentals of X-ray Strain Determination	16
2.2.4 Biaxial Residual Stress Analysis - The $\sin^2\psi$ Method	20
2.2.5 Measurement of Lattice Strains in the Bulk by High-Energy X-Rays	22
3 Methodology	25
3.1 Stress Evolution in the Bulk – High-Energy $\sin^2\phi$ Method	25
3.1.1 Conventional Setup	25
3.1.2 Advanced Approach - Enlarged Setup	29
3.2 Stress Evolution in Ultrathin Films – Low-Energy $\sin^2\phi$ Method	33
3.3 Strain Evaluation Procedure	38
3.4 Measurement Errors	41
4 Experimental	43
4.1 Synchrotron X-Ray Sources	43
4.1.1 DESY BW5 Beamline	43
4.1.2 DESY PETRA 2 Beamline	44
4.1.3 ANKA MPI-MF Beamline	45
4.2 High-Energy Experiments on Bulk Samples	45
4.2.1 Room Temperature Tensile Tests	45
4.2.2 Furnace	46
4.2.3 Experimental Setups Used	48
4.2.4 Materials Investigated	50
4.3 Low-Energy Experiments on Thin Films	55
4.3.1 Sample Fabrication and Characterization	55
4.3.2 Experimental Setup Used	58
4.3.3 Residual Stress Measurements - $\sin^2\psi$ Method	59

4.3.4 Stress Evolution - $\sin^2\varphi$ Method.....	60
5 Results.....	63
5.1 High-Energy Experiments – Bulk Materials	63
5.1.1 Cu/Mo Composites – Methodology Confirmation.....	63
5.1.2 Ti-Based Material	64
5.1.3 γ -TiAl Alloys – Conventional vs. Enlarged Setup	66
5.1.4 γ -TiAl Alloys – High-Temperature Experiments.....	70
5.1.5 NiAl Polycrystals.....	73
5.2 Low-Energy Experiments – Thin Films	75
5.2.1 Au Thin Films.....	75
5.2.2 Cu Thin Films.....	82
5.3 Summary of Results.....	88
6 Discussion	89
6.1 Methodology.....	89
6.2 Material Aspects	94
6.2.1 Ti-Based Material	94
6.2.2 γ -TiAl.....	95
6.2.3 NiAl	99
6.2.4 Plasticity of Thin Cu and Au Films	100
7 Conclusions.....	103
8 Outlook	105
9 References.....	107
10 Appendix.....	115
10.1 Appendix A.....	115
10.2 Appendix B.....	117
10.3 Appendix C.....	117
10.4 Appendix D.....	118
10.5 Appendix E.....	119
11 Deutsche Zusammenfassung.....	121
11.1 Grundlagen	121
11.1.1 Grundlagen der röntgenographischen Spannungsmessung.....	121
11.1.2 Biaxiale Eigenspannungsmessung – Die $\sin^2\psi$ Methode	122
11.1.3 Messung von Gitterdehnungen mit hochenergetischer Röntgenstrahlung	123
11.2 Methodik.....	124
11.2.1 Spannungsentwicklung in Vollmaterialien – Die Hochenergie- $\sin^2\varphi$ Methode ...	124

11.2.2 Spannungsentwicklung in ultradünnen Schichten – Die Niedrigenergie- $\sin^2\varphi$ Methode	126
11.3 Experimente.....	128
11.4 Ergebnisse.....	129

List of symbols and abbreviations

A	area [m ²]
ANKA	Angströmquelle Karlsruhe
APS	Advanced Photon Source
b	axis intercept of the $\sin^2\psi$ fit
B	axis intercept of the $\sin^2\phi$ fit
CCD	Charge Coupled Device
C_{ij}	reduced stiffness matrix
C_{ijkl}	stiffness matrix
d	lattice spacing [nm]
D	diffraction ring diameter [m]
DESY	Deutsches Elektronensynchrotron
E	Young's modulus [GPa]
ESP	Electronic Stability Program
EXAFS	Extended X-ray Absorption Fine Structure
F	force [N]
FFT	Fast Fourier Transformation
FIB	Focused Ion Beam
FWHM	Full Width Half Maximum
HASYLAB	Hamburger Synchrotronstrahlungslabor
HIP	Hot Isostatic Pressing
hkl	Miller Indices
IDL	Image Describing Language, programming language of RSI Software
l	length [m]
L	specimen-to-detector distance [m]
LASER	Light Amplification by Stimulated Emission of Radiation
LVDT	Linear Variable Differential Transducer
m	slope of the $\sin^2\psi$ fit
M	slope of the $\sin^2\phi$ fit
MEMS	Micro Electro-Mechanical System
<i>MPI-MF</i>	Max-Planck-Institute for Metals Research
n	integer value [-]
NEMS	Nano Electro-Mechanical system

PID	Proportional Integral Derivative control, automatic regulation
POI	Points Of Interest
R	diffraction ring radius [m]
SDEV	Standard Deviation
SEM	Scanning Electron Microscope
S_{ij}	reduced compliance matrix
S_{ijkl}	compliance matrix
TZM	Titanium-Zirconium-Molybdenum
UHV	Ultra-High Vacuum
x_m	x-coordinate of the diffraction ring center [pixel]
XSA	X-ray Stress Analysis
y_m	y-coordinate of the diffraction ring center [pixel]
Z	atomic mass [atomic mass units]
α	direction cosine [-]
β	direction cosine [-]
δ	detector inclination angle [°]
ε	strain [-]
ε_{ij}	strain tensor
γ	direction cosine [-]
φ	azimuthal angle [°]
λ	Wavelength [nm]
ν	Poisson's Ratio [-]
θ	Bragg Angle [°]
σ	stress [MPa]
σ_{ij}	stress tensor

1 Introduction

Components for lightweight applications are designed by engineers in order to improve the structure with respect to strength and weight. Such an optimized component can reduce both economical and environmental costs, especially in applications where the fuel efficiency depends highly on the total mass of the construction, e.g. in the car or aerospace industry. The first step in the optimization process is to analyze how the internal stresses and strains act on the component. If the stress state is known, it is possible to decide if a suitable material was selected and to find out where the component is possibly loaded over the design limit or where the load within the structure is relatively low. Afterwards the component is redesigned by adding material to or removing material from the structure. This is usually done by finite element calculations. If the material is thermo-mechanically treated during production, residual stresses have to be considered which have to be incorporated in the calculations. Residual stresses can be beneficial or detrimental for a component, depending on the type of load state. For example, compressive residual stresses are introduced by shot peening in order to increase the fracture load for a component loaded by tensile stresses. If the full mechanical potential of the selected material has to be used in the construction, such stresses must be considered. Residual stresses can be measured non-destructively by X-ray and neutron diffraction techniques (see Noyan and Cohen (1987)) or destructively, for example by the hole drilling method (see Kockelmann and Schwarz (1993)). In the next step the evolution of stresses during loading is important in order to further optimize the design of the construction.

Since the measurement of stresses within the bulk should be non-destructive, diffraction techniques are the methods of choice. These techniques allow the lattice spacing of differently oriented grain subsets to be determined by making use of the Bragg scattering of X-rays and neutrons in the material. While the penetration depth of conventional X-rays is in the order of several microns limiting the measurements to the near surface of materials, the penetration depth of neutrons is in the order of several centimeters. Strain measurements in the bulk using neutron diffraction techniques have been performed extensively i.e. by Lorentzen et al. (1998) and by Clausen et al. (1999). They also report on how the stress state can be estimated by the elastic constants and by model calculations using appropriate grain interaction models. The determination of the stress state from the measured elastic lattice strains is crucial since the selectivity of diffraction techniques for specific grain orientations makes the conversion of

elastic lattice strains to an overall stress state a non-trivial task. Since many high-performance alloys are multiphase materials, their load-bearing capacity is controlled by the internal load transfer between the constituent phases. Clausen (1997) reports a numerical model which allows the polycrystal deformation in multiphase materials to be characterized based on the results of neutron diffraction experiments (see also chapter 2.1.3).

An experimental measurement of the load partitioning between individual phases can give a wealth of information about the micromechanics going on during deformation. While the classical neutron techniques are capable of measuring phase-dependent lattice strains within the bulk, they are, however, time consuming due to their long data acquisition times of several hours per data point; this makes them not very suitable for studying time-dependent phenomena. Faster measuring techniques are thus required. It has been shown by Daymond and Withers (1996) and by Korsunsky et al. (1998) that strain measurements in the bulk are feasible by using high-energy synchrotron X-rays exhibiting a much higher photon flux and much shorter data acquisition times, whereas the penetration depth is comparable to that of neutrons. This high-energy X-ray technique is still under development, and it is one aim of this thesis to further increase its time and strain resolution.

The evolution of stresses also plays an important role in mechanically loaded thin film systems which are widely used by the microelectronics industry in microchips, micro- and nano electromechanical systems (MEMS/NEMS), optical devices, etc. Other examples for applications are integrated circuits on flexible substrates (e.g. for polymer displays, see Kuhlmann and Rink (1998), Gelinck et al. (2004), or wearable computers), sensor elements (airbag sensors or ESP sensors in the car industry), optical mirrors for broadband network switches (see Koloder (2002)), or protective films against abrasion on mechanically loaded components. The system Cu/polyimide is of special interest to the semiconductor packaging industry. Another field of current industrial development are shape-memory devices which are made using sputtered films on polyimide substrates. The combination of these two material types may be highly advantageous since the shape-memory metallization stiffens and recovers the shape when the device is heated, whereas the polyimide responds to heat by becoming more compliant and thus will tend to recover the shape on cooling. Both material types are very compatible and could form a new class of highly rugged microactuators capable of

providing large forces and tiny displacements. Furthermore, such systems could be made biocompatible, resistant against acids and serviceable in liquids (see Grummon and LaGrange (2000)).

The reliability of micro- and nanometer-scale devices is affected by large mechanical stresses which may occur during fabrication and service. Such stresses can result from growth processes, thermal mismatch or external loading. In metallic components, these stresses are partly relaxed by yielding and creep but the deformation mechanisms are sensitive to the dimensions of the components. Due to this importance there is a huge scientific activity in the research field of mechanical properties of thin film systems. In recent years, such size effects on the mechanical properties of metallic materials have been studied extensively and it has been shown that the mechanical properties of metallic thin films can differ significantly from the bulk values (i.e. Freund (1987), Nix (1989), Sanchez and Arzt (1992), Venkatraman and Bravman (1992), Thompson (1993)). Much progress has been made towards understanding the deformation mechanisms in the micrometer regime, mostly based on experimental investigations performed on continuous films with varying thicknesses. It would be of great interest from both fundamental and engineering points of view to extend the experimental investigations down to the nanometer regime. Thus, there is still an ongoing challenge for measuring mechanical properties of metal films as thin as possible. Unlike other commonly used techniques like the substrate curvature method, *in situ* X-ray tensile tests can be performed at constant temperature, which simplifies the interpretation of the results tremendously compared to the stress-temperature cycles obtained by applying strain by the variation of temperature.

The commonly used *in situ* X-ray tensile testing technique is based on the $\sin^2\psi$ method (see chapter 2.2.4) and has been shown to work very well for metal films with thickness in the micrometer range. Serious experimental problems arise, however, for films considerably thinner than 1 μm . First of all, the X-ray counting times required per data point increase to an impractical level as the gauge volume is decreased. Second, the signal-to-noise ratio of the diffraction peaks becomes unfavorable, which is closely related to the fact that the amorphous structure of the polyimide substrate gives rise to considerable scattering background. Hence, results from X-ray measurements combined with *in situ* tensile tests have so far been reported

only for films thicker than about 300 nm. The few stress-strain curves published for thinner metal films were obtained by either performing tensile tests on very thin (3.5 μm) polyimide samples with and without film and back-calculating the film stress from the small difference between the two macroscopic stress-strain curves obtained in this way by Kang et al. (1997) and Tregilgas and Strumpell (1998), or by performing uniaxial tensile tests on free-standing films using a special MEMS device into which the specimen is integrated (see Saif et al. (2002), Haque and Saif (2002)). These approaches suffer, however, from the following setbacks: The back-calculating approach ignores that the stresses developing in the thin film during deformation of the composite are biaxial due to the mismatch in Poisson's ratios between film and substrate. Any uncertainties about the thickness and the elastic and anelastic properties of the substrate also affect the results. The MEMS device designed by Saif et al. (2002) is an excellent tool for *in situ* TEM and SEM studies of deformation behavior, but sample fabrication is complicated and testing of thin films on macroscopic substrates is not possible. The latter case is of special relevance as most thin films used in actual applications are deposited on substrates. It is therefore desirable to extend the X-ray stress measurement techniques to thinner films.

1.1 Scope of this Dissertation

In this thesis, the recently achieved progress in the determination of loading stresses measured by a new synchrotron X-ray diffraction technique, the so-called $\sin^2\phi$ method (not to be mistaken for the $\sin^2\psi$ method), is described in detail. The $\sin^2\phi$ method allows for measuring the complete stress tensor by one single X-ray exposure during *in situ* tensile tests. The focus is on determining stresses and strains at the diffraction limit of X-rays in order to obtain nondestructive information about the mechanical behavior deep in the bulk of materials as well as in ultrathin films. The broad spectrum of applications for this new X-ray technique is shown on typical sample materials, relevant for fundamental as well as applied research. The results are discussed concerning the formation of stresses due to uniaxial loading in both homogeneous and heterogeneous metallic bulk materials and thin films. The research was performed in order to get a more complete picture of the micro- and nanomechanics during deformation. The focus was on developing a new technique for determining load stresses during *in situ* tensile tests performed at the limits of X-ray diffraction, which means that the material under investigation is either at the thickness limit of the penetration depth of X-rays

or the volume content is so small that only very weak diffracted intensity is obtained. The latter is especially the case for an ultrathin film in the thickness range below 100 nm. In this thickness range no *in situ* X-ray tensile tests have been reported in the literature so far.

Stress and strain measurements in materials based on X-ray diffraction are usually performed using the $\sin^2\psi$ method which requires rotation of sample and detector and is thus very time consuming. Since the penetration depth of X-rays of a laboratory source is limited to a few microns, this technique is only capable of measuring the strain state either at or near the surface of bulk materials or inside thin films. In the literature, some work can be found describing the determination of the strain state in the bulk of materials using neutron diffraction (see Clausen et al. (1999), Lorentzen et al. (1998)). While good results are obtained by this method it is, however, very time consuming and therefore not very suitable for fast *in situ* tensile tests on bulk samples and not applicable for measuring strains in thin films. The $\sin^2\phi$ method developed in this work makes use of some technological developments which became available in the last few years: (1) high-flux, tunable synchrotron X-ray sources providing high-energy X-rays which penetrate the bulk and low-energy X-rays for stress measurements in thin films; (2) large high-resolution area detectors, and (3) capacity for processing and storage of large amounts of data. While the $\sin^2\phi$ method itself is not new for high-energy applications measuring the strain state in the bulk, this is the first time it has been applied to thin films.

Experiments on different sample materials have been performed during this work. Besides methodological developments, the interest of research was on studying the load partitioning in the bulk of several multiphase alloys, mainly TiAl and NiAl alloys, as well as on studying the elastic-plastic behavior of thin Cu and Au films, especially in the film thickness range below 100 nm. The variety of different materials observed by the new X-ray method shows its wide applicability for *in situ* stress- and strain measurements and its relevance for future research in this field.

2 Literature

This chapter gives a short survey on the recent state of X-ray stress analysis (XSA). Primarily, the basics of XSA with respect to the theory of elasticity and X-ray physics are briefly reviewed. Thereafter the fundamentals of X-ray stress- and strain analysis are introduced with a focus on the standard X-ray stress measurement technique, the $\sin^2\psi$ method. The intention is to focus only on those parts which are of importance for this thesis. For a comprehensive background the interested reader is referred to the textbook of Noyan and Cohen (1987).

2.1 Theory of Elasticity

In the following, the fundamental concepts of linear elasticity are discussed. These general terms and definitions will be used in different chapters of this thesis for various types of stress analyses. A comprehensive review can be found in the book of Timoshenko and Goodier (1951).

2.1.1 Terms and Definitions

When a solid material is deformed by an external stress $\sigma = F / A$ (F = Force, A = cross-sectional area), the resulting strain¹ $\varepsilon = \Delta l / l_0$ (Δl = elastic elongation, l_0 = initial length) yields a deformation of the sample. In the case of linear elasticity, the strain is reversible, i.e., it goes back to zero if the load is released. Within a uniaxial tensile test, the linear elastic behavior for an isotropic material is described by Hooke's Law:

$$\sigma = E \cdot \varepsilon, \quad (2.1)$$

where σ denotes the stress, E the Young's modulus and ε the strain.

To describe the complete stress state in a solid, nine stress components are required in general, six of which are independent. The stress components acting on the normal directions are called normal stresses, where the in-plane components are called shear stresses. The complete stress state is described by a second-rank tensor, σ :

¹ The definition of strain in this content means the "engineering strain" whereas the reference length l_0 denotes the initial length of the sample. By using the actual length l instead of l_0 the "true strain" is obtained.

$$\sigma_{ij} = \begin{pmatrix} \sigma_{11} & \sigma_{12} & \sigma_{13} \\ \sigma_{12} & \sigma_{22} & \sigma_{23} \\ \sigma_{13} & \sigma_{23} & \sigma_{33} \end{pmatrix}. \quad (2.2a)$$

By analogy, a second rank strain tensor can be defined:

$$\varepsilon_{ij} = \begin{pmatrix} \varepsilon_{11} & \varepsilon_{12} & \varepsilon_{13} \\ \varepsilon_{12} & \varepsilon_{22} & \varepsilon_{23} \\ \varepsilon_{13} & \varepsilon_{23} & \varepsilon_{33} \end{pmatrix}. \quad (2.3a)$$

The Young's modulus is defined as the curvature of the potential energy curve at the bottom of the potential well and it is therefore independent of the sign of stress (compression or tension). It is only dependent on the variation of the interatomic forces with the distance from the equilibrium position and thus a material property. However, it is slightly affected by heat treatment or plastic deformation for some materials. Furthermore it changes with the direction of the crystal lattice since the lattice spacing between the atoms and therefore the variation of the potential energy is different along various crystal directions, which causes *elastic anisotropy*. Since a single crystal consists of periodically arranged unit cells, the Young's modulus will be constant along a given direction. Hooke's law for an anisotropic material is then of the following form:

$$\sigma_{ij} = C_{ijkl} \cdot \varepsilon_{kl}, \quad (2.4)$$

or in the inverted form:

$$\varepsilon_{ij} = S_{ijkl} \cdot \sigma_{kl}. \quad (2.5)$$

C_{ijkl} and S_{ijkl} obtain the stiffness and compliance values of the crystal. Both are symmetric fourth rank tensors. Usually, the stiffness and compliance terms are expressed with two subscripts instead of four. This notation is obtained by combining the first and the last pair of suffixes into one according to the following rules: 11 \rightarrow 1; 22 \rightarrow 2; 33 \rightarrow 3; 23 or 32 \rightarrow 4; 31 or 13 \rightarrow 5; 12 or 21 \rightarrow 6. The resulting C_{ij} and S_{ij} matrices are symmetric 6 \times 6 matrices containing 36 components each. In general, 21 independent components or elastic constants are required to describe the elastic behavior of an anisotropic crystal. A special crystal symmetry or texture can further affect the number of independent constants. For a cubic single crystal, only three independent constants are needed and the stiffness matrix becomes

$$C_{ij} = \begin{pmatrix} C_{11} & C_{12} & C_{12} & 0 & 0 & 0 \\ C_{12} & C_{11} & C_{12} & 0 & 0 & 0 \\ C_{12} & C_{12} & C_{11} & 0 & 0 & 0 \\ 0 & 0 & 0 & C_{44} & 0 & 0 \\ 0 & 0 & 0 & 0 & C_{44} & 0 \\ 0 & 0 & 0 & 0 & 0 & C_{44} \end{pmatrix}. \quad (2.6)$$

Similarly, the compliance matrix has the form

$$S_{ij} = \begin{pmatrix} S_{11} & S_{12} & S_{12} & 0 & 0 & 0 \\ S_{12} & S_{11} & S_{12} & 0 & 0 & 0 \\ S_{12} & S_{12} & S_{11} & 0 & 0 & 0 \\ 0 & 0 & 0 & S_{44} & 0 & 0 \\ 0 & 0 & 0 & 0 & S_{44} & 0 \\ 0 & 0 & 0 & 0 & 0 & S_{44} \end{pmatrix}. \quad (2.7)$$

The stiffness matrices for other crystal structures such as hexagonal and tetragonal lattices are given in Appendix B.

For an isotropic material subjected to a three-dimensional state of stress the strains ε_i are obtained from the stresses σ_i , the Young's modulus E and the Poisson's ratio ν in the following way:

$$\varepsilon_1 = \frac{1}{E}(\sigma_1 - \nu\sigma_2 - \nu\sigma_3), \quad (2.8a)$$

$$\varepsilon_2 = \frac{1}{E}(\sigma_2 - \nu\sigma_1 - \nu\sigma_3), \quad (2.8b)$$

$$\varepsilon_3 = \frac{1}{E}(\sigma_3 - \nu\sigma_1 - \nu\sigma_2), \quad (2.8c)$$

i.e., only two elastic constants are sufficient to describe the linear elastic behavior of an isotropic² solid.

² Polycrystals are regarded as "quasi isotropic" if they exhibit no texture. In the presence of texture appropriate elastic constants have to be considered.

2.1.2 Orientation Dependence of Young's modulus

The Young's modulus depends on the direction $[hkl]$ in the crystal along which the crystal is observed. For a cubic single crystal one obtains:

$$\frac{1}{E_{hkl}} = S_{11} - [2(S_{11} - S_{12}) - S_{44}] \cdot (\alpha^2 \beta^2 + \alpha^2 \gamma^2 + \beta^2 \gamma^2), \quad (2.9)$$

where α , β , and γ denote the direction cosines between the coordinate axes and the $[hkl]$ direction. For a hexagonal crystal, one obtains:

$$\frac{1}{E_{hkl}} = S_{11}(1 - \gamma^2)^2 + S_{33}\gamma^4 + (2S_{13} + S_{44})\gamma^2(1 - \gamma^2), \quad (2.10)$$

where γ denotes the direction cosine between the z axis $[001]$ and the $[hkl]$ direction. The relationships for other crystal structures can be found i.e. in the book by Kelly and Groves (1970) or in the work by Wieder (1997). The orientation dependence of Young's modulus for a hexagonal titanium single crystal is shown graphically in Figure 2.1.

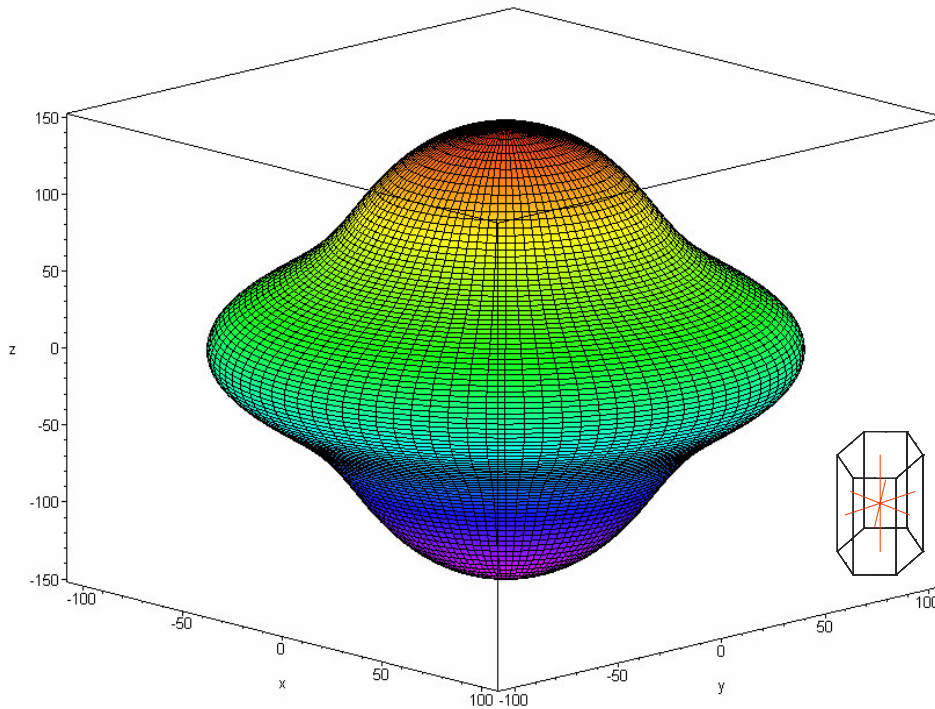


Figure 2.1: Orientation dependence of Young's modulus for a hexagonal titanium single crystal. The rotational symmetric representation surface was calculated for each hkl orientation according to Equation (10.4) given in Appendix C using the computer algebra program Maple V (all units in GPa).

2.1.3 Polycrystal Deformation

If the crystallites in a polycrystal are randomly oriented, its global elastic behavior is considered as *quasi isotropic*. After Kröner (1958) it is then possible to calculate the Young's modulus from the moduli of the individual orientations. Two extreme cases of weighting derive from Voigt and Reuss. The Voigt average is calculated on the assumption of constant local strains and is an average of the stiffnesses (see Voigt (1928)). The Reuss average is based on the assumption of constant local stresses and averages the compliances (see Reuss (1929)). For a cubic material one obtains the Young's modulus according to the Voigt model using:

$$E_V = \frac{(C_{11} + 2C_{12})(C_{11} - C_{12} + 3C_{44})}{2C_{11} + 3C_{12} + C_{44}}, \quad (2.11)$$

and according to the Reuss model with:

$$E_R = \frac{1}{5}(3S_{11} + 2S_{12} + S_{44}). \quad (2.12)$$

Diffraction measurements always yield elastic lattice *strain* components in specific directions for the individual grains which participate in diffraction. These grains have lattice plane normals in the same direction. Because only specific grains are selected by the measurement, problems arise in the interpretation of the measurement with respect to the global *stress* state in the sample. Converting specific elastic lattice strains to stresses is a non-trivial and often impossible task. The simplest way to estimate the stress state is to multiply the measured lattice strains with the Young's modulus for the specific grains, the so-called diffraction- or X-ray elastic constants. This calculation assumes that the stress state in the sample is uniaxial. A three-dimensional stress state can also be calculated by a more generalized Hooke's Law, however, still assuming an isotropic material. Intergranular strains will therefore strongly influence the results.

Modelling grain interactions has extensively been done in the past based on the results obtained by the $\sin^2\psi$ X-ray method (see chapter 2.2.4). Welzel (2002) reports studies which were performed on thin metal films using the Vook and Witt grain interaction models. Another way has been shown by Clausen (1997) based on lattice strain measurements by neutron diffraction using micro-mechanical polycrystal deformation models. The modelling is based on the deformation of the constituents of the polycrystal using the Taylor model (see Taylor (1938)), the Sachs model (see Sachs (1928)), and the self-consistent Hutchinson model

(see Hutchinson (1970)). Whereas in the Taylor model all grains are subjected to the same strain, the grains are subjected to the same stress in the Sachs model. The coupling between all grains is very stiff in both models and they represent the upper- and lower-bound for polycrystal plasticity like the Voigt- and Reuss models for the elastic stiffnesses of a polycrystal. Although the implementation of an appropriate algorithm is straightforward for the Taylor and Sachs models, the implementation laborious because the lattice rotations in the grains must be calculated for both models based on the number of active slip systems in the grains. This number differs considerably for the two models and it has been shown clearly by Clausen (1997) that the resulting grain rotations are completely different for the two models. In that work it was also shown that neither of the models is practical for correlating elastic lattice strains with neutron diffraction measurements. The stresses calculated in this way are thus only an estimate. However, the results of Clausen (1997) show that the models can be successfully used to predict deformation textures for large strains because the texture development is not influenced by the underlying micro-mechanics and elastic anisotropy is negligible at large strains. If texture development was also accounted for, Clausen (1997) has shown that the self-consistent Hutchinson model showed comparable results, especially if empirical assumptions like specific hardening laws for particular orientations are implemented in the model.

In this thesis, stresses are calculated from lattice strains only for the special case of a fiber-textured polycrystalline thin film. This will be shown in chapter 2.2.4 by the $\sin^2\psi$ method and in chapter 3.2 by the new low-energy $\sin^2\phi$ method. In all other cases stresses will be solely estimated by the simplest model using the X-ray elastic constants of the material. It is not the intension of this work to model grain interactions and load partitioning between different phases of the material. Moreover the methodological development for measuring lattice strains towards the achievable limit of X-ray diffraction will be pushed forward in order to deliver accurate experimental data which can enter the existing models in order to get a more complete picture of the physical processes going on during deformation.

2.2 Stress and Strain Analysis by X-ray Diffraction

In the following, the principles of stress and strain analysis by X-ray diffraction methods will be briefly assessed. After a short review of X-ray sources, the fundamentals of X-ray strain

determination will be introduced and the standard X-ray technique for biaxial stress analysis, the $\sin^2\psi$ technique will be explained. Thereafter, a short literature review will be given with respect to strain measurements within the bulk by high-energy X-rays.

2.2.1 X-Ray Sources

X-rays have been widely used for many applications since W.C. Röntgen observed this type of radiation in the year 1895 (see Röntgen (1895)). The first rotating anode was introduced by Clark in the year 1934. This kind of radiation source yields a higher photon flux than a conventional X-ray tube and is widely used today for X-ray experiments in the laboratory. In a rotating anode electrons are decelerated from typical energies of about 50 keV and deflected within the field of the atomic nuclei. During this process they emit electromagnetic radiation, the so called "*Bremsstrahlung*" (continuous X-ray radiation which is emitted when electrons are decelerated within a material). The anode rotates to decrease the heat load because of the electron bombardment. A rotating anode produces characteristic radiation as a result of the ionization of the K- and L-shells and the subsequent replacement of the holes by electrons originating from higher shells of the anode material. In consequence a line spectrum is obtained which is not tunable. Most of the energy is lost by heating - only about 0.1% of the electron energy is transformed into electromagnetic radiation. This limits the maximum power of rotating anodes to 20 – 50 kW.

According to Gehlen (2003), the principle of a synchrotron was developed in 1945 by E.M. McMillan in California and V. Veksler in the former Sowjet Union. One year later, a little 8 MeV synchrotron was built in England. At the beginning, first generation synchrotron radiation sources were built as particle accelerators mainly used for high-energy physics where accelerated particles emitted X-rays as an unwanted by-product. Today, second and third generation synchrotrons are built to produce solely X-ray radiation. A synchrotron can be operated with electrons or positrons, which are produced by a hot cathode and accelerated by a linear accelerator (LINAC). Positrons are produced from electrons which are accelerated on a tungsten target, the so-called converter. The particles are further accelerated within the booster and then injected into the storage ring where they travel with constant velocity almost at the speed of light. The storage ring is built as a polygon with several linear parts and bending magnets which force the particles to move along a closed path. When the direction of

accelerated particles is changed, energy is set free in form of radiation. A synchrotron produces a wide spectrum of electromagnetic radiation ranging from visible light to hard X-rays. This polychromatic radiation is called white X-ray radiation. The X-ray beam, generated by the bending magnets, has a very small angular divergence. The reason for this is the *Doppler effect*, which is very pronounced as the accelerated particles move almost as fast as the electromagnetic radiation they emit. For electrons the angular divergence is less than 0.5 mrad when the storage ring is operated at energies greater than 1 GeV which is typical for modern synchrotron radiation sources.

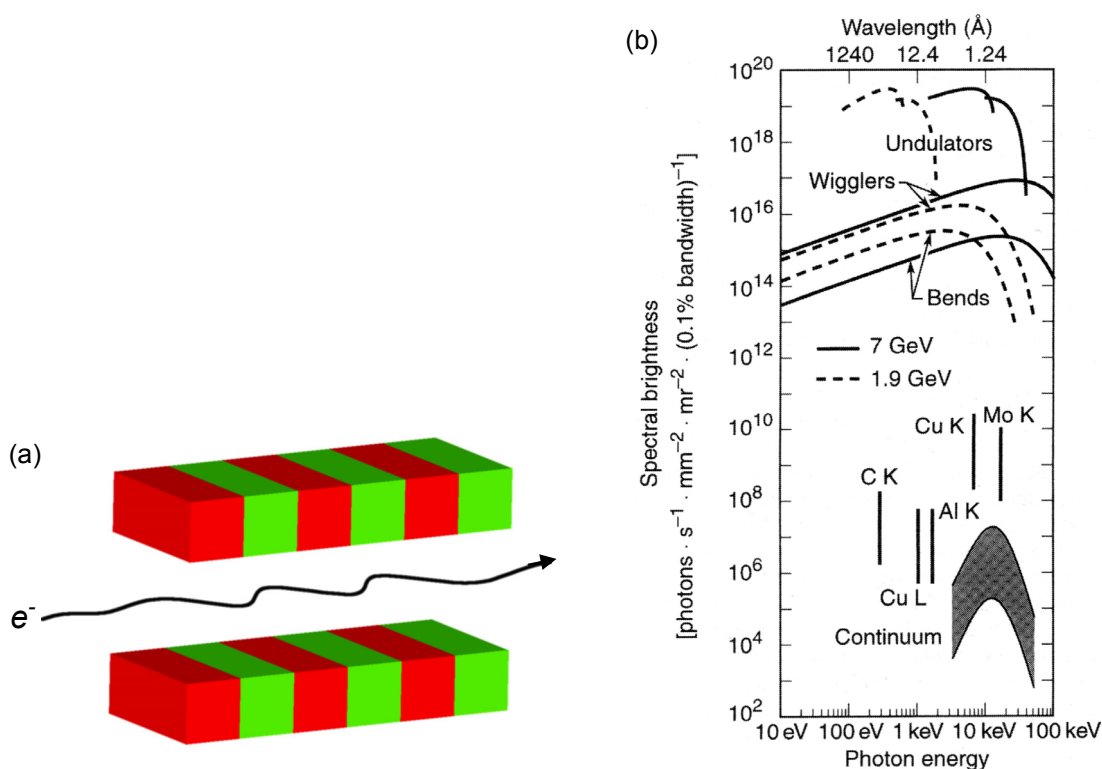


Figure 2.2: (a) Schematic of an undulator insertion device (ID). Small permanent magnets force the electrons to pass along an undulating path. (b) Spectral brightness of typical synchrotron sources using bending magnets, undulator- or wiggler-IDs. For comparison several laboratory sources are also shown. Graphic source: Thompson and Vaughan (2003)

The quality of an X-ray beam is determined by the *photon flux*, which is defined as the number of photons per time and relative energy bandwidth. The photon flux normalized to the angular divergence is called *brightness*. The *brilliance* is defined as the brightness normalized to the area of the radiation source:

$$\text{brilliance} = \frac{\text{number of photons}}{\text{sec} \cdot \text{mrad}^2 \cdot 0.1\% \text{ energy bandwidth}} \quad (2.13)$$

In modern synchrotrons the flux is increased considerably with the help of insertion devices (IDs). An undulator ID is built of structures which form an array of small magnets forcing the electrons to pass along an undulating, wavy path (see a). The magnets in an undulator ID have a relatively low magnetic field and are spaced close together. The low magnetic field of undulators narrows the cone of radiation, allowing the radiation from each pole to interfere constructively thus producing a much more brilliant X-ray beam compared to that of a bending magnet. This interference creates peak intensities at certain energies as well as high-brilliance beams which are tunable in wavelength. In a wiggler ID, a high magnetic field and a larger distance between the individual magnets produces very intense radiation over a wide spectrum as shown in b, see also Advanced Photon Source (2003) and European Synchrotron Radiation Facility (2003).

2.2.2 Why Synchrotron X-rays?

Most work on stress analysis published so far is based on the diffraction of X-rays or thermal neutrons. Residual stress analysis is carried out routinely using laboratory X-ray sources. As the penetration depth of characteristic X-rays from a laboratory source is in the range of several microns, stress analysis works fine for near-surface investigations, coatings or films on a substrate. If one is interested in the evolution of load stresses in the material, this limited penetration depth is the major problem since the stress state at the surface of a sample can be completely different to that within the bulk. Neutrons can penetrate the bulk of materials in the range of several centimeters and most work concerning the evolution of stresses is based on neutron diffraction. However, measurement times are quite long (in the range of several hours per data point) due to the inherently low interaction of neutrons with mass. Neutron diffraction techniques are therefore not practical for fast *in situ* experiments. In order to overcome this limitation high-energy synchrotron X-rays can be used. Synchrotron radiation in the energy range above 60 keV can penetrate materials with a thickness of several millimeters or centimeters. Due to the high flux of 3rd generation synchrotron sources measurement times can be reduced to several seconds or minutes per data point. In Table 1 on

page 26 the half-value thicknesses of X-rays with different photon energies are shown for several elements.

The available gauge volume limits the scattered intensity of X-rays at the other end of the accessible thickness length scale, since one limitation for conventional X-ray stress analysis techniques using laboratory X-ray sources is the film thickness itself. In the film thickness range below 200 – 300 nm the intensity of the diffracted beam is very weak yielding a very low signal-to-noise ratio. This leads to very long measuring times and limits *in situ* experiments to a certain minimum film thickness which depends on the sample material and the X-ray source. The high flux of a synchrotron source can help to push the film thickness limit down to the range of several nanometers. This makes possible *in situ* tests on ultrathin films with high stress- and time resolution.

2.2.3 Fundamentals of X-ray Strain Determination

Different length scale levels have to be distinguished in order to describe residual stresses in a material. So-called type-I stresses as defined by Macherauch and Kloos (1986) occur due to macroscopic reasons, e.g. stresses in a bulk solid originating from surface- or thermal treatments, or stresses in thin films caused by film growth during annealing. Coherency stresses in epitaxial films are a special case of such stresses. Stresses occurring on a crystallite scale level are so-called type-II stresses. They differ between individual grains due to grain interactions arising from constraints at the grain boundaries as well as elastic anisotropy which varies from one grain to another. On a microscopic subgrain scale, so-called type-III stresses occur on a crystal lattice level due to crystal defects like dislocations or point defects.

At this point it should be emphasized that direct stress measurements are not possible; only elastic strain can be measured directly. Internal strains are typically measured non-destructively by diffraction methods. The analysis of the stress state of a crystalline sample measured by diffraction can basically be simplified to the measurement of angles at which the maximum diffracted intensity occurs when the specimen is irradiated by X-rays or neutrons.

The kinematic theory³ or the simple geometric representation by Bragg's law is sufficient to describe the measurement of lattice spacings of polycrystals: Constructive interference is only observed if the pathlength difference between incident beam and reflected beam is equal to an integer number of wavelengths. This relationship is commonly known as Bragg's equation:

$$2d \sin \theta = n\lambda, \quad (2.14)$$

where d is the lattice spacing, θ the Bragg angle, and λ is the wavelength of the radiation used.

In this work, no attempt is made to determine the crystal structure. In fact, the crystal structure is presumed to be known. Elastic strain yields a change Δd of the lattice spacing, which leads to a shift $\Delta\theta$ of the Bragg reflexes. As long as all strains are elastic, strain measurements by diffraction methods are possible. If the specimen is subjected to an external load, the lattice spacings will be different compared to the unloaded plane spacing. This difference is proportional to the micro strain acting on these planes. In Figure 2.3 the difference between macro strain and lattice strain is shown for a polycrystalline thin film.

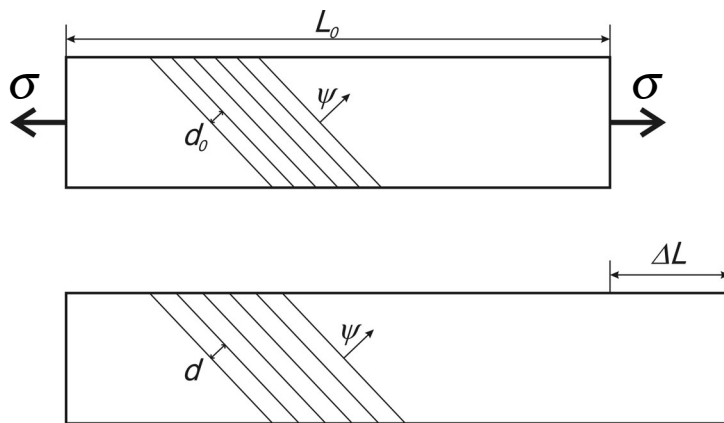


Figure 2.3: Illustration of macro strains and lattice strains for the case of a thin film. Macro strains are obtained by the total length difference $\epsilon_{macro} = \Delta L / L_0$; micro strains are obtained by the total lattice constant difference $\epsilon_{micro} = (d - d_0) / d_0$.

The lattice strain is obtained directly by differentiating Bragg's Equation (2.14):

³ See Laue (1962). The dynamic theory of X-ray diffraction must be applied for single crystalline materials [Ewald (1920)]. Single crystals including layers and multilayers are excluded from the discussion in this work.

$$\varepsilon = \frac{\Delta d}{d_0} = -\cot\theta \cdot \Delta\theta, \quad (2.15)$$

where d_0 is the unstressed lattice spacing. According to Equation , the accuracy of strain measurements is better at large Bragg angles. A general problem with all diffraction techniques is the determination of absolute stresses because the unstrained lattice parameter d_0 must also be measured with sufficient accuracy. This task is laborious and often impossible, which is the reason why often only the evolution of relative strains during mechanical tests is reported in literature. If the elastic constants are known, the residual and applied stresses can possibly be calculated using the theory of elasticity. In order to obtain the six independent components of the strain tensor, six independent measurements are required in general. Homogeneous strains will only shift the position of a Bragg reflex whereas the width, determined by the number of reflecting lattice planes and the grain size, stays constant. Inhomogeneous strains, however, yield a peak shift as well as peak broadening. The corresponding average stress is called *macro stress*; stress causing Bragg peak broadening is called *micro stress*.

In order to determine the strain tensor (see Equation (2.3a)) from the lattice strains measured along different angles it is useful to define adequate coordinate systems. The orthogonal coordinate systems used in this work are shown in Figure 2.4. The axes \mathbf{S}_i are numbered in the following way: \mathbf{S}_1 and \mathbf{S}_2 are oriented parallel to the specimen plane, axis \mathbf{S}_3 is oriented perpendicular to the specimen plane. The laboratory system \mathbf{L}_i is defined such that \mathbf{L}_3 lies in the direction of the normal of the planes (hkl) along which the lattice spacing is measured by X-rays. \mathbf{L}_1 and \mathbf{L}_2 lie in the specimen plane and define the plane of the azimuthal angle φ by with these axes are rotated against \mathbf{S}_1 or \mathbf{S}_2 , respectively. Following the convention by Dölle (1979) (see also Noyan and Cohen (1987)) primed tensor quantities refer to the laboratory system whereas unprimed tensor quantities refer to the sample coordinate system.

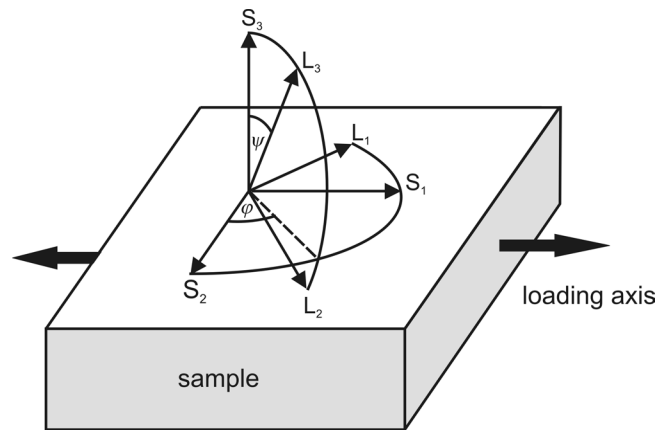


Figure 2.4: Definition of sample (S) and laboratory (L) coordinate systems as well as azimuthal angle φ and inclination angle ψ .

The lattice strain along \mathbf{L}_3 , measured for a given reflection hkl , is obtained from the lattice spacing $d_{\varphi\psi}$ according to Equation by the following simple relationship:

$$(\varepsilon'_{33})_{\varphi\psi} = \frac{d_{\varphi\psi} - d_0}{d_0}. \quad (2.16)$$

The strain measured in the laboratory coordinate system can be expressed by the lattice strains ε_{ij} in the sample coordinate system by tensor transformation as described in the textbook by Noyan and Cohen (1987). For this operation the sample coordinate system is rotated around the \mathbf{S}_3 axis by the azimuthal angle φ and tilted around \mathbf{S}_2 by the inclination angle ψ . The transformation matrix is

$$a_{S \rightarrow L} = \begin{pmatrix} \cos \varphi \cos \psi & \sin \varphi \cos \psi & -\sin \psi \\ -\sin \varphi & \cos \varphi & 0 \\ \cos \varphi \sin \psi & \sin \varphi \sin \psi & \cos \psi \end{pmatrix}. \quad (2.17)$$

Applying the transformation to Equation (2.16), the lattice strain in the laboratory coordinate system can be expressed by strains in the sample coordinate system by the following equation:

$$(\varepsilon'_{33})_{\varphi\psi} = \varepsilon_{11} \cos^2 \varphi \sin^2 \psi + \varepsilon_{12} \sin 2\varphi \sin^2 \psi + \varepsilon_{22} \sin^2 \varphi \sin^2 \psi + \varepsilon_{33} \cos^2 \psi + \varepsilon_{13} \cos \varphi \sin 2\psi + \varepsilon_{23} \sin \varphi \sin 2\psi. \quad (2.18)$$

Equation (2.18) was derived by Glocker (1936) and is called the fundamental Equation of X-ray strain determination.

2.2.4 Biaxial Residual Stress Analysis - The $\sin^2\psi$ Method

The so-called $\sin^2\psi$ method is the common technique to determine stresses by X-ray diffraction. It is applied in this work to determine residual stresses in metallic thin films. As described in detail i.e. by Noyan and Cohen (1987) or by Hauk (1998), the residual stress can be obtained by plotting the lattice spacings d_ψ against $\sin^2\psi$. The application of the $\sin^2\psi$ method to thin films has also been described extensively i.e. by Flinn and Chiang (1990), Besser et al. (1994), or Kuschke and Arzt (1994).

For a polycrystalline thin film on a substrate or the surface of a bulk material, the stress tensor is biaxial within the range of lattice planes irradiated by the X-ray beam. In this case, the orientations of the principal strain axes with respect to the specimen coordinate system are known. The strain $\varepsilon_{\phi\psi}$ existing in an arbitrary direction defined by the in-plane azimuthal angle ϕ and the out-of-plane inclination angle ψ (see Figure 2.4) depends on the principal strains ε_{11} , ε_{22} and ε_{33} as follows:

$$(\varepsilon'_{33})_{\phi\psi} = \varepsilon_{11} \sin^2 \phi \sin^2 \psi + \varepsilon_{22} \cos^2 \phi \sin^2 \psi + \varepsilon_{33} \cos^2 \psi . \quad (2.19)$$

Depositing a thin film on an amorphous substrate yields in-plane randomly oriented grains, which means that in the as-deposited state, i.e. prior to applying any tensile load, the stress state in the thin film can be considered as equibiaxial and thus ε_{11} must be equal to ε_{22} . Hence, the strain is independent of the azimuthal angle ϕ and Equation (2.19) reduces to

$$(\varepsilon'_{33})_{\psi} = \varepsilon_{11} \sin^2 \psi + \varepsilon_{33} \cos^2 \psi = (\varepsilon_{11} - \varepsilon_{33}) \sin^2 \psi + \varepsilon_{33} , \quad (2.20)$$

and for the lattice spacing d_ψ , which is the quantity measured in a diffraction experiment, we obtain

$$d_\psi = d_0 \left((\varepsilon'_{33})_{\psi} + 1 \right) = d_0 (\varepsilon_{11} - \varepsilon_{33}) \sin^2 \psi + d_0 (\varepsilon_{33} + 1) , \quad (2.21)$$

where d_0 is again the unstressed lattice spacing. Equation (2.21) has the form $d_\psi = m \sin^2 \psi + b$. The two parameters m and b are thus obtained by plotting the lattice spacings d_ψ measured at different inclination angles ψ against $\sin^2\psi$. The ratio m/b does not depend on the stress-free lattice spacing d_0 and is, at a very good approximation, equal to the strain difference $\varepsilon_{11} - \varepsilon_{33}$:

$$\frac{m}{b} = \frac{d_0(\varepsilon_{11} - \varepsilon_{33})}{d_0(\varepsilon_{33} + 1)} \approx \varepsilon_{11} - \varepsilon_{33}. \quad (2.22)$$

In case of a polycrystalline film exhibiting a perfect fiber texture, the stiffness matrix has the following form:

$$C'_{ij} = \begin{pmatrix} C'_{11} & C'_{12} & C'_{13} & 0 & C'_{15} & 0 \\ C'_{12} & C'_{11} & C'_{13} & 0 & C'_{25} & 0 \\ C'_{13} & C'_{13} & C'_{33} & 0 & 0 & 0 \\ 0 & 0 & 0 & C'_{44} & 0 & C'_{46} \\ C'_{15} & C'_{25} & 0 & 0 & C'_{44} & 0 \\ 0 & 0 & 0 & C'_{46} & 0 & C'_{66} \end{pmatrix}, \quad (2.23)$$

where C'_{ij} are the elastic constants of the thin film material in the sample coordinate system (S). For a cubic material exhibiting a perfect $\langle 111 \rangle$ fiber texture, the relationship between these elastic constants and the elastic constants in crystal coordinates (C_{11} , C_{12} , and C_{44}) are obtained by coordinate transformation:

$$C'_{11} = \frac{C_{11} + C_{12} + 2C_{44}}{2}, \quad (2.24a)$$

$$C'_{12} = \frac{C_{11} + 5C_{12} + 2C_{44}}{6}, \quad (2.24b)$$

$$C'_{13} = \frac{C_{11} + 2C_{12} - 2C_{44}}{3}, \quad (2.24c)$$

$$C'_{33} = \frac{C_{11} + 2C_{12} + 4C_{44}}{3}. \quad (2.24d)$$

The equibiaxial stress is a linear function of the strain difference ($\varepsilon_1 - \varepsilon_3$), which, according to Equation (2.21), can be determined by the $\sin^2\psi$ method. Combining equations (2.21)-(2.23) and applying Hooke's law yields:

$$\sigma_{11} = \sigma_{22} = \frac{(C'_{12} + C'_{13})C'_{33} + 2C'_{13}{}^2}{2C'_{13} + C'_{33}} (\varepsilon_{11} - \varepsilon_{33}) \approx \frac{(C'_{12} + C'_{13})C'_{33} + 2C'_{13}{}^2}{2C'_{13} + C'_{33}} \frac{m}{b}. \quad (2.25)$$

The residual stress in the film is thus obtained by plotting the lattice spacings d_ψ against $\sin^2\psi$. A linear fit to the dataset obtained in this way yields the ratio m/b from which the equibiaxial stress is derived according to Equation (2.25) using the elastic constants given in Appendix A. The $\sin^2\psi$ method is a straightforward method for measuring the equibiaxial

residual stress state existing in an as-deposited film. However, since the specimen must be tilted in order to vary the inclination angle ψ , the measurement procedure is time-consuming and thus not very well suited for *in situ* experiments during which a large number of stress measurements are desired. Upon straining the film-substrate composite sample in a uniaxial tensile test, the rotational symmetry of the stress state in the film with respect to axis S_3 is broken, and in order to measure the stress in the transverse direction with the same accuracy as in the longitudinal direction, $\sin^2\psi$ measurements must be performed at $\varphi = 90^\circ$. For this, the specimen would have to be rotated around a second axis, making the whole measurement procedure even more laborious and time-consuming. In order to perform *in situ* tensile tests with a higher strain rate, it is desirable to measure the complete stress tensor by one single X-ray exposure. This can be achieved with a new method which will be reported in chapter 3.2.

2.2.5 Measurement of Lattice Strains in the Bulk by High-Energy X-Rays

The measurement of macroscopic internal stresses (type-I stresses, see chapter 2.2.3) by diffraction methods is based on the measurement of the deviation of the lattice spacing for crystallographic planes from the stress-free material. In the simplest case, there is a linear relation between the deviation of lattice spacings and the macroscopic stress. However, due to elastic anisotropy, which is the result of intergranular stresses (type-II stresses), there is not one but several linear relations which depend on the lattice planes. Often, the measured macroscopic stresses lead to plastic deformation of the material. If plasticity occurs, the stress-strain relations are generally non-linear, which implies that in the presence of plastic anisotropy there are several non-linear relations between applied stress and lattice strains.

Classical techniques to measure volume-averaged lattice strains within the bulk of crystalline metallic or ceramic materials are based on the diffraction of thermal neutrons. While these techniques have been successful for many applications, typical measurement times are long (in the order of several hours) due to the low flux available at current neutron sources. The availability of high-energy, high-flux X-rays from third generation synchrotron research facilities offers alternative approaches to diffraction measurements of internal strains which do not have these restrictions and are therefore complementary tools to neutron diffraction (see Pyzalla et al. (2000)). Hence, high-energy X-ray diffraction is a viable technique to

measure volume-averaged lattice strains within the bulk of polycrystals at increased speed compared to neutron diffraction (Liss et al. (2003)). Different techniques for high-energy X-ray strain measurements have been developed: Laue diffraction has successfully been applied for measurements within single crystals or individual grains using focused microbeams (Biermann et al. (1997), Spolenak et al. (2002)). Debye-Scherrer diffraction techniques have been developed to obtain volume-averaged results on polycrystalline samples (Royer et al. (2001), Daymond and Withers (1996), Korsunsky et al. (1998), Wanner and Dunand (2000)). An interesting procedure, the so-called $\sin^2\phi$ method, was established by these authors and will be described in detail in chapter 3.1.1. In this technique, the sample under investigation is irradiated by monochromatic X-rays (photon energy range of about 65-100 keV) and complete Debye-Scherrer rings are recorded using a high-resolution area detector. The lattice strains are obtained by analyzing the minute distortions of these rings. Wanner and Dunand (2000) report the use of a calibration substance attached to the sample in order to compensate for unintentional specimen movements during deformation. In the following chapter, advanced techniques based on this $\sin^2\phi$ method will be presented.

3 Methodology

In this chapter, the methodological aspects of determining stresses and strains at the diffraction limit of X-ray using a new synchrotron-based approach will be described. First, the principles of the *high-energy* $\sin^2\varphi$ method will be introduced and the issue of measurement limitations will be addressed. Thereafter a further developed $\sin^2\varphi$ -method will be presented which also relies on high-energy synchrotron radiation. Based on this measurement strategy, an experimental approach for characterizing the stress evolution *in situ* during high-temperature tensile tests will be presented. Afterwards, a novel *low-energy* $\sin^2\varphi$ -method suitable for *in situ* tensile tests on ultrathin metallic films will be reported. Finally, the strain analysis procedure will be described in detail.

3.1 Stress Evolution in the Bulk – High-Energy $\sin^2\varphi$ Method

3.1.1 Conventional Setup

The typical experimental setup using a high-energy normal-incidence X-ray method to measure lattice strains during mechanical loading was first described by Daymond and Withers (1996). In this kind of setup, the polycrystalline sample under investigation is irradiated with a parallel beam of monochromatic X-rays, and complete Debye-Scherrer-rings are recorded using a high-resolution area detector (CCD camera, image plate detector or wire frame detector). A schematic of the experimental setup is shown in Figure 3.1a. In Figure 3.1b typical Debye-Scherrer cones are shown. This high-energy method can especially be applied for characterizing the two dimensional, volume-averaged strain states within the bulk of flat samples with planar and parallel surface such as sheet materials or flat tensile specimens. The photon energy must be higher than 60 keV in order to penetrate the depth of materials of technical interest (see also Table 1). The diffraction condition can be compared to that of a transmission electron microscope since the wavelength is much smaller than the lattice spacings of the low-index planes which are thus almost parallel to the incident beam when they are in diffracting condition. Lattice strains averaged over the bulk are obtained in the plane normal to the X-ray beam. This plane contains the longitudinal direction (loading axis) as well as a transverse direction (perpendicular to the loading axis).

Table 1: Half-value thicknesses (50 % intensity absorption) of selected elements at different photon energies (after Wcislak et al. (2002)).

Photon energy [keV]	10	50	100	200
Wavelength [Å]	1.24	0.25	0.12	0.06
Element	Half-value thickness			
Aluminum	0.2 mm	1.1 cm	2.4 cm	3.3 cm
Titanium	10 μm	1 mm	6 mm	1.2 cm
Iron	5 μm	0.4 mm	2 mm	6 mm
Copper	4 μm	0.3 mm	2 mm	4 mm
Tungsten	4 μm	60 μm	80 μm	0.5 mm
Lead	5 μm	90 μm	0.3 mm	1.0 mm

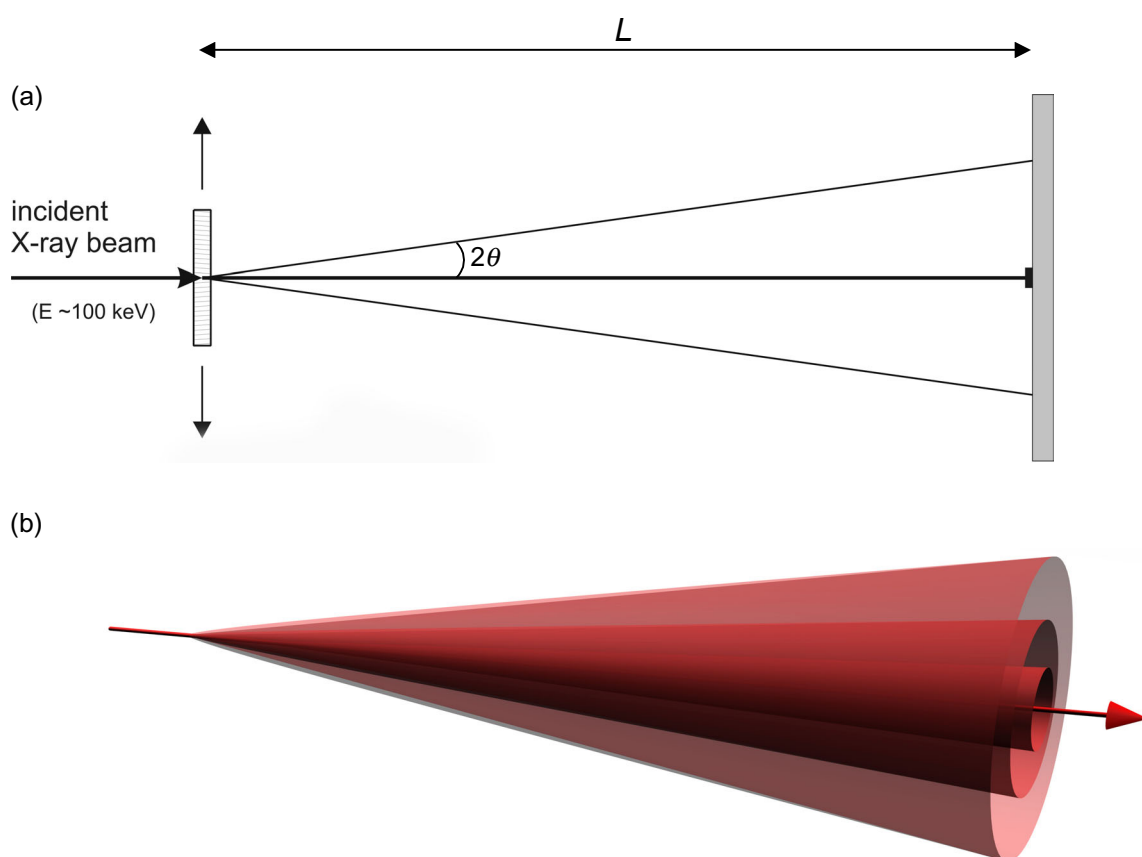


Figure 3.1: (a) Schematic of the experimental setup of the high-energy normal incidence transmission technique for $\sin^2\phi$ measurements. (b) Schematic Debye-Scherrer cones of a polycrystal irradiated in transmission by high-energy X-rays.

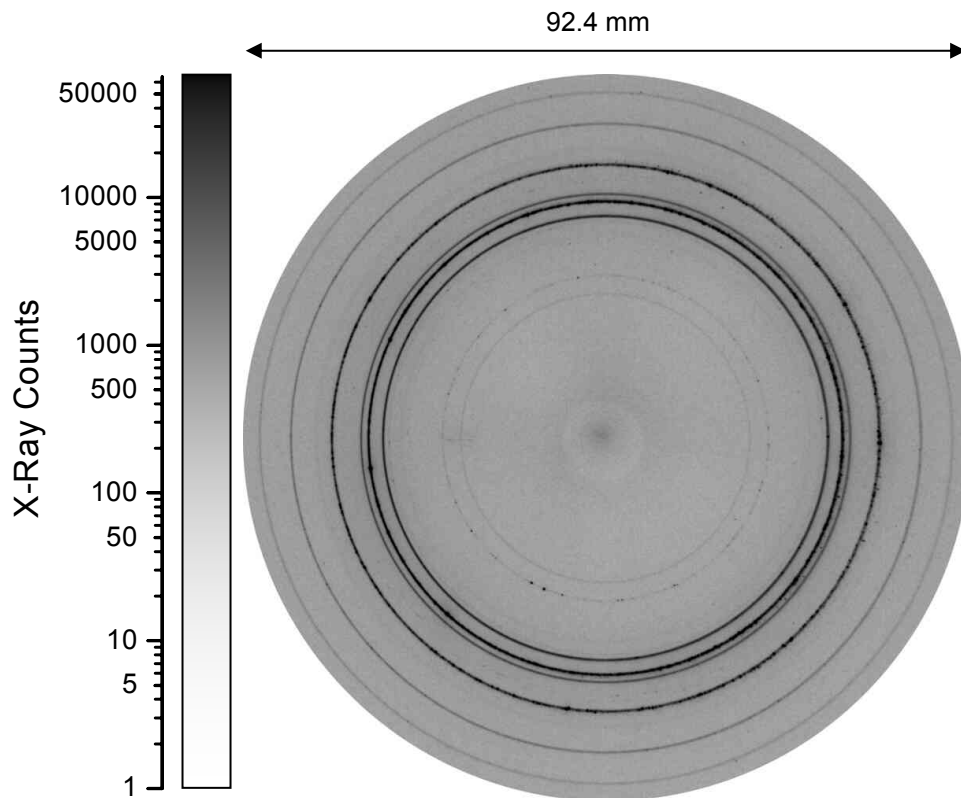


Figure 3.2: Part of a typical diffraction pattern of a Cu/Mo composite material as recorded by a MAR345 image plate area detector. Photon energy: 100 keV. This particular image shows a circular crop (diameter: 924 pixel, pixel size: 0.1 mm) of the original image which had as size of 3450×3450 pixel. In order to visualize all details of the as-recorded 16 bit grayscale image (exhibiting color values between 1 and 65536), the color space was inverted and scaled logarithmically, leading to color values between 0 and 4.82. Afterwards these color values were multiplied by an arbitrary factor of 50, leading to color values between 0 and 241 followed by a contrast enhancement using a linear tonal spreading between 80 and 180. By this operation, out of the logscale color values between 0 and 241 all values below 80 and above 180 are cropped, value 80 represents the grayscale color value 0 (white) and value 180 represents the grayscale color value 255 (black) in the final image.

Figure 3.2 shows typical diffraction rings which are recorded by the area detector. During the tensile test, the Debye-Scherrer rings on the detector screen are distorted elliptically. The semiaxes of this ellipse can be determined in the following way: First, the diameters of the diffraction rings D on the detector screen are obtained from the diffraction angle θ and the specimen-to-detector distance L by simple trigonometry:

$$D = 2L \tan(2\theta). \quad (3.1)$$

Combining Equation (3.1) with the Bragg's Equation (2.14), the following relationship for the change of lattice spacing Δd is obtained:

$$d = \frac{\lambda}{2 \sin \left(\frac{1}{2} \arctan \left(\frac{D}{2L} \right) \right)}. \quad (3.2)$$

At high energies the corresponding Bragg angles are small and therefore $D/2 \ll 1$. In this case the trigonometric functions can be replaced by their arguments leading to the following simplified equation:

$$d \approx \frac{2L\lambda}{D}. \quad (3.3)$$

The lattice strain *changes* can then be calculated according to Equation :

$$\Delta \varepsilon = \frac{\Delta d}{d_i} \approx \frac{D_i - D}{D} \approx \frac{D_i - D}{D_i}, \quad (3.4)$$

where index i denotes the initial, unloaded state.

It has been shown by Wanner and Dunand (2000) that a calibration substance has to be attached to the sample in order to compensate for unintentional sample movements and energy drifts of the monochromator. They found the following Equation robust against small changes of λ and L :

$$\Delta \varepsilon_{\varphi} \Big|_{\psi=\psi_0} \approx 1 - \frac{D_{s,\varphi}}{D_{s,\varphi}^i} \cdot \frac{D_{c,\varphi}^i}{D_{c,\varphi}}, \quad (3.5)$$

where $D_{s,\varphi}$ denotes the ring diameter of the sample at the azimuthal angle φ and $D_{c,\varphi}$ denotes the ring diameter of the calibration substance at the azimuthal angle φ .

In order to determine the almost equal semi-axes a and b of the elliptically distorted diffraction rings, the ring diameter can be approximated as $D(\varphi) = a + (b - a) \sin^2 \varphi$. By plotting $D(\varphi)$ against $\sin^2 \varphi$ and applying a linear fit to the dataset, the semi-axes are obtained at $\sin^2 \varphi = 1$ (corresponding to the longitudinal direction at $\varphi = 90^\circ$ and 270°) as well as at $\sin^2 \varphi = 0$ (corresponding to the transverse direction at $\varphi = 0^\circ$ and 180°). The longitudinal as well as the transverse lattice strains are then calculated using Equation (3.5) by taking the longitudinal and transverse semi-axes of sample and calibration substance into account.

The high-energy $\sin^2\varphi$ method can be summarized as follows: the changes of lattice strains are obtained by analyzing the changes of the diffraction ring semi-axes of the sample ($D_{s,\varphi}$) as well as of an attached calibration substance ($D_{c,\varphi}$) both referred to the unloaded state (i) and plotting against $\sin^2\varphi$.

3.1.2 Advanced Approach - Enlarged Setup

The major setback of the "conventional" $\sin^2\varphi$ method described above is its limitation to very fine-grained polycrystals and its sensitivity to unintentional specimen movements making the use of a calibration substance indispensable.

Limited gauge volume and grain statistics

The shape of the diffraction ring on the detector screen is determined by the number of grains which are in diffracting condition (see Figure 3.3). Hence, it is preferable to work with a large available gauge volume. This can be achieved by using thick samples. However, the maximum sample thickness is defined by the penetration depth of the X-ray beam which depends on the energy used. Typical half-value thicknesses for high-energy X-rays are in the range of several millimeters (see Table 1 on page 26). The width of the diffraction rings is primarily defined by the spot size of the incident beam on the sample. In order to avoid overlap of adjacent diffraction rings, the ring widths must be small enough. Small rings are also required for sufficient strain resolution; this means that the ratio of width to diameter must be small enough to measure the elliptical distortions with adequate accuracy. In short, the available energy, the shape of the Debye-Scherrer rings i.e., the "spottiness" and the width-to-diameter ratio define the achievable strain resolution. In practice, the beam spot size is in the range of 0.5 mm, the sample thickness is about 1 mm, the available energy about 100 keV, the typical detector size about 350 mm, and the sample-to-detector distance about 1 m. For those parameters, a strain resolution better than 10^{-4} can be achieved only with materials exhibiting grain sizes less than about 10 μm . The conventional high-energy $\sin^2\varphi$ -method is thus limited to very fine-grained sample materials.

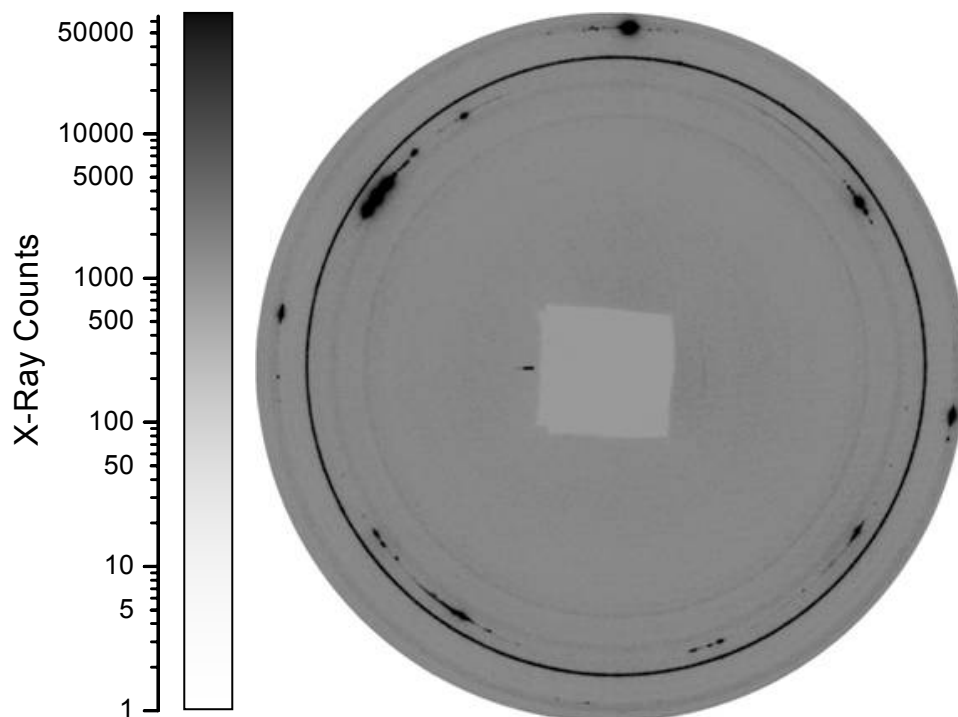


Figure 3.3: Effect of limited gauge volume. The continuous ring stems from the iron powder calibration substance, the spotty rings from the aluminum phase of a coarse-grained aluminum matrix fiber-reinforced composite material. Photon Energy: 65 keV. Detector: marccd area detector, diameter: 132 mm. This image was taken during a stay at the APS (Advanced Photon Source at the Argonne National Laboratory, IL., USA).

Sample movements

The high-energy $\sin^2\phi$ -method is especially sensitive to sample movements along the incident beam during mechanical or thermal loading. If they are unaccounted for, pseudo lattice strains are obtained which are inversely proportional to the specimen-to-detector distance. This means that for a specimen-to-detector distance of 1 m and sample movements in the order of about 100 μm the measuring error is in the range of 10^{-4} , thus leading to a very poor strain resolution. However, using a calibration substance is not practical for all purposes. At this point it has to be emphasized that the calibration substance must not be stressed with the sample. Serious problems arise for high-temperature experiments where it is difficult to attach the calibration substance to the sample and to keep it at the same temperature as the specimen. Omitting the calibration substance would therefore be desirable.

Enlarging the experimental setup

Theoretical considerations suggest that these setbacks can be diminished significantly by enlarging the whole experimental setup by one order of magnitude (Wanner and Dunand (2001)). Following this approach, a new $\sin^2\varphi$ method was developed in this work in order to overcome the two major restrictions: limited gauge volume (requiring fine-grained sample materials) and sensitivity to sample movements (requiring a calibration substance). shows a schematic of the enlarged setup as realized at HASYLAB. First results obtained by this new method have already been published in Böhm et al. (2003).

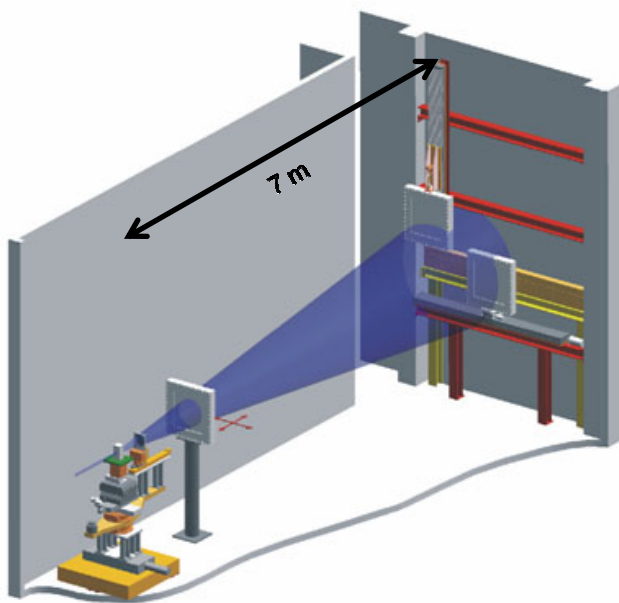


Figure 3.4: Schematic of the enlarged experimental setup as realized at the undulator beamline PETRA 2 of HASYLAB (image courtesy of GKSS).

In order to increase the strain resolution using a coarse-grained material, first good grain statistics must be achieved i.e., the gauge volume must be increased in order to obtain more grains in diffracting condition. One possible way would be to move the sample during the exposure. However, unintentional sample movements along the beam axis would be increased drastically thus leading to poor strain resolution. It is more straightforward to increase the spot size of the incident beam. Since the total possible sample thickness for an experiment is defined and limited by the energy of the incident X-ray beam, the gauge volume scales with the square of the beam width. The number of diffracting grains within this volume scales inversely with the cube of the grain size. Hence, a $10^{2/3}$ dependency (about a factor of five) is

obtained for the tolerable grain size if the ring diameter and width are increased by a factor of ten. The same strain resolution would be achieved for a material exhibiting a grain size of about $50\ \mu\text{m}$ as for a $10\ \mu\text{m}$ material using a non-enlarged setup.

Since the strain resolution is affected by the width-to-diameter ratio, the specimen-to-detector distance must be increased accordingly. Due to the very small beam divergence of the parallel incident beam produced by a synchrotron, the ring thickness is almost unaffected by the larger distance. One practical limitation is the available size of the experimental hutch and the size of the area detectors. By increasing the specimen-to-detector distance a calibration substance is no longer required any more because the measuring errors are inversely proportional to the specimen-to-detector distance L and pseudo strains are decreased accordingly. Thus, increasing L from 1 m to 10 m decreases the strain measurement errors by one order of magnitude from 10^{-4} to 10^{-5} .

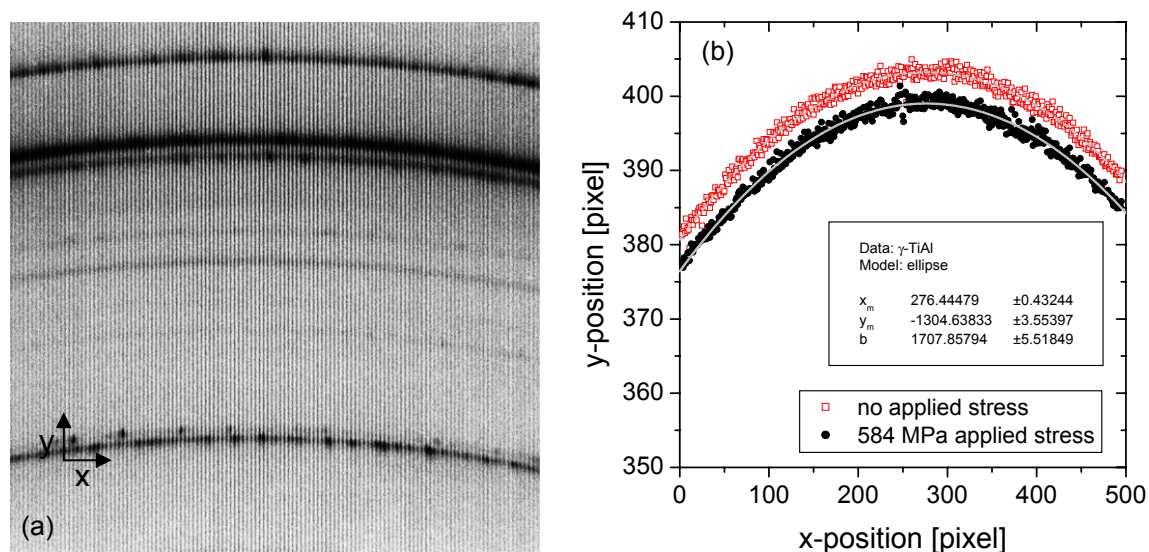


Figure 3.5: (a) Partial diffraction rings as recorded by the wire-frame detector at beamline PETRA 2 of HASYLAB monitoring strains in longitudinal direction. Photon energy: 90 keV. Specimen-to-detector distance: ~ 7 m. (b) Fitting of ellipse segments to partial Debye-Scherrer diffraction rings. The center of the ellipse with coordinates x_m and y_m lies outside the recorded image.

First experiments measuring lattice strains by high-energy synchrotron X-ray diffraction have been performed using an enlarged setup in which *two* area detectors are positioned at a large distance (7 meters) from the specimen. The elastic strains in the directions parallel to the loading axis (longitudinal direction) and perpendicular to the loading axis (transverse

direction) were deduced from the elliptical distortions of partial diffraction patterns as recorded by the two area detectors (see a). The following improved procedure has been developed in order to obtain the transverse and longitudinal lattice strains: the ring segment of interest is described by the maxima of Gaussian peaks fitted to the intensity data at 500 equispaced x -positions (see b for coordinates). The center of the undistorted diffraction ring lying far outside the image is calculated by fitting an ellipse segment to the data set obtained in this way. Relative to this centre, the diffraction ring diameter D_φ at each azimuthal angle φ is calculated for every data point of the ring segment (corresponding to the semiaxis b of the fitted ellipse in b). Since the two detectors cover narrow φ -ranges around 0° and 90° , two separate data sets are obtained. One set is used to determine the transverse main axis of the ellipse by extrapolating to $\sin^2\varphi = 0$, the other one to obtain the longitudinal main axis by extrapolating to $\sin^2\varphi = 1$. The changes of these main axes are used to calculate the lattice strain changes according to Equation (3.4).

3.2 Stress Evolution in Ultrathin Films – Low-Energy $\sin^2\varphi$ Method

In the present thesis, a novel experimental approach is taken by which it is possible for the first time to fully characterize the evolution of the biaxial stress state of thin films fast and efficiently by the $\sin^2\varphi$ method described in chapter 3.1 (Böhm et al. (2004)). The experimental method for thin film testing was developed during this work based on the knowledge obtained from the high-energy $\sin^2\varphi$ method for bulk samples. The intention was to make use of the advantages of the normal-incidence geometry for *in situ* tensile tests on thin films.

A well-established approach to characterize the flow behavior of a crystalline thin film is to perform a uniaxial *in situ* tensile test in an X-ray diffractometer. The film of interest is typically deposited on a dogbone-shaped substrate; film and substrate are strained simultaneously while the stress in the thin film is monitored by X-ray measurements. Early experiments were performed by Noyan and Sheikh (1992), Kretschmann et al. (1997), and by Renault et al. (1998) using metallic substrates like Ni or Al. In recent years, polyimide (Kapton[®] HN by DuPont) has been shown to serve as a better substrate material because this amorphous polymer is more compliant, can be deformed homogeneously up to very large

strains (>5%), and can be produced with excellent surface quality (Kraft et al. (2000), Hommel and Kraft (2001)). Also, polyimide can serve as a model material for flexible substrates which are important for various applications (such as flexible displays and wearable devices).

In order to apply the normal-incidence $\sin^2\varphi$ method in the presence of a pronounced <111> fiber texture, it has to be taken into account that intense and complete diffraction rings are obtained only if the wavelength of the incident X-ray beam is adjusted accordingly. For the case of a <111> fiber texture, the inclination ψ -angle for the $(\bar{1}11)$ lattice planes is $\psi = 70.5^\circ$ (see also Figure 4.12 on page 61). The required Bragg angle θ is then $\theta = 90^\circ - \psi = 19.47^\circ$, and $\sin\theta = 1/3$. In order to fulfill Bragg's Equation (2.14), the wavelength must then be $2/3$ of the lattice spacing d . For cubic metals d is in the order of 2 \AA thus leading to a required wavelength $\lambda = 4/3 \text{ \AA}$ corresponding to a photon energy of about 9.3 keV . This is the reason why *in situ* tensile tests on thin films can not be performed straightforward using high-energy synchrotron X-rays. For universal applications including textured thin film specimens, the method requires a *tunable*, brilliant X-ray source in the *low-energy* range ($E = 7 - 15 \text{ keV}$). To date, such X-ray sources are only available at dedicated synchrotron radiation facilities.

The correlation between the change in lattice strain $\Delta\varepsilon$ and the Bragg peak shift $\Delta\theta$ is obtained by the differentiated Bragg Equation (see Equation (2.15)):

$$\Delta\varepsilon = -\cot\theta \cdot \Delta\theta, \quad (3.6)$$

The Bragg-peak shift $\Delta\theta$ is therefore:

$$\Delta\theta = -\tan\theta \cdot \Delta\varepsilon. \quad (3.7)$$

In the normal-incidence geometry used for low-energy $\sin^2\varphi$ measurements, the diameter D of a Debye-Scherrer ring depends, according to Equation (3.1), only on the specimen-to-detector distance L and the Bragg-angle θ . For the change of the ring radius we obtain:

$$\Delta D = \frac{d(2L \tan(2\theta))}{d\theta} \cdot \Delta\theta = 4L[1 + \tan^2(2\theta)] \cdot \Delta\theta. \quad (3.8)$$

Combining Equations (3.1), (3.7) and (3.8) finally yields a relation between the relative change of ring diameter, $\Delta D/D$, and the change of elastic strain $\Delta\varepsilon$:

$$\frac{\Delta D}{D} = -2 \frac{1 + \tan^2(2\theta)}{\tan(2\theta)} \tan\theta \cdot \Delta\varepsilon. \quad (3.9)$$

Solving Equation (3.9) for $\Delta\varepsilon$ leads to

$$\Delta\varepsilon = -f(\theta) \frac{\Delta D}{D},$$

$$\text{with } f(\theta) = \frac{1}{2} \cot\theta \frac{\tan(2\theta)}{1 + \tan^2(2\theta)}. \quad (3.10)$$

The geometry function $f(\theta)$ is shown graphically in Figure 3.6.

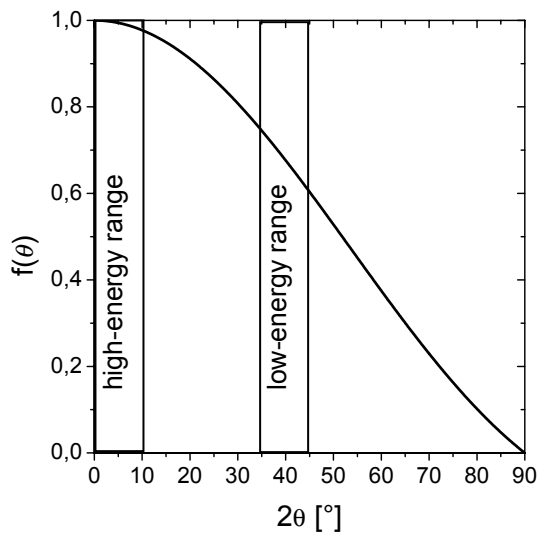


Figure 3.6: Geometry function for the calculation of lattice strains. At small Bragg angles θ , which correspond to high photon energies, $f(\theta)$ is nearly 1 and the θ dependent term can be omitted. Large angles, corresponding to low photon energies, lead to a non-linear behavior which must be corrected by the $f(\theta)$ geometry function.

As described in detail in chapter 3.1, it is essential to attach a calibration substance to the sample in order to compensate for unintentional sample movements. For low-energy experiments, Equation (3.5) must be modified to be applicable to large diffraction angles by including the additional geometry term $f(\theta)$:

$$\Delta\varepsilon_{\varphi} \Big|_{\psi=\psi_0} = f(\theta) \left(1 - \frac{D_{s,\varphi}}{D_{s,\varphi}^i} \cdot \frac{D_{c,\varphi}^i}{D_{c,\varphi}} \right). \quad (3.11)$$

The changes of the elastic lattice strains in the directions parallel to the loading axis $\Delta\varepsilon_{\varphi=90^\circ}$ (longitudinal direction) and perpendicular to the loading axis $\Delta\varepsilon_{\varphi=0^\circ}$ (transverse direction) can

thus be deduced from the elliptical distortions of the Debye-Scherrer rings. This can be done according to Equation (3.11) by plotting the ring diameter D_φ against $\sin^2\varphi$, where φ is the azimuthal angle.

The $\sin^2\psi$ method is applied only for characterizing the initial, equibiaxial *residual stress* state of the film. During the tensile test itself, no further absolute stress measurements are made. Instead, the stress *changes* relative to the initial stress state are recorded. For this, it was sufficient to measure only the variation of lattice spacing as a function of the azimuthal angle φ while keeping ψ at a constant value (ψ_0). A schematic of the experimental setup for the low-energy technique is shown in Figure 3.7a. The typical sample geometry and the directions of the main axes are shown in Figure 3.7b, and Figure 3.7c shows typical Debye-Scherrer rings for the case of low-energy X-rays. By orienting specimen axis 3, which is the direction of the surface normal of the sample, parallel to the incident X-ray beam and using an area detector for recording the diffraction patterns, it is possible to access the whole φ range (from 0° to 360°) without moving or rotating any component of the experimental setup, thus reducing the measurement time to a minimum.

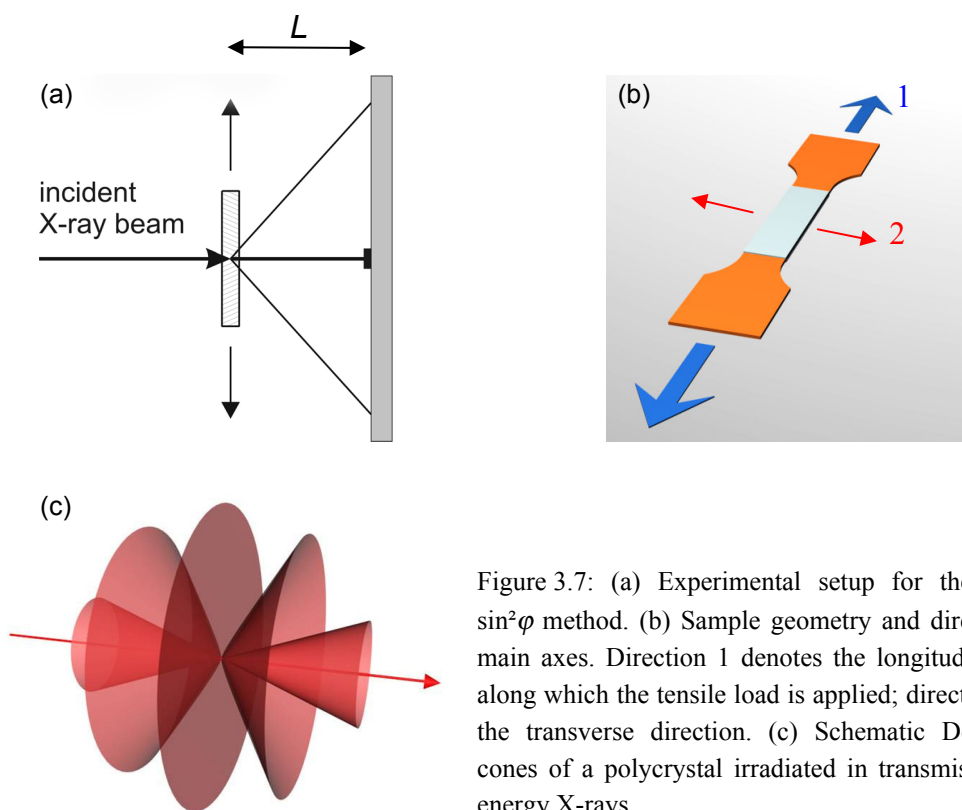


Figure 3.7: (a) Experimental setup for the low-energy $\sin^2\varphi$ method. (b) Sample geometry and directions of the main axes. Direction 1 denotes the longitudinal direction along which the tensile load is applied; direction 2 denotes the transverse direction. (c) Schematic Debye-Scherrer cones of a polycrystal irradiated in transmission by low-energy X-rays.

The measurement strategy is based on the following considerations: According to Equation (2.19), the change in lattice spacing observed at a fixed inclination angle ψ_0 when the stress state is change during the *in situ* experiment depends on the changes of the principal strains ($\Delta\varepsilon_1$, $\Delta\varepsilon_2$, and $\Delta\varepsilon_3$) and on the azimuthal angle φ in the following way:

$$\begin{aligned}\Delta d_\varphi \Big|_{\psi=\psi_0} &= d_i [\Delta\varepsilon_1 \sin^2 \varphi \sin^2 \psi_0 + \Delta\varepsilon_2 \cos^2 \varphi \sin^2 \psi_0 + \Delta\varepsilon_3 \cos^2 \psi_0] \\ &= [d_i (\Delta\varepsilon_1 - \Delta\varepsilon_2) \sin^2 \psi_0] \sin^2 \varphi + d_i [(\Delta\varepsilon_2 - \Delta\varepsilon_3) \sin^2 \psi_0 + \Delta\varepsilon_3].\end{aligned}\quad (3.12)$$

In this equation, d_i is the initial lattice spacing existing at inclination angle ψ_0 . Equation has the form

$$\Delta d_\varphi = M \sin^2 \varphi + B, \quad (3.13)$$

with substitutions

$$M = d_i (\Delta\varepsilon_1 - \Delta\varepsilon_2) \sin^2 \psi_0, \quad (3.14a)$$

$$B = d_i [(\Delta\varepsilon_2 - \Delta\varepsilon_3) \sin^2 \psi_0 + \Delta\varepsilon_3]. \quad (3.14b)$$

It will be shown at the end of this chapter how the values of M and B can be determined experimentally for every loading situation.

The strain changes are correlated to the stress changes via Hooke's law:

$$\Delta\varepsilon_1 = S'_{11} \Delta\sigma_1 + S'_{12} \Delta\sigma_2, \quad (3.15a)$$

$$\Delta\varepsilon_2 = S'_{12} \Delta\sigma_1 + S'_{11} \Delta\sigma_2, \quad (3.15b)$$

$$\Delta\varepsilon_3 = S'_{13} (\Delta\sigma_1 + \Delta\sigma_2). \quad (3.15c)$$

In this inverted version of Hooke's law, S'_{11} , S'_{12} , and S'_{13} are three independent compliance constants which are obtained by inverting the stiffness matrix given by Equation (2.23).

By combining equations (3.15a-c) with equations a) and b), we can express M and B as functions of $\Delta\sigma_1$ and $\Delta\sigma_2$

$$M = [d_i \sin^2 \psi_0 (S'_{11} - S'_{12})] \Delta\sigma_1 + [d_i \sin^2 \psi_0 (S'_{12} - S'_{11})] \Delta\sigma_2, \quad (3.16a)$$

$$B = [d_i (\sin^2 \psi_0 (S'_{12} - S'_{13}) + S'_{13})] \Delta\sigma_1 + [d_i (\sin^2 \psi_0 (S'_{11} - S'_{13}) + S'_{13})] \Delta\sigma_2. \quad (3.16b)$$

For the sake of brevity, we make use of the following substitutions:

$$\alpha = d_i \sin^2 \psi_0 (S'_{11} - S'_{12}), \quad (3.17a)$$

$$\beta = d_i \sin^2 \psi_0 (S'_{12} - S'_{11}), \quad (3.17b)$$

$$\gamma = d_i (\sin^2 \psi_0 (S'_{12} - S'_{13}) + S'_{13}), \quad (3.17c)$$

$$\delta = d_i (\sin^2 \psi_0 (S'_{11} - S'_{13}) + S'_{13}). \quad (3.17d)$$

By solving equations (3.16a) and (3.16b) for $\Delta\sigma_1$ and $\Delta\sigma_2$ we finally obtain the following equations:

$$\Delta\sigma_1 = \frac{\delta}{\delta\alpha - \beta\gamma} M - \frac{\beta}{\delta\alpha - \beta\gamma} B, \quad (3.18a)$$

$$\Delta\sigma_2 = -\frac{\gamma}{\delta\alpha - \beta\gamma} M + \frac{\alpha}{\delta\alpha - \beta\gamma} B. \quad (3.18b)$$

This new approach can be summarized as follows: First, the $\sin^2\psi$ method is applied to determine m and b and calculate the *residual stresses* using Equation (2.25). While deforming the sample in the *in situ* test, $\sin^2\phi$ measurements are applied repeatedly to monitor the *strain changes* by determining M and B and Equations (3.18a) and (3.18b) are used to calculate the *stress changes* in the thin film.

Combining Equations (3.11) and (3.11) leads to the following relationship for the relative changes of lattice spacings:

$$\Delta d_{\varphi=0^\circ} \Big|_{\psi=\psi_0} = \Delta \varepsilon_{\varphi=0^\circ} \Big|_{\psi=\psi_0} \cdot d_i \Big|_{\psi=\psi_0} = B, \quad (3.19a)$$

$$\Delta d_{\varphi=90^\circ} \Big|_{\psi=\psi_0} = \Delta \varepsilon_{\varphi=90^\circ} \Big|_{\psi=\psi_0} \cdot d_i \Big|_{\psi=\psi_0} = B + M. \quad (3.19b)$$

The relative stress changes $\Delta\sigma_1$ and $\Delta\sigma_2$ can finally be calculated by insertion of B and M into Equations (3.16a) and (3.16b). The required compliance constants for Cu and Au films are given in Appendix A.

3.3 Strain Evaluation Procedure

Using the normal-incidence $\sin^2\phi$ method, the diffraction patterns for both, the high-energy and the low-energy method, consist of Debye-Scherrer rings which are perfect, concentric circles under ideal conditions. During the tensile test, due to the applied strain, these circles

are distorted into an elliptical shape, the semiaxes of which are aligned parallel and perpendicular to the loading direction. Under ideal conditions (smooth diffraction rings due to a very small grain size and a texture-enhanced diffracted intensity) the simplest way for lattice strain evaluation would be to measure the ring diameters in the horizontal and vertical directions. However, coarse grained materials exhibit spotty diffraction rings leading to a very poor strain resolution. Therefore an algorithm taking the whole Debye-Scherrer rings into account was developed, which is based on the work published by Wanner and Dunand (2000) and has been extended by several enhancements to increase the strain resolution for spotty and weak diffraction rings. The implementation of the algorithm was performed using the IDL 6.0 programming language (Research Systems, Boulder, CO) a flowchart of which is presented in Figure 3.8.

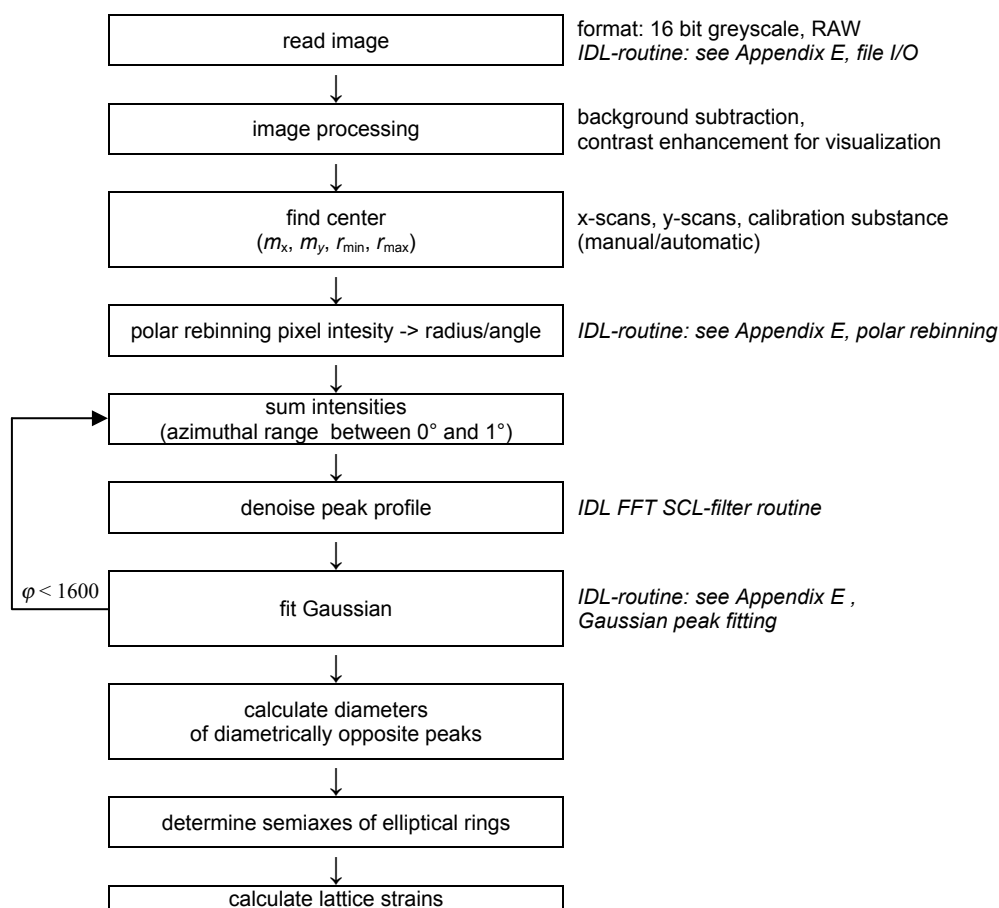


Figure 3.8: Flowchart of the strain evaluation algorithm implemented in the programming language IDL.

The algorithm is similar to that described by Korsunsky et al. (1998) and by Wanner and Dunand (2000). However, it differs in some important aspects. Averaging over an azimuthal $\Delta\varphi$ range is only performed if necessary for the Gaussian peak fits. This is required for very weak diffraction rings as obtained from ultrathin films. In this case azimuthal averaging was performed only over a very small $\Delta\varphi$ range between 0.5 and 1°. Weak peak profiles were additionally smoothed by an appropriate IDL filtering algorithm (Fast Fourier Transformation Filtering, FFT) in order to enhance the signal-to-noise ratio. It has to be mentioned that averaging, smoothing and filtering leads to a less well defined diffraction peak profile. However, it is the only way to obtain reasonable peak fits since weak and noisy peak profiles cannot be fitted at all. However, it is not important to obtain exact descriptions of single Gaussian peak profiles. Furthermore it is essential to obtain good statistics around the whole diffraction ring, which means that peak fitting must be possible at a large number of azimuthal positions. The fitting function itself (Gaussian, Voigt, etc.) is also of minor importance since only the positions of the peak maxima must be determined and an exact description of the whole peak profile is not required. The more peak maxima can be determined at different φ positions, the more points are obtained for the $\sin^2\varphi$ plot leading to a better defined slope and thus to a better strain resolution.

The improved strain evaluation algorithm has two major advantages: (1) Because averaging is only performed when necessary and only over a very small azimuthal φ range, every angular direction has to very good approximation the same statistical weight, independent of signal intensity. This way of averaging is crucial for strain evaluation of coarse-grained materials exhibiting spotty diffraction rings, because then the full information from the weak intensity range between high intensity spots is fully taken into account. (2) Since Gaussian peak fits are obtained at a large number of different φ positions, the average and the standard deviation of the peak widths can be used to characterize the evolution of microstructural and micromechanical deformation processes occurring in the material during deformation.

3.4 Measurement Errors

The strain measurement error for $\sin^2\varphi$ measurements can be obtained by error propagation calculation. According to Equation (3.11), the calculations yield:

$$\Delta(\Delta\varepsilon_\varphi) = f(\theta) \cdot \left(\frac{\partial(\Delta\varepsilon_\varphi)}{\partial D_{s,\varphi}} \Delta D_{s,\varphi} + \frac{\partial(\Delta\varepsilon_\varphi)}{\partial D_{s,\varphi}^i} \Delta D_{s,\varphi}^i + \frac{\partial(\Delta\varepsilon_\varphi)}{\partial D_{c,\varphi}} \Delta D_{c,\varphi} + \frac{\partial(\Delta\varepsilon_\varphi)}{\partial D_{c,\varphi}^i} \Delta D_{c,\varphi}^i \right) \quad (3.20)$$

$$\begin{aligned} \Delta(\Delta\varepsilon_\varphi) = f(\theta) \cdot & \left(-\frac{D_{c,\varphi}^i}{D_{s,\varphi}^i \cdot D_{c,\varphi}} \Delta D_{s,\varphi} + \frac{D_{s,\varphi} \cdot D_{c,\varphi}^i}{(D_{s,\varphi}^i)^2 \cdot D_{c,\varphi}} \Delta D_{s,\varphi}^i \right) + \\ & f(\theta) \cdot \left(\frac{D_{s,\varphi} \cdot D_{c,\varphi}^i}{D_{s,\varphi}^i (D_{c,\varphi})^2} \Delta D_{c,\varphi} + \frac{D_{s,\varphi}}{D_{s,\varphi}^i \cdot D_{c,\varphi}} \Delta D_{c,\varphi}^i \right) \end{aligned} \quad (3.21)$$

where $\Delta D_{s,\varphi}$ is the error of the ring diameter of the sample, $\Delta D_{c,\varphi}$ that of the calibration substance and superscript i denotes the initial, unstressed state. The $f(\theta)$ -function is assumed to be constant for small deviations of θ during the tensile test and therefore does not enter the error calculation. The measurement error of $\Delta\varepsilon$ is thus only determined by the measurement errors of all ring diameters entering Equation (3.11). These errors are obtained by the standard error of the linear fit applied to the data points in a $\sin^2\varphi$ plot. Because of the large number of data points – typically 1600 for all azimuthal φ positions – the standard error obtained from the linear fits is very small, usually in the subpixel resolution range of the detector. A typical value is a resolution of the ring diameters in the range of $\pm 1/5$ pixel (corresponding to a resolution of 16 μm if the best resolution of the marccd detector with a pixel size of 80 μm is used).

If the surface of the area detector is not normal to the beam axis, one obtains an elliptical distorted diffraction ring even if no external load was applied to the sample. This misalignment can be corrected by the calibration substance, since the unstrained powder ring is then also distorted elliptically. A rotation of the ellipse on the detector screen i.e. from an off-axis orientation of the tensile direction or a misalignment of the detector screen was also accounted for by introducing an additional fit parameter. While the measurement errors occurring due to relative translations of the sample along the axis of the incident beam are also corrected by the calibration substance, misalignment errors of the sample cannot be fully

eliminated by the calibration substance, i.e. rotation of the sample around its longitudinal axis during tensile testing can not be fully compensated, since the calibration procedure is based on the assumption of a constant spacing between specimen and calibration substance. This assumption is not true if the sample is rotated around an axis that does not coincide with the direction of the incident X-ray beam. However, such rotations could in practice not be found in any of the tensile tests performed, neither on bulk samples nor on thin films on a flexible polyimide substrate.

In summary, unintentional specimen movements must be eliminated either by using a calibration substance or, as has been shown in chapter 3.1.2, by using an enlarged experimental setup. Because experiments on fiber textured thin films have to be performed in the low-energy range leading to a very short specimen-to-detector distance in the range of only 10-15 cm, a calibration substance is indispensable in this case.

4 Experimental

In this chapter the experimental realization of the $\sin^2\phi$ -method will be described on several examples. First, there will be a brief introduction to the synchrotron X-ray sources and beamlines used in this work. Afterwards, the experimental realization as well as the materials investigated by the high-energy $\sin^2\phi$ method will be presented. Finally, the experimental implementation and the thin film systems investigated by low-energy $\sin^2\phi$ measurements will be described in detail.

4.1 Synchrotron X-Ray Sources

For this thesis, different synchrotron X-ray sources and beamlines were used. All high-energy X-ray diffraction experiments were performed at HASYLAB (Hamburger Synchrotronstrahlungslabor) of DESY (Deutsches Elektronen Synchrotron) using the high-energy beamlines BW5 and PETRA 2. All synchrotron X-ray diffraction measurements performed at low energies on thin films were carried out at the Surface Diffraction beamline of the Max-Planck-Institute for Metals Research (MPI-MF) located at the synchrotron radiation source ANKA (Karlsruhe, Germany).

Table 2: Key parameters of the MPI-MF Surface Diffraction Beamline at ANKA (2003)), the wiggler beamline BW5 at the DORIS storage ring as well as the PETRA undulator beamline at HASYLAB/DESY (2003).

	ANKA	DORIS wiggler	PETRA undulator
spot size at sample position [mm ²]	1×1	0.5×0.5	0.5×0.5
photon flux [photons/(s × 0.1 % energy bandwidth)]	10 ¹²	2×10 ⁻¹⁴	10 ⁻¹⁷
photon energy resolution [$\Delta E/E$]	2×10 ⁻⁴	1.1×10 ⁻³	7.5×10 ⁻⁵
X-ray wavelength range [Å]	0.62 – 2.0	0.12	0.16 – 0.06
photon energy range [keV]	6 – 20	100	80 – 200

4.1.1 DESY BW5 Beamline

The BW5 beamline is located at the DORIS storage ring of HASYLAB (see HASYLAB (2003)). DORIS is operated with positrons at an energy of 4.450 GeV. The initial beam current is 120 mA and the typical beam lifetime is about 8 hours. The polychromatic X-ray beam is generated at a bending magnet followed by a hard X-ray wiggler which has been designed to reach a critical energy of 26.5 keV. BW5 is dedicated for X-ray scattering

experiments at energies above 60 keV. The beamsize is defined by a tilt adjustable slit system before it enters the experimental endstation at a distance of 30 m from the source. The heat load from the optical elements is reduced by a water-cooled 1.5 mm thick copper plate which also serves as a high-pass energy filter. The wiggler and the filter together cut a spectral range between 60 and 200 keV from the full X-ray spectrum. The monochromator and analyzer crystals consist of selectable Si(111), Si(220) and Si(311) crystals which can be mounted in Laue geometry. The final beam size can be controlled by a motorized Ta cross slit system which can be varied between 0.5×0.5 and $6 \times 6 \text{ mm}^2$. The typical flux at the sample is about $5 \cdot 10^{10}$ photons/s/mm² at an energy of 100 keV. An intensity monitor as well as a motorized absorber wheel complete the whole setup (see Figure 4.1).

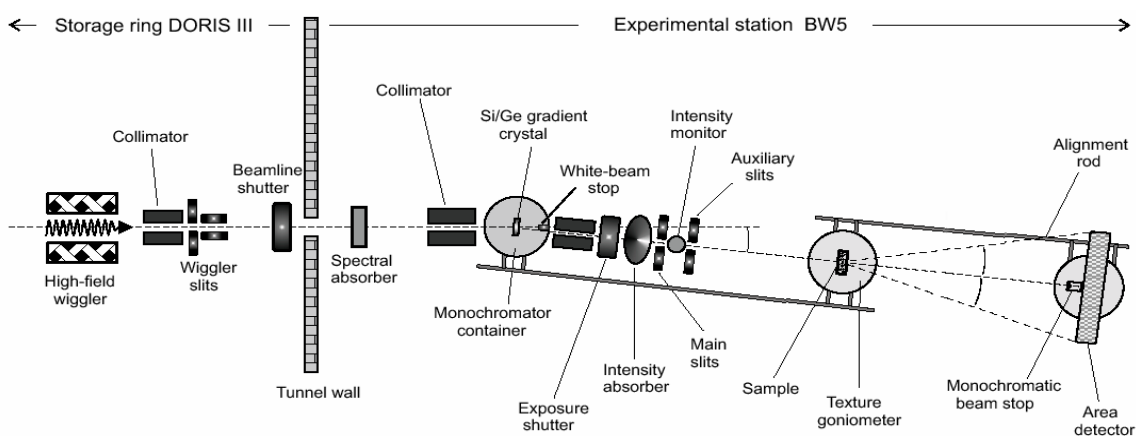


Figure 4.1: Schematic of the experimental station BW5 at HASYLAB/DESY. Graphics source: Wcislak et al. (2000) and Wcislak et al. (2002).

4.1.2 DESY PETRA 2 Beamline

The PETRA 2 beamline is another high-energy beamline at HASYLAB (HASYLAB (2003)) which is supplied with synchrotron radiation generated by an undulator insertion device installed at a 49.5 m long straight section of the PETRA II accelerator which covers a spectral range from 14 to 150 keV. A diamond crystal positioned approximately 106 m downstream from the undulator splits the primary beam into a low-energy branch (PETRA 1 beamline) and a high-energy branch (PETRA 2 beamline). The PETRA II storage ring serves as a part of the injector system of the HERA accelerator which is used for high-energy particle physics. Whenever the PETRA II accelerator is not needed for HERA, the PETRA 2 beamline is operated as a DESY test facility with only temporary access. Positrons or electrons are used

for undulator operation with a maximum current of 50 mA. Typical lifetimes of about 10 hours are achieved. PETRA 2 is equipped with a monochromator which consists of selectable Si crystals producing tunable X-rays up to an energy of about 150 keV.

The main advantage of the PETRA 2 beamline over BW5 is the much larger experimental endstation which enables much larger specimen-to-detector distances (up to 7 m), which is, as has been shown extensively in chapter 3.1.2, advantageous in many respects.

4.1.3 ANKA MPI-MF Beamline

The synchrotron radiation facility ANKA (ANKA (2003)) is located at the Forschungszentrum Karlsruhe and is typically operated at an electron energy of 2.5 GeV and with an initial electron beam current of 180 mA. Beam lifetimes longer than 20 hours are routinely achieved. At the Surface Diffraction beamline of the Max-Planck Institute for Metals Research (MPI-MF) the polychromatic photon beam is produced at a bending magnet and fed through the optical system of the beamline, which consists of a ruthenium-coated silicon mirror followed by a double-crystal monochromator. Tunable monochromatic X-ray beams are produced in the wavelength range between 0.6 and 2.1 Å corresponding to photon energies ranging from 20 to 6 keV. The mirror truncates the energy spectrum of the incident photons at its higher end in order to suppress the harmonic contents of the monochromatic beam and it also focuses the X-ray beam in the vertical direction. Two pairs of slit systems positioned on the downstream side of the monochromator delimit the X-ray beam in horizontal and vertical directions. The typical spot size used throughout the experiments was $1 \times 1 \text{ mm}^2$. The key parameters concerning the ANKA X-ray source are summarized in Table 2 on page 43.

4.2 High-Energy Experiments – Bulk Materials

4.2.1 Room Temperature Tensile Tests

A miniature, screw-driven tensile device (Kammrath & Weiss GmbH, Dortmund, Germany) was used to perform *in situ* X-ray uniaxial tensile and compression tests at room temperature either at the wiggler beamline BW5 or at the undulator beamline PETRA2 of HASYLAB. The macroscopic load vs. elongation curves were recorded by measuring the crosshead displacement using a linear variable differential transducer (LVDT) and the load using a 5 kN load cell. The sample under investigation was irradiated in transmission by a monochromatic, parallel high-energy X-ray beam and Debye-Scherrer rings were recorded with one or two

area detectors. For all tensile and compression tests the strain was increased or decreased in a stepwise manner and held constant during the X-ray exposure.

4.2.2 Furnace

All *in situ* X-ray high-temperature experiments were carried out using a heatable tensile testing device constructed and operated by Alain Jacques from the Laboratoire de Physique des Matériaux, Ecole des Mines, Nancy, France (see Feiereisen et al. (2003)). It mainly consists of a vacuum chamber in which a four columns mechanical testing device can be inserted. The tensile sample is inserted into two high-temperature resistant TZM grips (by Plansee AG, Reutte, Austria). TZM is a particle-strengthened molybdenum based alloy with fine dispersed Ti-carbides which are responsible for its high-temperature strength up to 1400°C (see Plansee (2003)). A photograph of the sample and the grips is shown in a, the mounted sample inside the furnace is shown in b.

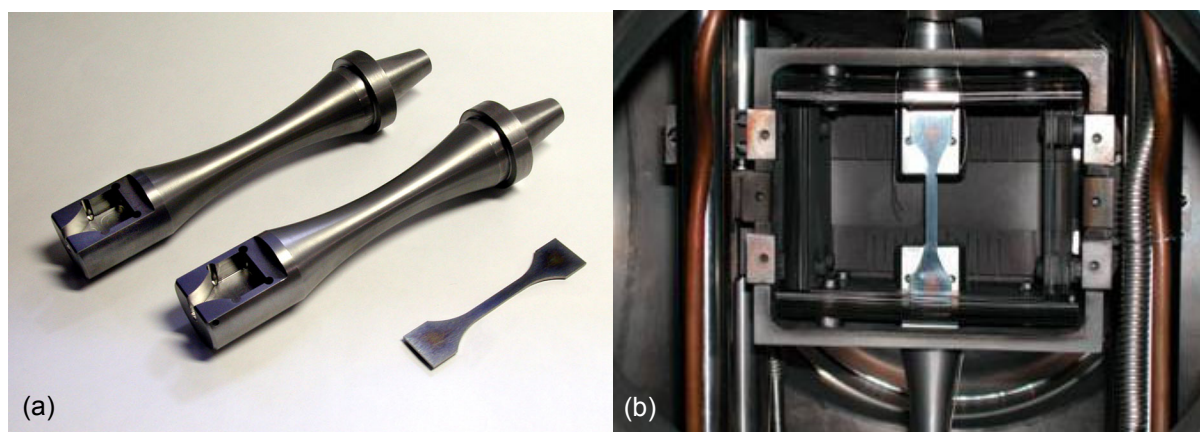


Figure 4.2: (a) Tensile specimen for high temperature experiments and high temperature resistant TZM grips. (b) Sample mounted within the furnace before a tensile test.

There are two aluminum windows with a diameter of 180 mm which are mounted on the portholes of the chamber. The tensile tester is equipped with a 5kN load cell located within the vacuum chamber for avoiding the influence of external pressure and a mobile crosshead outside the chamber to avoid vacuum contamination. The crosshead displacement is recorded by two LVDTs. The heater consists of two pairs of graphite resistors mounted in front of and behind the sample (see b). The temperature is measured directly on the sample by an attached thermocouple and the temperature is controlled by PID controllers using two thermocouples

in the vacuum near the sample. Thermal shielding for high temperature operation is additionally provided by several layers of tungsten reflectors on the top and bottom of the sample. The columns, grips and the load cell are water cooled. The vacuum chamber itself is cooled by air and additional cooling fans are necessary for the two aluminum windows. For temperature ranges up to 750 °C argon atmosphere can be used.

The consequences of additional material in the incident beam (e.g. the furnace used for *in situ* experiments) are shown in Figure 4.3.

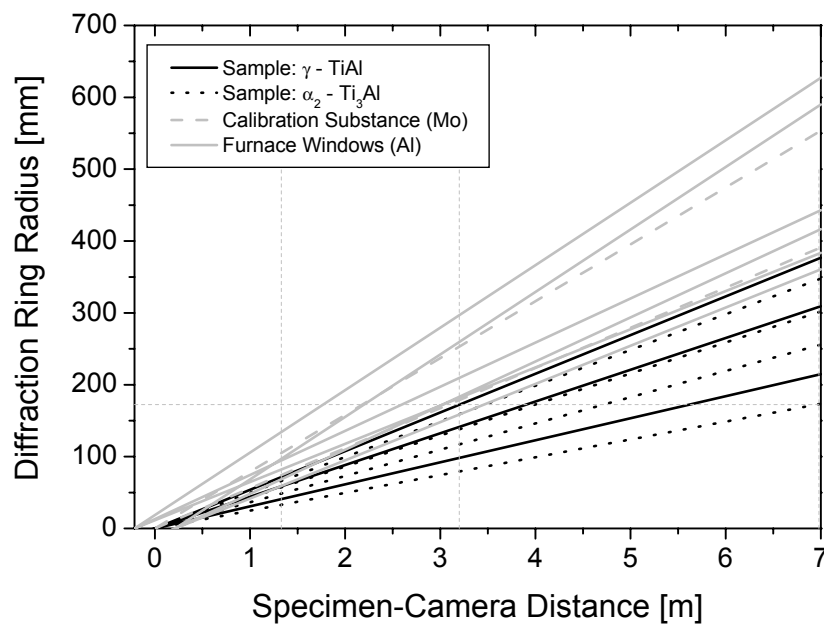


Figure 4.3: Interference of Debye-Scherrer diffraction rings from sample (black), calibration substance and furnace (light gray) at low specimen-to-detector distances (below 1 m). At a distance of 7 m, individual diffraction rings can be separated, and there is no overlap of diffraction rings from sample and furnace.

The sample is located in the origin of the specimen-camera distance axis. The furnace windows are situated 20 cm before and after the sample. The dark lines show the diffraction angles of cuts through the first Debye-Scherrer cones of the sample, the light lines those of the furnace and a Mo calibration substance attached to the sample. It can be seen clearly that all diffraction rings lie close side by side at short specimen-to-camera distances of about 1 m. This leads to overlapping and interfering diffraction rings which cannot be separated in order to apply the azimuthal scanning algorithm for $\sin^2\phi$ strain evaluation. Thus, it is very difficult to perform *in situ* experiments with such a furnace with a short camera length. Here, it is again very desirable to increase the specimen-to-detector distance. At a camera distance of

7 m, which is the distance which could be used in the enlarged setup at the PETRA 2 beamline, the spacing between individual diffraction rings is much larger and diffraction rings can be separated very easily. An enlarged experimental setup is therefore also desirable for high temperature *in situ* experiments using such a furnace.

4.2.3 Experimental Setups Used

High-energy $\sin^2\phi$ measurements were performed at the beamline BW5 of HASYLAB using the conventional setup. The sample-to-detector distance was about 1 m. The specimen was irradiated with a parallel beam of 100 keV X-rays and complete Debye-Scherrer rings were recorded using an image-plate area detector (Model mar345 by MAR, Inc., Evanston, IL, USA) positioned "on axis" on the downstream side of the specimen. This detector has a diameter of 345 mm and a pixel size of $0.1 \times 0.1 \text{ mm}^2$. The dimensions of the recorded 16 bit grayscale images were 3450×3450 pixels. The sample to detector distance was 1150 mm, which means that complete diffraction rings could be recorded for diffraction angles up to $\theta = 4.3^\circ$. The spot size of the beam was $0.5 \times 0.5 \text{ mm}^2$ and the exposure time for each image was between 60 and 150 s. A Fe- or Si-powder calibration substance in a small container was attached to the sample as a reference with a rubber belt. The lattice strains in longitudinal and transverse directions are obtained from the distortions of the Debye-Scherrer rings relative to the unloaded state based on Equation (3.5). The strain evaluation procedure will be described in chapter 3.3.

The high-energy beamline PETRA 2 of HASYLAB also offers X-rays in the desired range of 100 keV. The key advantages over the BW5 station are that (a) the size of the experimental endstation is much larger, thus offering the possibility to position the area detector at a much greater distance (up to 7 m) from the sample (Kampmann et al. (2001)), and (b) that the beam divergence is substantially smaller ($\leq 50 \text{ } \mu\text{rad}$ instead of $\approx 1 \text{ mrad}$). In order to record complete diffraction rings at such an increased distance, the detector size must be increased accordingly. Since no area detectors with diameters of several meters are available up to now, the measurements were restricted to selected parts of the whole diffraction pattern.

First experiments using an enlarged setup were carried out at room temperature. The area detectors were positioned approximately 7 m from the specimen each recording ring segments

for the longitudinal and transverse direction respectively. Partial diffraction patterns of 90 keV photons were recorded using two Xe-gas area detectors which were developed by Kampmann et al. (2001) and by Marmotti et al. (2002). The Xe-detectors were aligned with the direction of their central anode wire parallel to the radius of the diffraction ring to achieve a peak shift resolution of about 0.1 mm along the 2θ direction. They allow for excellent background subtraction due to their single photon detection mode. The pixel size was 0.3 mm (radial) by 0.5 mm (tangential), and the total sensitive area 300 mm by 300 mm. No calibration substance was used. The deformation axis of the miniature tensile device was mounted vertically onto the sample goniometer. The sample was rotated from -0.5° to 0.5° around the horizontal axis perpendicular to the incident X-ray beam. During this tilting operation, 20 single frames were stored separately. The acquiring time was 50 s for each frame adding up to a total time of 1000 s per loading step. The further ring-segment analysis was based on averaged images obtained by stacking all 20 frames in order to increase the grain statistics.

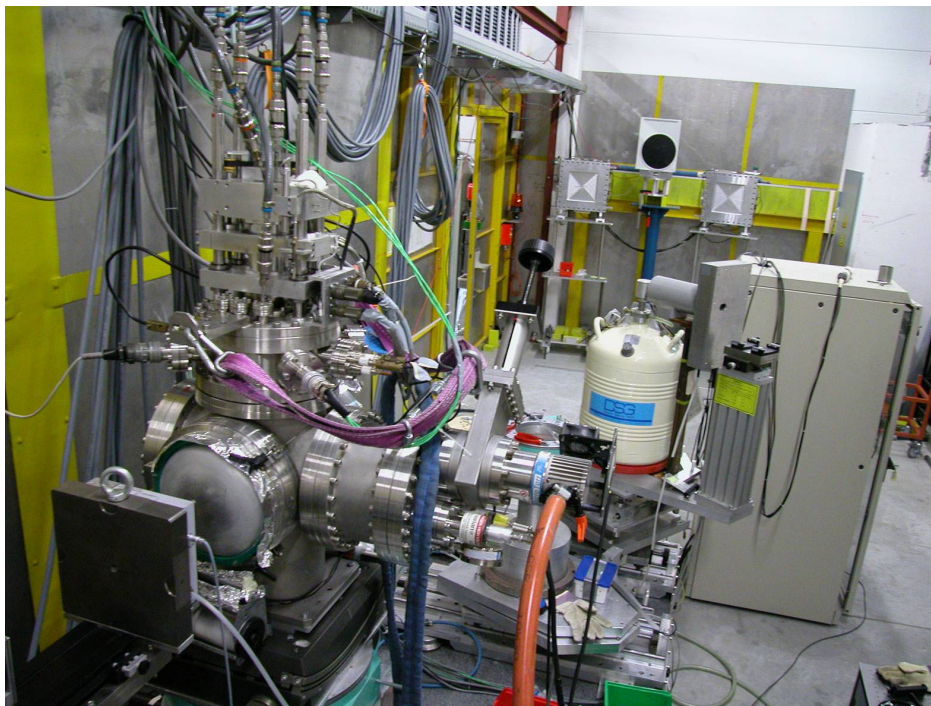


Figure 4.4: Photograph of the experimental setup for high temperature *in situ* tensile tests using a large specimen-to-detector distance as realized at the beamline PETRA 2 of HASYLAB. The detectors are positioned about 7 m from the sample.

High-temperature experiments have been performed during this work using the furnace described in chapter 4.2.1 which has been used intensively by A. Jacques and coworkers for *in situ* X-ray strain measurements using an energy dispersive method at the European Synchrotron Radiation Facility (ESRF) (Pyzalla et al. (2001)). First *in situ* tensile tests have been performed during this thesis using the enlarged setup (Böhm et al. (2003)). For high-temperature experiments only the longitudinal strains were recorded using the MAR345 image plate area detector due to the better pixel resolution. Another reason for using the image plate detector was the saturation of the wire frame detectors due to high intensity diffraction spots from the coarse-grained aluminum windows of the furnace. A photograph of the experimental setup as realized at beamline PETRA 2 of HASYLAB is shown in Figure 4.4.

4.2.4 Materials Investigated

In the following, several sample materials of technical as well as of scientific interest are described which were studied in the present thesis. The intention was to select the materials to demonstrate the potential of the high-energy method.

Cu/Mo Composite

The aim of the experiments on Cu/Mo composites was to compare the results of the method established at HASYLAB to those obtained by Wanner and Dunand (2000) at the APS (Advanced Photon Source, located at the Argonne National Laboratory, Argonne, IL. USA). Details of the production process of the composite can also be found in (Wanner and Dunand (2000)). The sample investigated in this work stems from the same fabrication process thus allowing a direct comparison to their studies. The material consists of a copper matrix reinforced with 15 % Mo particulates produced by solid-state powder metallurgy. Since Cu and Mo exhibit a very small mutual solubility, the Cu/Mo composite is composed by the two pure, untextured phases Cu and Mo.

Ti-based material

The intention of the studies on a Ti-based material was to get a reliable confirmation of the elastic anisotropy of a material exhibiting large strength combined with a relatively low Young's modulus thus leading to large elastic strains. Because a fine-grained material is

desirable for a good strain resolution, the technically important Ti-based material is an ideal sample material for developing methodological improvements. This was the main reason for the studies on this material. Since titanium exhibits a hexagonal structure, one obtains sufficient diffraction rings to distinguish different hkl orientations for studying elastic anisotropy. However, one challenge is now the development of capable strain evaluation routines. Because the total diffracted intensity for hexagonal materials is distributed over a larger number of diffraction rings relatively weak intensities are obtained compared to fcc and bcc polycrystals.

The specific strength of titanium can be further improved by incorporating reinforcements of low density, high Young's modulus and high strength (Lu et al. (2001)). Titanium matrix composites (TMCs) can be toughened by continuous- or discontinuous reinforcements. Discontinuously reinforced TMCs show isotropic behavior and can easily be fabricated at low cost. In the present work, a fine-grained material with discontinuous ceramic particles formed during casting was investigated. The samples were fabricated by the State Key Laboratory of Metal Matrix Composites, Jiao Tong University, Shanghai, China. They contained TiB whiskers as well as TiC particles fabricated by a common arc-melting technology. The reagents used were grade II sponge titanium (99%) and B₄C powder (98%, average particle size: 5-10 μm). A standard casting technique was used for fabricating the Ti/(TiB+TiC) material. The composition of the matrix was analyzed by the surface analytics department of the Max-Planck-Institute for Metals research using electron probe micro analysis (EPMA). The results can be found in Table 3. Although the material exhibits long TiB whiskers (see Figure 4.5a and b), it can, however, not be regarded as a fiber-reinforced composite due to low volume content of the reinforcements. In addition, the TiC particles are much too large for providing an oxide dispersion strengthening (ODS) effect as reported e.g. by Arzt and Grahle (1996) for disordered and ordered metallic materials. The advantage of the material with respect to methodological developments for the $\sin^2\phi$ technique is thus its fine grained titanium matrix exhibiting high strength within a wide range of strain.

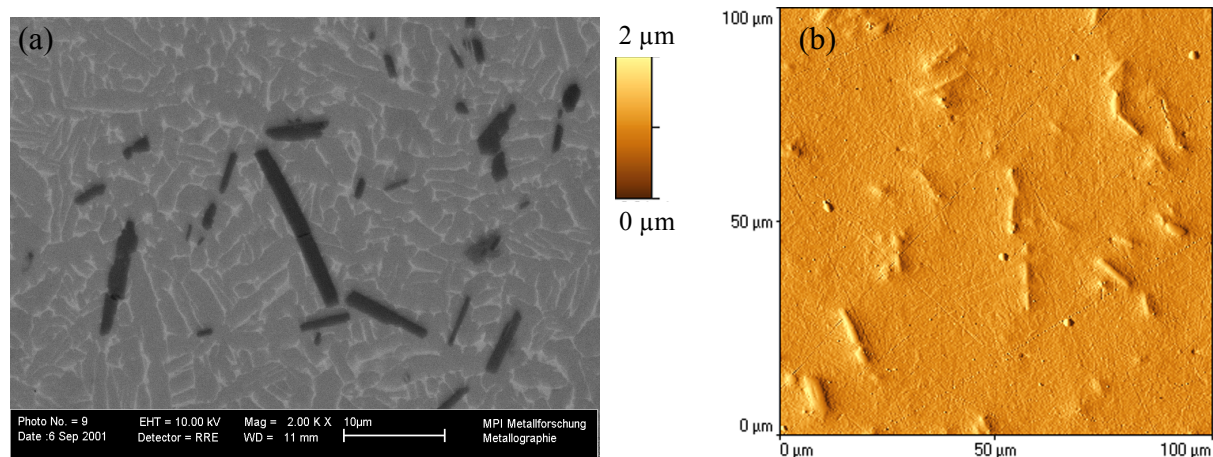


Figure 4.5: (a) Back-scattered electron micrograph of an *in situ* whisker reinforced Ti-based material. Dark phase: TiB + TiC, dark gray: Ti matrix, light gray: secondary grain boundary phase containing Zr, Sn and Si from contaminations during casting. (b) AFM image of the surface topography after grinding and polishing. The hard boride whiskers and carbide particles are clearly visible as hillocks because they are more resistant against abrasion during polishing.

Table 3: Composition of the matrix of the TiB + TiC whisker reinforced Ti-based material as measured by EPMA (electron probe micro analysis).

	Ti	Al	Zr	Sn	Si	C
matrix composition [wt.%]	86.7	5.5	3.4	2.7	0.4	0.7

γ -TiAl Alloys

The intermetallic phase γ -TiAl shows several physical and mechanical properties which are of interest for applications where high specific strength at high temperatures is demanded. Typical examples can be found in the aerospace industry: components in aircraft turbines, rocket propulsion systems or outer skin structures. The material also receives increasing interest for applications such as valves in automotive engineering. Components made of γ -TiAl alloys are about 15% lighter than components made of classical titanium alloys and have less than half of the weight compared to conventional super alloys. The disadvantage of TiAl alloys is their brittleness at room temperature due to a limited number of slip systems, which is a common problem for this type of ordered intermetallics. At room temperature, the ductility as well as the fracture toughness of TiAl is very low. From this point of view there is a large interest for fundamental research on this material. In this work, the micromechanical behavior of γ -TiAl was investigated at room temperature as well as at high temperatures between 700 and 800 °C. The focus was on studying the load partitioning between differently

oriented γ -TiAl grains during deformation. Knowing the stress-strain behavior of individual grain orientations can be valuable for optimizing the texture of polycrystalline samples with respect to "hard" and "soft" orientations during loading.

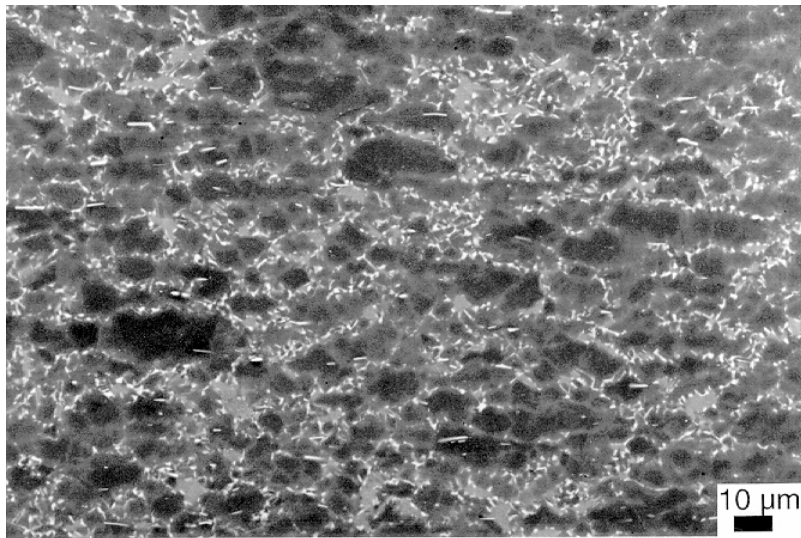


Figure 4.6: Microstructure of Ti-46.5at.%Al-4at.%(Cr, Nb, Ta, B) sheet material. The two major constituents are γ -TiAl (dark) and α_2 -Ti₃Al (light grey) as well as B2 phase (bcc CsCl structure, white rods); back-scattered scanning electron image.

Dog-bone shaped, flat tensile specimens with gauges 50 mm long, 5 mm wide and 1 mm thick were fabricated by electric discharge machining and subsequent mechanical polishing. The starting sheet material with a nominal composition of Ti-46.5at.%Al-4at.%(Cr, Nb, Ta, B), (γ -MET by Plansee AG, Reutte, Austria) was fabricated by a powder metallurgical process. The double extruded material had a fine grain size of about 5 μm . Details concerning the rolling process and the subsequent heat-treatment in order to flatten the sheet material are described in the work by Clemens et al. (1999). Bartels and Schillinger (2001) have performed texture measurements based on X-ray diffraction on this material. They report a sharp $\langle 111 \rangle$ -fiber texture following extrusion. According to Bartels et al. (1997) this texture causes a strong plastic anisotropy of the sheet material. The typical "near gamma" microstructure consisted predominantly of equiaxed γ -TiAl (tetragonal, L1₀ structure) grains with an average grain diameter of 15-20 μm (see Figure 4.6). Approximately 5 vol.% of α_2 -Ti₃Al phase (hexagonal, DO₁₉ structure) as well as B2 phase (bcc CsCl structure) were present at grain boundaries and triple points. The rod-like shaped particles consisted of Ta-borides which were preferentially

aligned in the rolling direction. A more detailed description of the phases is given by Inkson and Clemens (1999). Another material was HIPed from a prealloyed powder leading to a very homogeneous equiaxed microstructure. According to the X-ray measurements of Bartels and Schillinger (2001), the texture for this material is nearly random.

NiAl polycrystals

The intermetallic phase NiAl exhibits a combination of features relevant for high-temperature, light-weight structural applications. Of special interest are its high melting point, its superb oxidation resistance, and its relatively low density (Miracle (1993)). However, NiAl polycrystals exhibit little ductility at room temperature, which is attributed to an insufficient number of independent slip systems. Upon plastic deformation, microcracks form primarily at the grain boundaries due to plastic incompatibility of neighboring grains. In the case of compressive deformation, these microcracks are usually stable. Thus, NiAl polycrystals can be deformed up to several per cent of strain without global failure, while extensive microcracking and work-hardening was observed by Wanner et al. (1995).

The aim of the studies on NiAl was to investigate the evolution of lattice strains during plastic deformation for grains exhibiting different crystallographic orientations with respect to the loading axis. Lysak et al. (2001) suggest a stress-induced martensitic phase transformation as well as crack edge friction and avalanche-like dislocation activity as an origin for acoustic emission during unloading. Observing the possible occurrence of such a martensitic phase transformation during uniaxial compression tests was the second aim of the studies. The near-stoichiometric (50.3 at.% Ni) specimen material, produced by powder metallurgy, was free of texture and completely isotropic. Details on the processing procedure are reported by Wanner et al. (1995).

Uniaxial compressive deformation tests were carried out *in situ* up to stress levels of 840 MPa on NiAl polycrystals using the conventional experimental setup described in chapter 3.1 but without a calibration substance. The specimen was irradiated with a $1 \times 1 \text{ mm}^2$ wide beam of monochromatic 100 keV X-rays. At each loading step, the low-index Debye-Scherrer rings were recorded using a MAR345 image plate detector positioned on-axis on the downstream side of the specimen. The experiments were carried out on rectangular specimens with

dimensions $5.0 \times 2.2 \times 2.2 \text{ mm}^3$. The load was applied parallel to the long axis of the sample via hard metal punches and the stress was increased in steps of approximately 100 MPa. The applied load was measured using a load cell. Since the specimen strain could not be measured with appropriate precision from the crosshead displacement of the testing device, it was estimated from the applied stress based on the compressive stress-strain curve reported by Wanner et al. (1995) for the same material.

4.3 Low-Energy Experiments – Thin Films

The work on thin films has been performed in cooperation with Dr. R. Spolenak from the Max-Planck-Institute for Metals Research Stuttgart and P. Gruber from the Institute of Physical Metallurgy of the University of Stuttgart. This thesis focuses on the methodological development of the $\sin^2\phi$ method for thin film experiments.

4.3.1 Sample Fabrication and Characterization

All thin film samples were fabricated by the thin film laboratory (scientific central facility of the Max-Planck-Institute for Metals Research, Stuttgart). Dogbone-shaped specimens for tensile testing were cut out of 125 μm thick polyimide foil (Kapton[®] HN by DuPont). The specimen gauge section was 20 mm long and 6 mm wide (see Figure 4.7 for sample geometry).

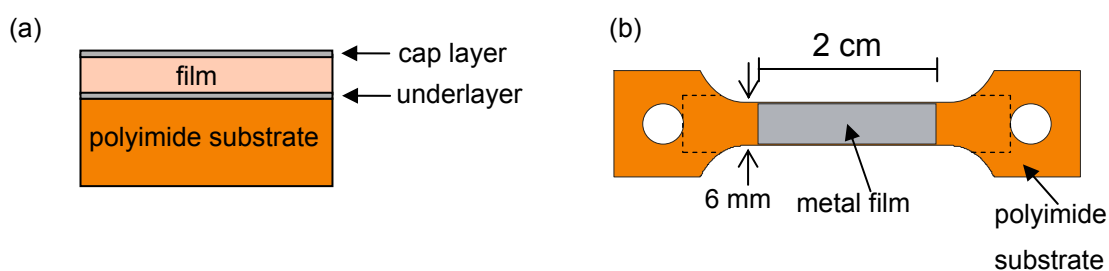


Figure 4.7: (a) Schematic cross-section of the thin film sample system. (b) Schematic top view of a sample for the *in situ* X-ray tensile tests. The dogbone shaped substrate exhibiting two holes was cut out of a sheet of polyimide foil and the metal film was sputtered on one side of the wafer. This is the standard shape for samples used for *in situ* X-ray tensile tests at the rotating anode. For synchrotron experiments a different tensile tester than for the laboratory source is used which has been described in chapter 4.2.1. The sample was cut along the dashed lines for the synchrotron measurements.

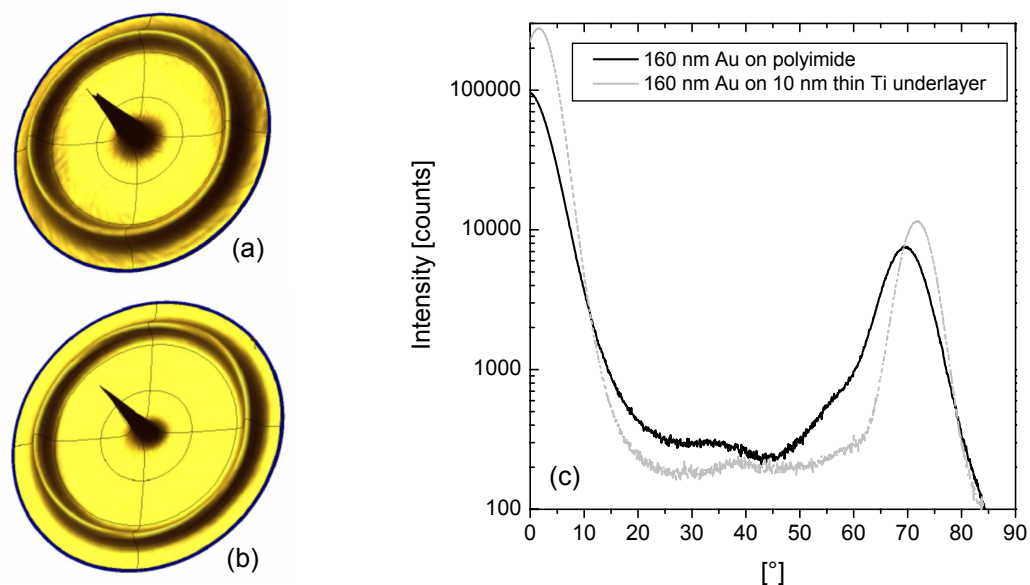


Figure 4.8: 111-pole Figure plots of a 160 nm thin Au layer showing a pronounced $\langle 111 \rangle$ fiber texture. (a) the Au film was sputtered directly on the polyimide substrate. Texture width (FWHM): 5.3° . (b) the Au film was sputtered on top of a 10 nm thin titanium underlayer. Texture width (FWHM): 7.3° (c) Radial sections through the pole Figure plots shown in (a) and (b) in the range between 0° and 90° .

Polycrystalline copper and gold films were deposited under ultrahigh vacuum (UHV) conditions (base pressure: 10^{-7} Pa) on one side of the samples by DC magnetron sputtering. Prior to film deposition the substrate surface was cleaned by argon ion bombardment (1 min at 200 eV). In order to enhance the adhesion and the texture of the films a 10 nm thick underlayer was deposited for some of the films (titanium underlayer in the case of the gold films and a tantalum underlayer for the copper films). The different thin film systems investigated are summarized in Table 4. During deposition the substrate was electrically grounded. The sputter rate was calibrated to allow for controlling the film thickness during sputtering. Film texture was determined from X-ray diffraction pole figures (see Figure 4.8).

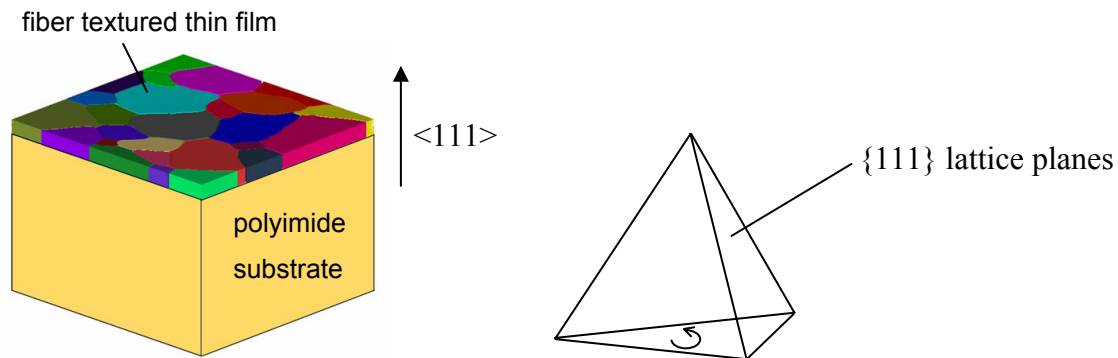


Figure 4.9: Illustration of the typical $\langle 111 \rangle$ fiber texture for thin films on polyimide substrates. The different colored grains of the film on the left represent $\langle 111 \rangle$ oriented grains with different in-plane rotation angles as illustrated by the $\{111\}$ plane pyramid on the right.

All films show a pronounced $\langle 111 \rangle$ fiber texture (see Figure 4.9 for illustration), which is very typical for thin films of fcc metals produced in this way (Thomson and Carel (1995)). Focused ion beam (FIB) investigations revealed that the films thicker than 100 nm were polycrystalline and consisted of equiaxed, columnar grains (see b). This microstructure is also expected for the thinner films (although it could not be seen by cross-sectional imaging because of the 20 nm resolution limit of the FIB). The films were completely closed and continuous as verified by SEM and FIB imaging (see a and b).

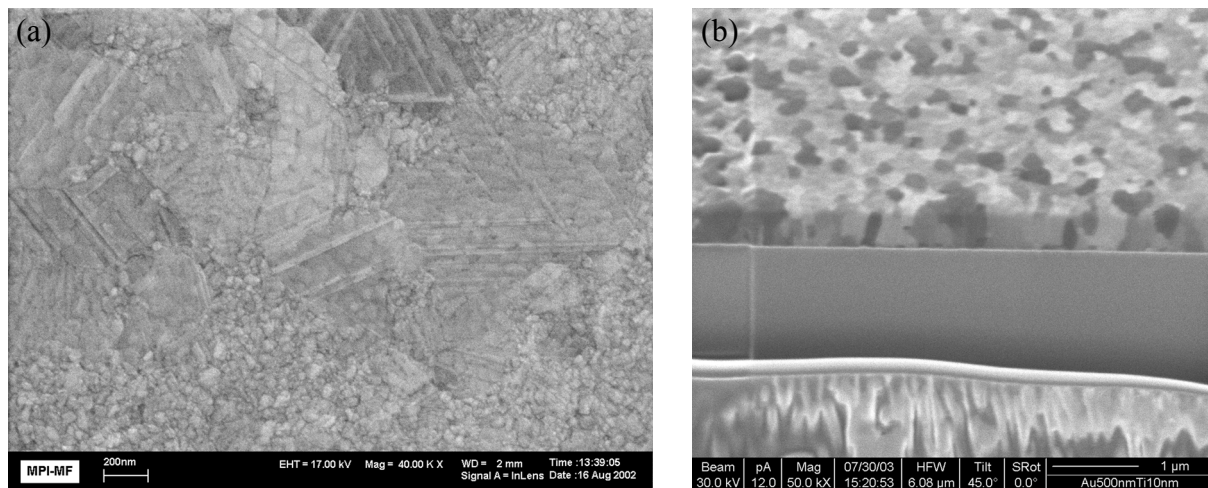


Figure 4.10: (a) Scanning electron micrograph of the closed surface of a 160 nm thin copper film on polyimide substrate (backscattered electron image, in-lens detector). Slight channeling contrast due to electron channeling could be obtained. The grain size is approximately in the range of the film thickness although large grains are visible which exhibit twins. (b) Focused ion beam image of a 500 nm thin gold film with a 10 nm thin titanium underlayer on a 125 μm thick polyimide substrate. The film was not annealed after deposition. A typical columnar grain structure can be observed.

Table 4: Investigated thin film systems reported in this thesis.

polyimide substrate thickness	underlayer	film thickness	cap layer
125 μm	10 nm Ti	20 nm Au	-
125 μm	10 nm Ti	40 nm Au	-
125 μm	10 nm Ti	80 nm Au	-
125 μm	10 nm Ti	160 nm Au	-
125 μm	10 nm Ti	240 nm Au	-
125 μm	10 nm Ti	500 nm Au	-
125 μm	10 nm Ti	1000 nm Au	-
125 μm	10 nm Ta	20 nm Cu	10 nm Ta
125 μm	10 nm Ta	50 nm Cu	10 nm Ta
125 μm	10 nm Ta	300 nm Cu	10 nm Ta
125 μm	10 nm Ta	160 nm Cu	-
125 μm	10 nm Ta	640 nm Cu	10 nm Ta
125 μm	-	80 nm Cu	-

4.3.2 Experimental Setup Used

The same microtensile tester as described in chapter 4.2.1 used for the high-energy experiments was equipped with a 250 N load cell. It was mounted on the sample stage of a 2+3 circle diffractometer aligned carefully with respect to the incident low-energy X-ray beam by an adjustable table. All low-energy experiments were performed at the synchrotron radiation facility ANKA (see chapter 4.1.3). The total sample strain was measured contact-free by a laser extensometer (Fiedler Optoelektronik GmbH, Germany). The accuracy of the laser-optical strain measurements is about 10^{-5} under ideal conditions (no air turbulences, constant temperature and perfect adjustment of the laser). Diffraction patterns were recorded using an area detector mounted on the detector arm of the diffractometer. This high-resolution area detector was a charge-coupled device (CCD camera, Model MAR CCD by MAR, Inc., Evanston, IL, USA). The X-ray sensitive screen has a diameter of 165 mm. Grayscale 16 bit images 2048×2048 pixels in size are produced by this detector. The exposure time was between 15 and 60s, the time required for readout and storage was 3s per image. Two different detector positions were used for characterizing the biaxial residual stresses produced

in the thin film during fabrication ($\sin^2\psi$ method) and for monitoring the stress evolution in the film during deformation ($\sin^2\phi$ method). Figure 4.11 shows photographs of the experimental setup for the different detector positions.

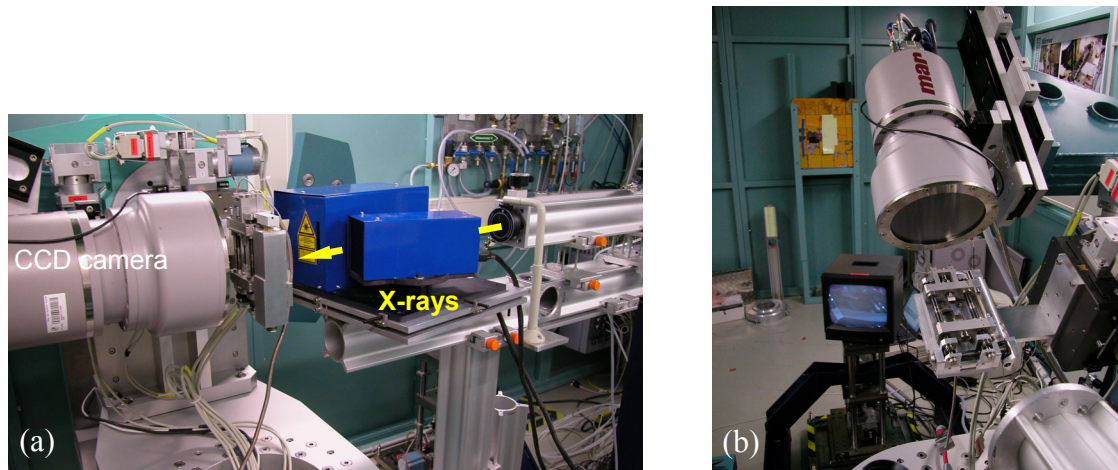


Figure 4.11: (a) Experimental setup for *in situ* X-ray tensile tests using the $\sin^2\phi$ method. (b) Experimental setup for characterizing the initial residual stress state using the $\sin^2\psi$ method.

4.3.3 Residual Stress Measurements - $\sin^2\psi$ Method

The initial residual stress state of the films was characterized by the $\sin^2\psi$ method measuring the interplanar spacing of 111 lattice planes exhibiting different inclination angles with respect to the film plane (see Figure 2.4). Due to the presence of a pronounced $\langle 111 \rangle$ -fiber-texture in the fcc films, high 111-peak intensities can be found only at inclination angles near $\psi_1 = 0^\circ$ and $\psi_2 = 70.53^\circ$. In order to ensure a high level of accuracy it is essential to detect the 111 ring of the sample as well as at least two rings of the calibration substance within a single CCD frame. The tuneability of the X-ray source is very helpful in this context because only by adjusting the wavelength can all experimental constraints (e.g., shadowing effects of the tensile tester) be accounted for. As an example, in the case of the gold films optimum results were obtained for $\lambda = 1.7735 \text{ \AA}$, resulting in Bragg angles of $2\theta_s = 44.34^\circ$ for the Au 111 reflection and of $2\theta = 46.76^\circ$ and 68.28° for the W 110 and W 200 reflections, respectively. The X-ray area detector was positioned 220 mm away from the specimen center, inclined by an angle of $\delta = 50^\circ$ from the primary X-ray beam. All parameters are summarized in Table 5, a photograph of the experimental setup for characterizing the residual stresses using the $\sin^2\psi$ method is shown in Figure 4.11b.

As described in chapter 2.2.4, the residual stress in the film is obtained by plotting the lattice spacings d_ψ against $\sin^2\psi$. A linear fit to the dataset obtained in this way yields the ratio m/b from which the equibiaxial stress is derived according to Equation (2.25) using the elastic constants given in Appendix A. For these measurements it is crucial that the thin film under investigation is either perfectly positioned in the center of rotation of the diffractometer or that all effects of misalignment are compensated by using a calibration substance. In the present case, the second option is recommended since a calibration substance is also essential for the $\sin^2\phi$ measurements. The calibration procedure is described in detail in Appendix D.

4.3.4 Stress Evolution - $\sin^2\phi$ Method

During the tensile tests, the detector was positioned "on-axis" on the downstream side of the specimen and the normal of the specimen surface was aligned parallel to the incident beam. In this so-called normal-incidence geometry, the Bragg angle θ at which strain measurements can be performed is determined by the texture of the sample, and the lattice spacing is given by the material under investigation. Figure 4.11a shows a photograph of the experimental setup. The microtensile tester is located in the center of the diffractometer on the vertical sample stage. Throughout the tensile test, the displacement of the crossheads was increased in steps of 20 to 100 μm . During each X-ray exposure, the crosshead position was kept constant. The total macroscopic strain was measured by the laser extensometer. The sample was typically strained up to a maximum total strain of 6.5 % and subsequently unloaded.

All normal-incidence measurements carried out on thin films during this thesis are based on the 111 diffraction ring. Due to the pronounced $\langle 111 \rangle$ fiber texture, strong diffracted intensities are found at ψ angles of 0° and 70.53° . Full Debye-Scherrer rings can be obtained for $\psi_0 = 70.53^\circ$, corresponding to a Bragg angle of $\theta_{111}^{Au,Cu} = 90^\circ - \psi_0 = 19.47^\circ$ (see Figure 4.12). In order to obtain a 111 Debye-Scherrer ring at this Bragg angle, the incident X-ray beam must be tuned to a wavelength of $\lambda = 1.57 \text{ \AA}$, corresponding to a photon energy of 7.91 keV in the case of Au and $\lambda = 1.39 \text{ \AA}$ or a corresponding photon energy of 8.92 keV in the case of Cu. This is the reason why *low-energy* synchrotron radiation must be used for $\langle 111 \rangle$ fiber textured thin films. For these energies, the Bragg angle for the tungsten calibration substance is $\theta_{110}^W = 20.55^\circ$ in the case of Au and $\theta_{110}^W = 18.14^\circ$ in the case of Cu. In

order to fit these rings onto CCD detector screen, the sample-to-detector distance L must be reduced accordingly. Leaving a spacing of 12 mm from the outer ring to the border of the detector screen with a diameter of 165 mm yields $L = 84$ mm for Au and $L = 73$ mm for Cu measurements, respectively. All parameters are summarized in Table 5.

The exposure time was in the range between 10-15 s for thicker films with film thicknesses >300 nm and 15-120 s for ultrathin films in the film thickness range below 300 nm. Strain rates in the order of 10^{-4} s^{-1} could be routinely achieved. Fine tungsten (W) powder turned out to serve well as a calibration substance to compensate for unintentional sample movements. The powder was finely dispersed in vacuum grease, a thin layer of which was applied on the reverse side of the polyimide substrate.

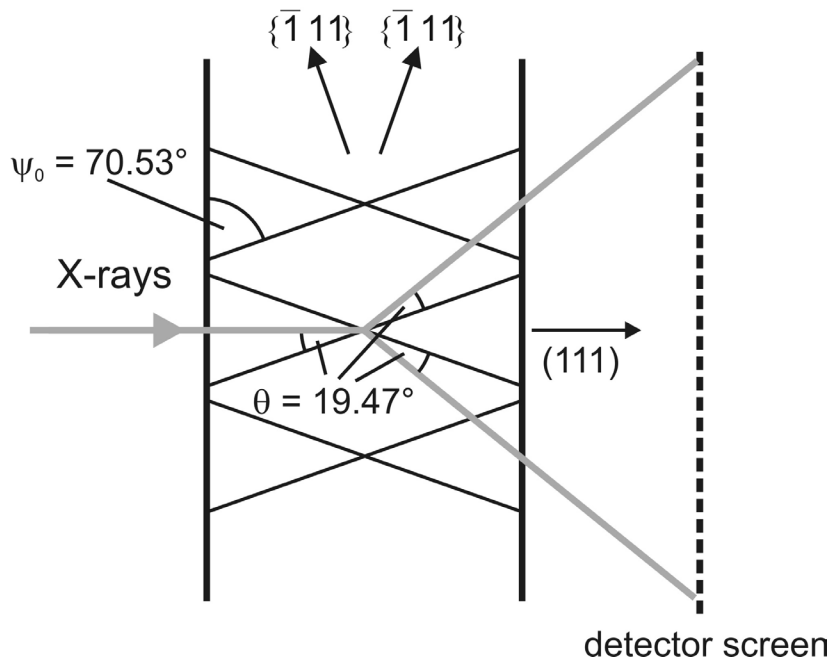


Figure 4.12: Normal-incidence diffraction obtained from $\{\bar{1}11\}$ planes in a $\langle 111 \rangle$ fiber-textured film ($\sin^2\varphi$ method). The (111) normal is perpendicular to the sample surface. In this low-energy normal-incidence geometry, the Bragg angle $\theta = 19.47^\circ$ is only determined by the $\langle 111 \rangle$ fiber texture independent of the material. The wavelength of the monochromatic incident beam must be tuned accordingly to fulfill Bragg's condition.

Table 5: Parameters for using the $\sin^2\psi$ and the $\sin^2\phi$ method on $\langle 111 \rangle$ fiber textured Au and Cu thin films.

	Au		Cu	
	$\sin^2\psi$ method	$\sin^2\phi$ method	$\sin^2\psi$ method	$\sin^2\phi$ method
specimen-to-detector distance, L	220 mm			
Photon energy, E	7.0 keV	7.97 keV	8.0 keV	8.92 keV
Wavelength, λ	1.7735 Å	1.5577 Å	1.5518 Å	1.3918 Å
Angle between detector screen normal and photon beam axis, δ	50°	0°	49°	0°
Angle between diffracting lattice plane and sample surface, ψ	0° (111) 70.53° {-111}	70.53° {-111}	0° (111) 70.53° {-111}	70.53° {-111}
Angle between sample surface and incident beam, α	22.17° (111) 92.67° {-111}	90°	22.17° (111) 92.67° {-111}	90°
Bragg angle, 2θ	44.34° Au (111) 46.76° W (110) 68.28° W (200)	38.71° Au (111) 40.80° W (110)	43.71° Cu (111) 40.64° W (110) 58.82° W (200)	39.01° Cu (111) 36.29° W (110)

5 Results

In the following, all results obtained by the $\sin^2\varphi$ method are presented. Since the method can be applied for various materials, the results are divided into two main parts: high-energy experiments on bulk materials (chapter 5.1) and low-energy experiments on ultrathin films (chapter 5.2).

5.1 High-Energy Experiments – Bulk Materials

5.1.1 Cu/Mo Composites – Methodology Confirmation

The lattice strain results for the Cu/Mo composites obtained by the normal-incidence $\sin^2\varphi$ method established at beamline BW5 of HASYLAB are shown in Figure 5.1e and f.

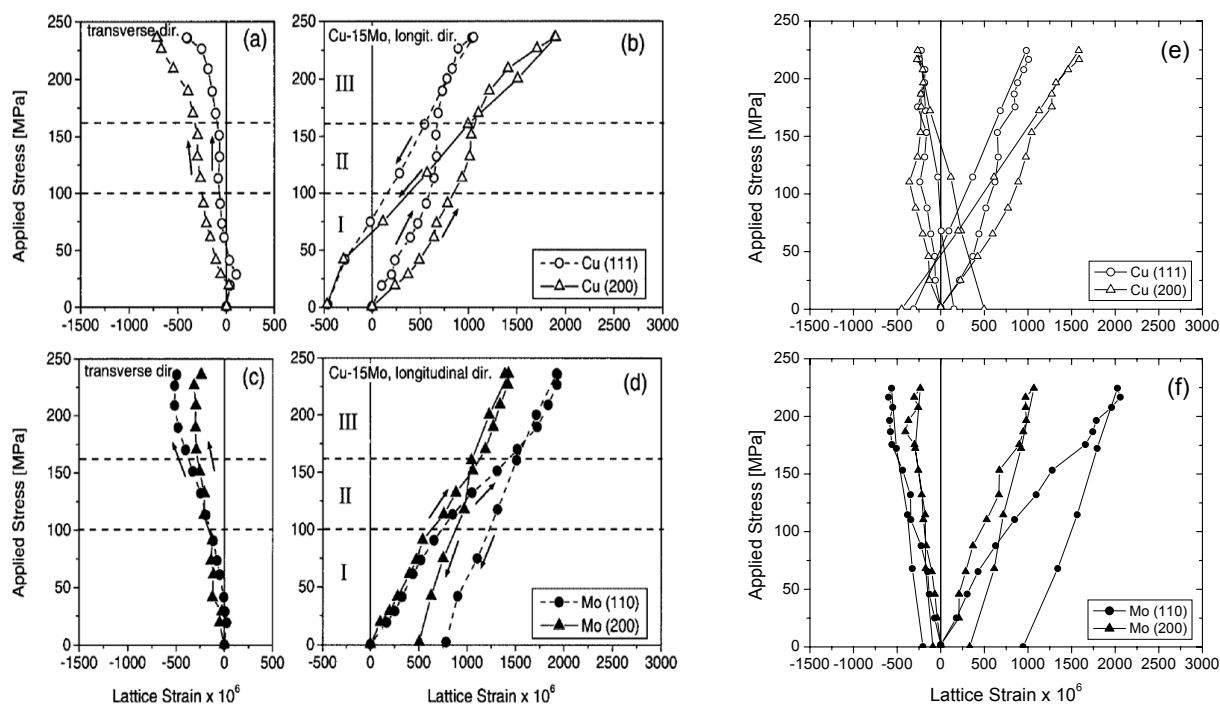


Figure 5.1: Applied stress vs. lattice strain for the Cu-15Mo composite. The longitudinal and transverse Cu (111) and Cu (200) as well as the Mo (110) and Mo (200) strains are shown. (a)-(d) Lattice strain results obtained by Wanner and Dunand (2000) at the Advanced Photon Source (APS) with the same method using a CCD area detector; (e)-(f) Lattice strain results obtained by the high-energy $\sin^2\varphi$ method at beamline BW5 of HASYLAB using an image plate area detector.

The diagrams show the longitudinal and transverse lattice strains from evaluating the Cu (111), Cu (200), Mo (110), and Mo (200) diffraction rings which were all corrected using the Fe (110) diffraction ring. It is obvious that the lattice strains vary between the two phases, which is expected since they exhibit different mechanical properties. The lattice strains also vary between different crystallographic hkl directions due to elastic and plastic anisotropy of the individual grains. The results can be directly compared to those obtained by Wanner and Dunand (2000) at the Advanced Photon Source (APS) shown in Figure 5.1 (a)-(d), since the specimen stems from the same production process. In both experiments, three regions with different slopes during loading can be seen, which indicates changes in the load sharing mechanism between matrix and reinforcements. The unloading curves are linear within the measurement error in all cases. After unloading, the longitudinal residual lattice strains are positive for the reinforcements and negative for the matrix. The lattice strain results obtained by the high-energy $\sin^2\phi$ method are highly reproducible which can be directly seen by comparing the results shown in Figure 5.1e and f with Figure 5.1a-d

5.1.2 Ti-Based Material

In Figure 5.2 the diffraction pattern of the Ti-based material is shown as recorded by the mar345 image plate area detector at beamline BW5 of HASYLAB. Due to the small volume content of the reinforcements and a low signal-to-noise ratio obtained by the image plate detector, only reflections of the Ti matrix were obtained. However, the fine-grained Ti matrix shows very smooth Debye-Scherrer rings which are of excellent quality for strain evaluation. The intensity and the smoothness is comparable to that of the Fe powder calibration substance which was attached to the sample. Figure 5.3 shows the applied stress vs. longitudinal lattice strain plot for the six different hkl lattice planes. The lattice strains were obtained by analyzing the diffraction ring evolution of the diffraction rings which were shown in Figure 5.2 using the $\sin^2\phi$ evaluation procedure presented in chapter 3.1. Within the error of measurement Ti shows a linear elastic stress-strain behavior for all hkl lattice planes up to a large applied stress. The slopes calculated from the elastic constants of titanium fit well to the results (see also chapter 6.2.1 for details), especially for the (100) and (110) lattice planes. The $\sin^2\phi$ method is thus capable of measuring the elastic anisotropy of Ti with sufficient accuracy.

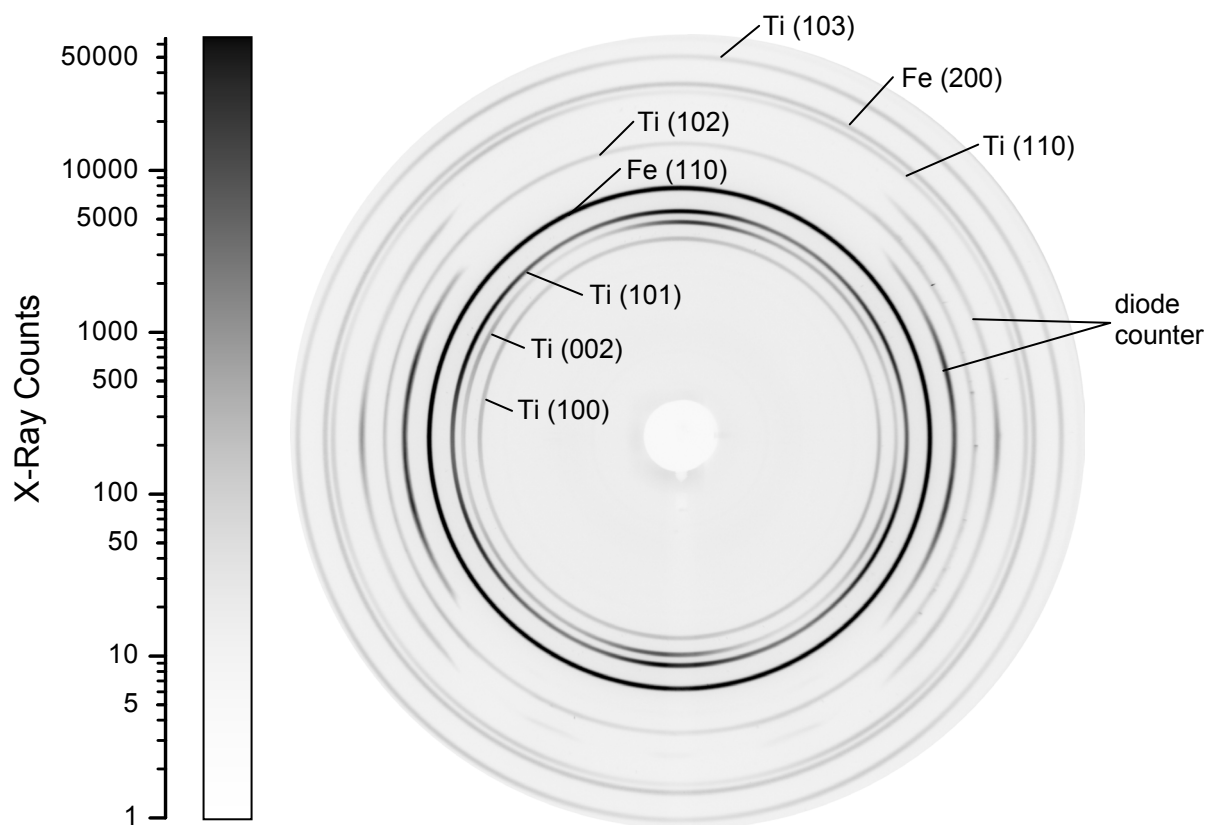


Figure 5.2: Diffraction pattern of a Ti-based material (logarithmic grayscale, exposure time: 60 s). Only the Debye-Scherrer rings of the fine-grained Ti matrix are visible. Intensity and smoothness are comparable to that of the Fe powder calibration substance which was attached to the sample. The two sickle-like rings stem from the diode counter which was within the primary beam monitoring the intensity of the X-ray beam.

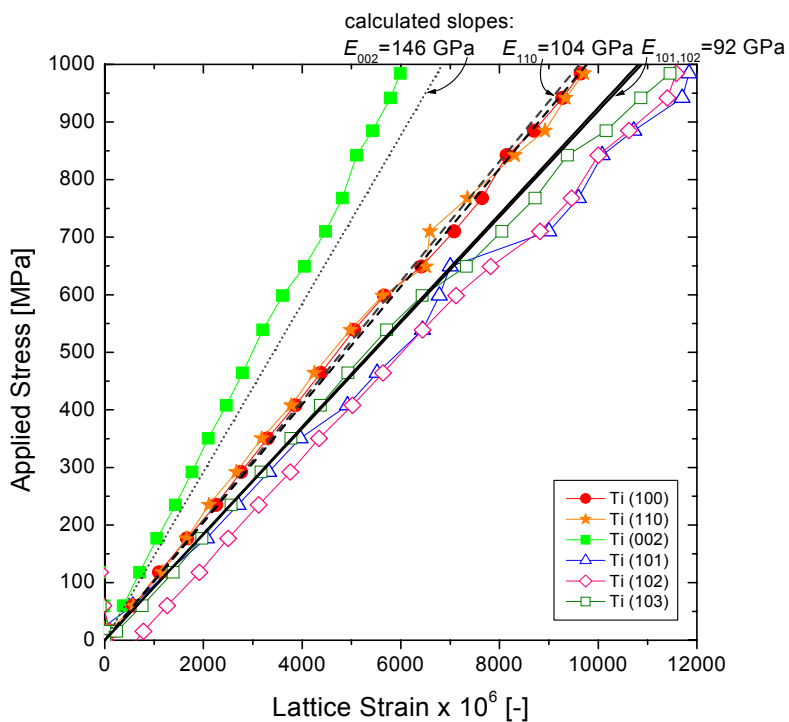


Figure 5.3: Longitudinal applied stress vs. lattice strain for the Ti matrix of a Ti-based material (see text).

5.1.3 γ -TiAl Alloys – Conventional vs. Enlarged Setup

Global Stress-Strain Curves

Two exemplary applied stress vs. total strain curves obtained during *in situ* tensile tests on a γ -TiAl alloy are shown in Figure 5.4. The yield stress of the alloy is about 525 MPa. Stress relaxation of about 4% was observed within the plastic regime during the holding times in which the X-ray measurements were made. In both tests, specimen fracture occurred at a total strain of about 0.8%.

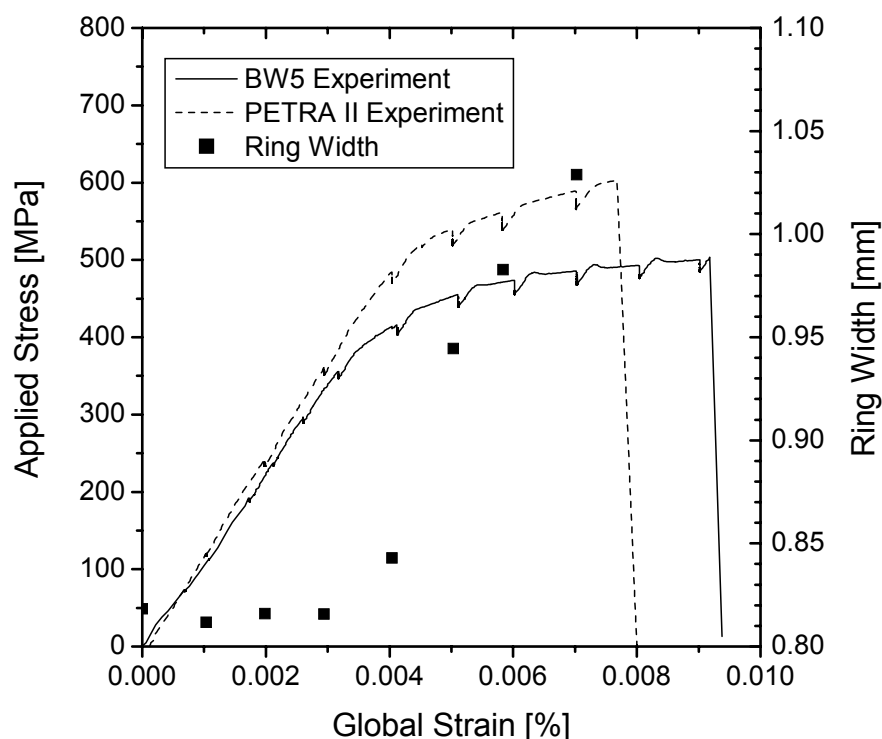


Figure 5.4: Macroscopic stress-strain curves obtained from two different *in situ* tensile tests on γ -TiAl. The kinks in the curves are due to the stress relaxation occurring during hold times. The diagram also shows the evolution of the γ (222) diffraction ring width obtained from the PETRA 2 experiments (enlarged experimental setup).

X-ray Diffraction Patterns

Figure 5.5a shows part of a typical diffraction pattern recorded using the MAR345 image plate detector at beamline BW5. For this particular exposure, no calibration substance was attached to the specimen. Hence, all of the concentric diffraction rings visible in Figure 5.5a stem from the titanium aluminide alloy. The strong diffraction rings belong to the tetragonal phase γ -TiAl, which is the major constituent of the alloy. The two square-shaped areas "1"

and "2" delineated in the pattern correspond to the regions covered by the two area detectors used in the experiments with the enlarged setup performed at beamline PETRA 2. An enlargement of one of the delineated areas is shown in Figure 5.5b. For comparison, a pattern recorded at PETRA 2 by one of the two area detectors is shown in Figure 5.5c. This image was obtained by stacking the frames recorded at 20 different tilt angles as described in chapter 4.2.3. It is apparent that the image shown in Figure 5.5c exhibits a much better signal-to-noise ratio and also much sharper diffraction rings compared to that shown in Figure 5.5b. Further on, much more diffraction rings are visible and even the doublets stemming from the very slight tetragonality of γ -TiAl can now be resolved due to the much improved resolution. A lattice constant ratio of $c/a = 1.012$ could be determined by a best fit from the relative positions of the γ -TiAl rings visible in Figure 5.5c.

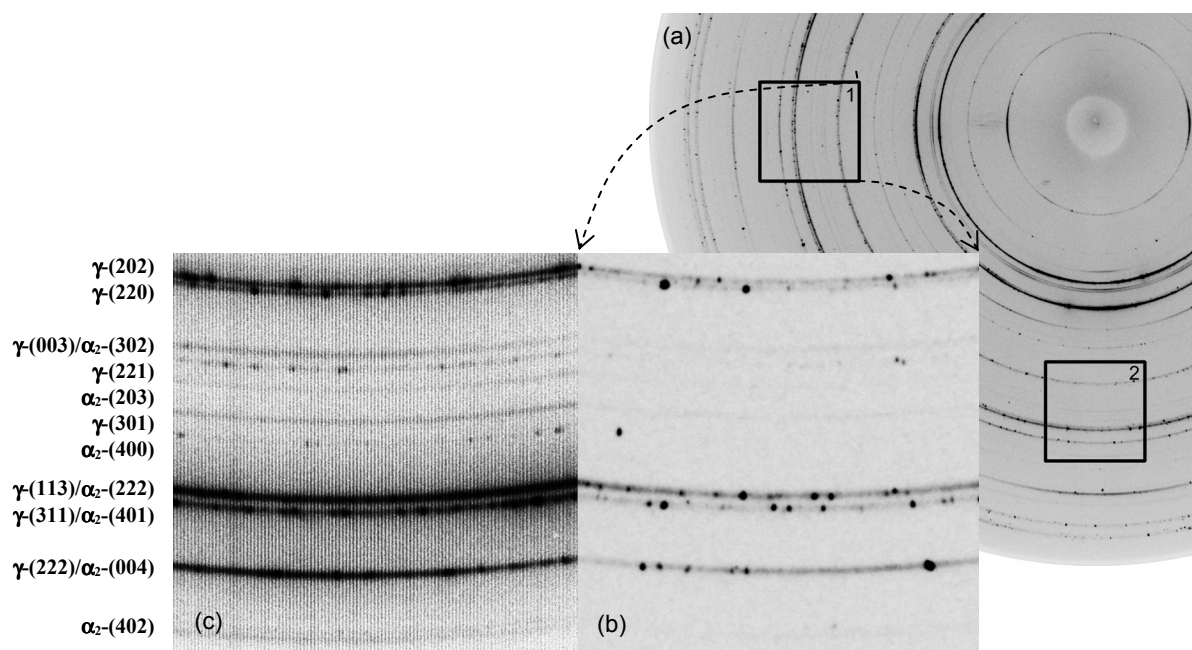


Figure 5.5: (a) Part of a typical diffraction pattern of the γ -TiAl alloy recorded by the image plate detector at beamline BW5 of HASYLAB. Photon energy: 100 keV. (b) Close-up of area "1", rotated counterclockwise around 90° for comparison (c) Corresponding diffraction pattern as recorded by one of the two wire-frame area detectors used in the enlarged experimental setup at beamline PETRA 2 of HASYLAB. Photon energy: 90 keV. All visible reflections are indexed on the right hand side for the phases γ -TiAl and α_2 -Ti₃Al, respectively.

Strain Evolution

The elastic strains in the directions parallel to the loading axis (longitudinal direction) and perpendicular to the loading axis (transverse direction) were deduced from the elliptical distortions of the diffraction rings. If the whole rings are available as in the experiments performed at BW5, the main axes of the ellipse can be obtained according to Equation (3.5) by the diffraction ring analysis procedure described in chapter 3.3 and plotting the ring diameter D against $\sin^2\varphi$. In practice, only some of the diffraction rings visible in Figure 5.5a are suitable for strain evaluation. Most of the rings either exhibit too low intensity or they are too close to adjacent diffraction rings. Of the rings intersecting the square areas as shown in Figure 5.5b, the (222) diffraction ring of the γ -TiAl phase turned out to be the only one from which useful strain results could be obtained. Figure 5.6a shows a D vs. $\sin^2\varphi$ plot for this ring and an applied stress of 470 MPa. In order to eliminate the apparent strains stemming of unintentional specimen movements, the same evaluation procedure was applied to the 111 diffraction ring of the unstrained Si calibration powder substance attached to the specimen. Figure 5.7 shows the net longitudinal and transverse lattice strains derived from the diffraction ring distortions, plotted against the applied stress. The strain results obtained from evaluating the displacements of the 222 ring segments recorded by the enlarged setup at beamline PETRA 2 are also shown. The lattice strains were calculated using the strain evaluation procedure described in chapter 3.1.2. In Figure 5.6b the diameters obtained by this analysis are plotted against $\sin^2\varphi$, again for an applied stress of 470 MPa. Since the two detectors cover narrow φ -ranges around 0° and 90° , two separate data sets are obtained. One set is used to determine the transverse main axis of the ellipse by extrapolating to $\sin^2\varphi = 0$, the other one to obtain the longitudinal main axis by extrapolating to $\sin^2\varphi = 1$. The changes of these main axes are finally used to calculate the lattice strains according to Equation (3.4).

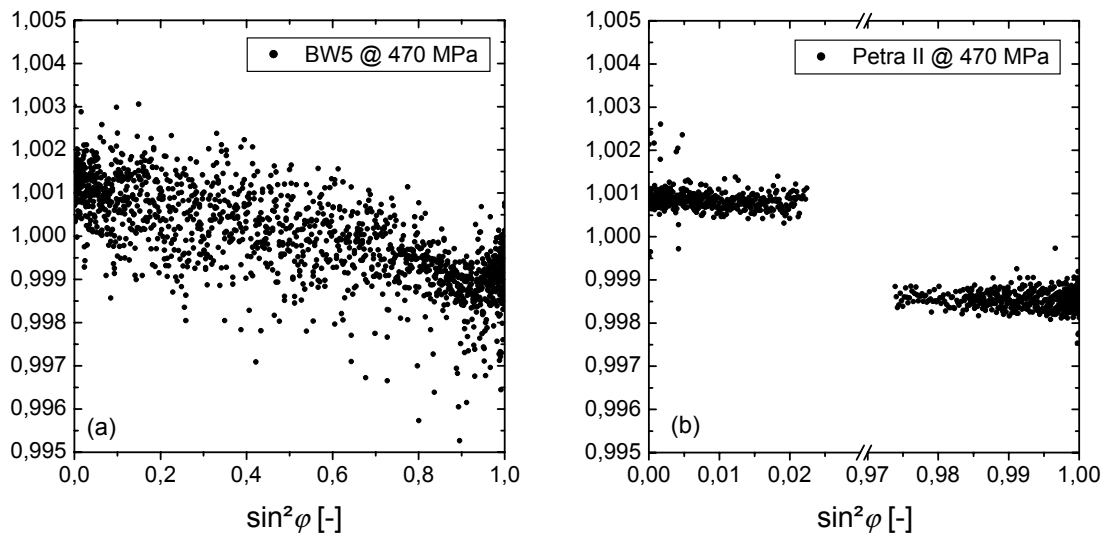


Figure 5.6: (a) Example of the strain evaluation procedure based on the conventional setup and full diffraction rings recorded at BW5. The diameter of the γ -TiAl 222 diffraction ring, normalized to the average ring diameter in the stress-free starting condition, is plotted against $\sin^2\varphi$. Due to the lattice strains caused by applying a stress of 470 MPa, the diffraction ring is distorted elliptically. The two main axes of the ellipse are obtained by fitting a straight line to the dataset and extrapolating to $\sin^2\varphi = 1$ (longitudinal direction) and $\sin^2\varphi = 0$ (transverse direction). (b) The same procedure can be applied to the radii of the ring segments obtained from the evaluation of the partial diffraction rings recorded in the enlarged experimental setup at PETRA 2. The $\sin^2\varphi$ -range is thus restricted to values close to 0 and 1. It is apparent that the data in (b) exhibit considerably less scatter than those in (a).

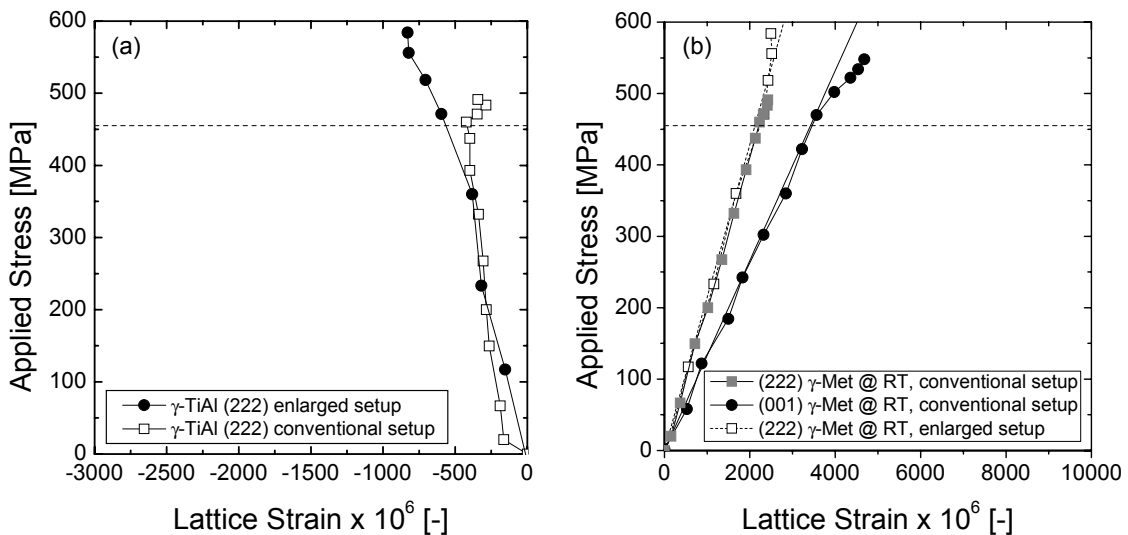


Figure 5.7: Applied stress vs. lattice strain for γ -TiAl. The lattice strains were calculated from the distortions of the (222) and the (001) γ -TiAl diffraction rings or ring segments recorded during *in situ* tensile tests at beamline BW5 or PETRA2 of HASYLAB, respectively. The transverse strains are shown in (a), the longitudinal strains in (b).

5.1.4 γ -TiAl Alloys – High-Temperature Experiments

The high-temperature *in situ* X-ray tensile tests were performed on the same γ -TiAl alloy as used for the room temperature experiments using the furnace described in chapter 4.2.2. The samples were loaded up to stress levels of about 350 MPa and *in situ* X-ray strain measurements were carried out using the conventional setup at beamline BW5. The results are presented in Figure 5.8. Lattice strains were measured along the normal of the (001) lattice planes.

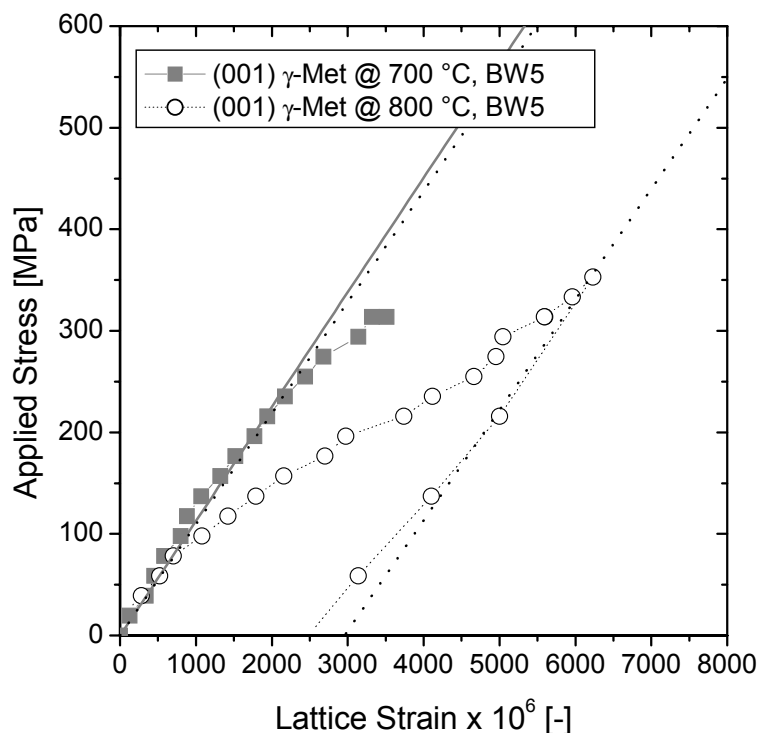


Figure 5.8: Applied stress vs. lattice strain for γ -TiAl measured *in situ* at high temperatures (700 °C and 800 °C) using the conventional experimental setup.

These experiments show for the first time the evolution of lattice strains in the γ -TiAl phase at high temperatures. The two straight lines in Figure 5.8 show the slope of the Young's modulus calculated from the elastic constants given by He et al. (1995). Due to the only slight tetragonality of $c/a=1.012$ (see chapter 5.1.3), Equation (2.9) for cubic crystals was used for approximation. While at room temperature the lattice strains deviate from the linear elastic behavior at an applied stress of about 500 MPa (see Figure 5.7b), the deviation at high temperatures is observed at much lower applied stresses (about 250 MPa at 700 °C and about

100 MPa at 800 °C). At 700 °C, fracture occurred at 320 MPa. At 800 °C, a stress level of 360 MPa was reached and the sample was unloaded again. The unloading curve follows a straight line within the error of measurement. The deviation from linear elastic behavior indicates considerable hkl -dependent load partitioning within the γ -TiAl phase which will be discussed in chapter 6.2.2. Since at high temperatures only strain measurements could be obtained from the (001) lattice planes of the γ -TiAl phase, no conclusion of the elastic strain development for other differently oriented lattice planes can be made. However, other differently oriented γ -TiAl lattice planes exist, which must show a positive deviation from the elastic line. Due to the limitations which occur using the conventional setup with a short specimen-to-detector distance, no strain results for other orientations could be obtained for this material.

Figure 5.9 shows two macroscopic stress-strain curves for γ -TiAl obtained at 700 °C (beamline BW5) and at 800 °C (beamline PETRA 2).

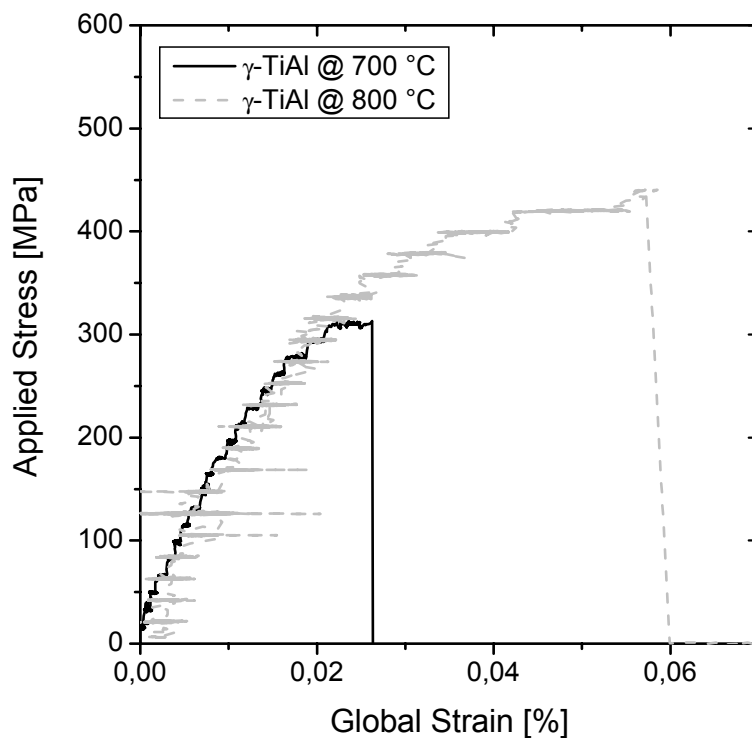


Figure 5.9: Macroscopic stress-strain curves obtained from two different *in situ* tensile tests on γ -TiAl at high temperatures (γ -Met @ 700 °C and γ -Met HIP @ 800 °C). The kinks in the curves are due to the stress relaxation occurring during hold times. The 800 °C curve is noisy because of noise trouble with the wire connection.

High-temperature $\sin^2\varphi$ measurements were carried out during tensile tests using the enlarged setup at beamline PETRA 2. Figure 5.10 shows part of the diffraction pattern as recorded by the mar345 image plate detector positioned about 7 m from the sample recording the evolution of the rings in longitudinal direction. The image shows clearly distinguishable partial diffraction rings which do not interfere with the undesired graphite and Al diffraction rings from the furnace. In this particular image, for the first time a low-intensity diffraction ring from the α_2 -Ti₃Al minority phase is visible. However, lattice strain measurements based on this ring could not yet be performed due to a lack of available beamtime at PETRA 2. Since the access to the PETRA 2 beamline was limited, only one high-temperature *in situ* tensile test could be performed at 800 °C. This experiment was performed on a HIPed γ -TiAl alloy exhibiting a nearly random texture.

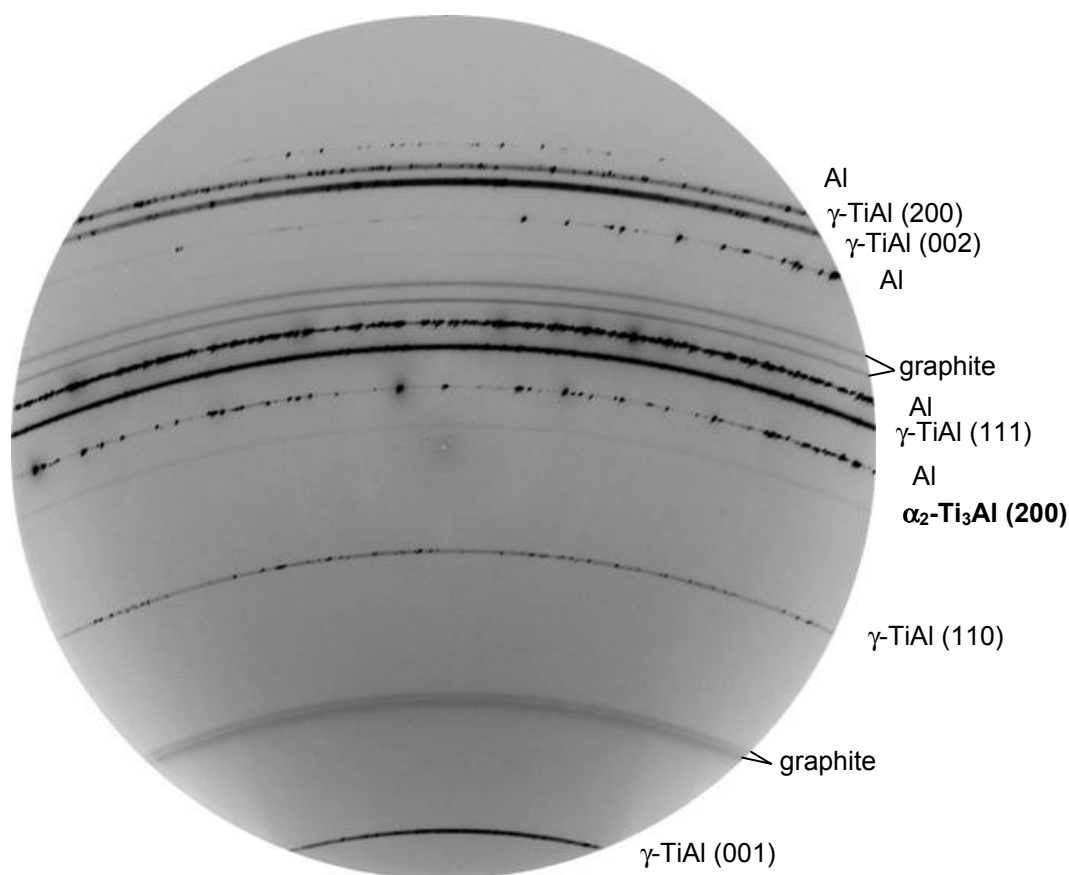


Figure 5.10: Partial diffraction pattern as obtained for a γ -TiAl alloy at beamline PETRA 2 of HASYLAB using the enlarged experimental setup. The diffraction pattern was recorded by a mar345 image plate detector which was positioned about 7 m from the sample recording the evolution of the diffraction rings in longitudinal direction (see also for a photograph of the experimental setup).

The lattice strain results measured *in situ* for the (001) lattice planes are presented in Figure 5.11. Deviation from linear elastic behavior above 180 NPa applied stress at 800 °C indicates again considerable *hkl*-dependent load partitioning within the γ -TiAl phase (see also chapter 6.2.2). The results agree well with the high-temperature results presented in Figure 5.8 obtained at beamline BW5.

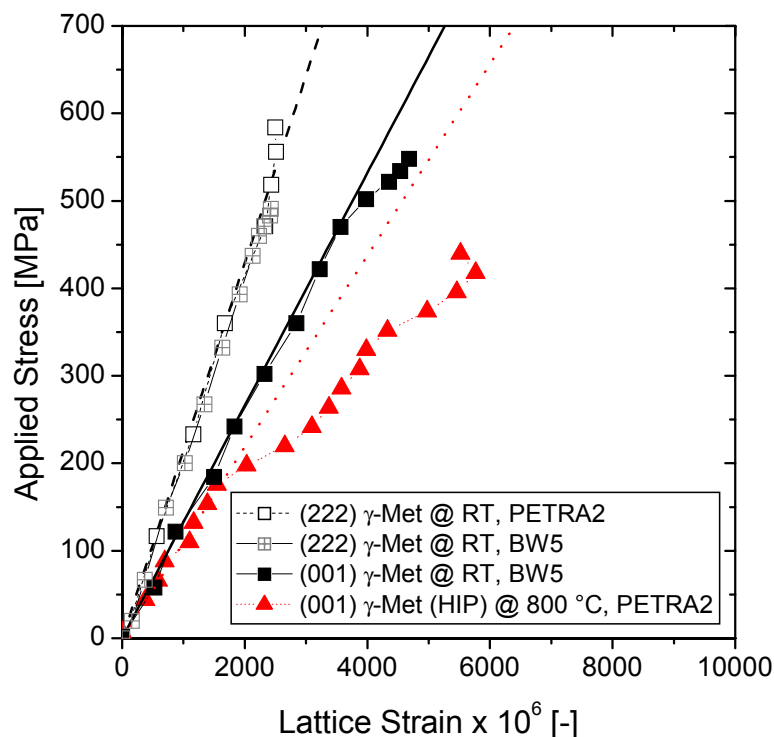


Figure 5.11: Applied stress vs. lattice strain during tensile testing of a HIPed γ -TiAl alloy at 800 °C using the enlarged experimental setup at beamline PETRA 2 of HASYLAB. For comparison, the room temperature results obtained at beamlines PETRA 2 and BW5 are also shown.

5.1.5 NiAl Polycrystals

The lattice strains were obtained by analyzing the minute elliptical distortions of the diffraction rings using the evaluation procedures described in chapter 3.1, but without using a calibration substance. In Figure 5.12a the global stress-strain curve is shown. The results for the longitudinal and the transverse directions are shown in Figure 5.12b for the (100) and (110) diffraction rings. For the longitudinal direction, the relationships between applied stress and lattice strain are linear within the error of measurement. The apparent Young's moduli as determined from the slopes of the fit lines shown in Figure 5.12b are 96.4 GPa for (100)

orientation and (177) GPa for (110) orientation. The single crystal Young's moduli for the same crystallographic orientations are 97.8 GPa and 202 GPa, respectively. These values were calculated from single-crystal elastic constants reported by Rusović and Warlimont (1977) for NiAl of the same chemical composition.

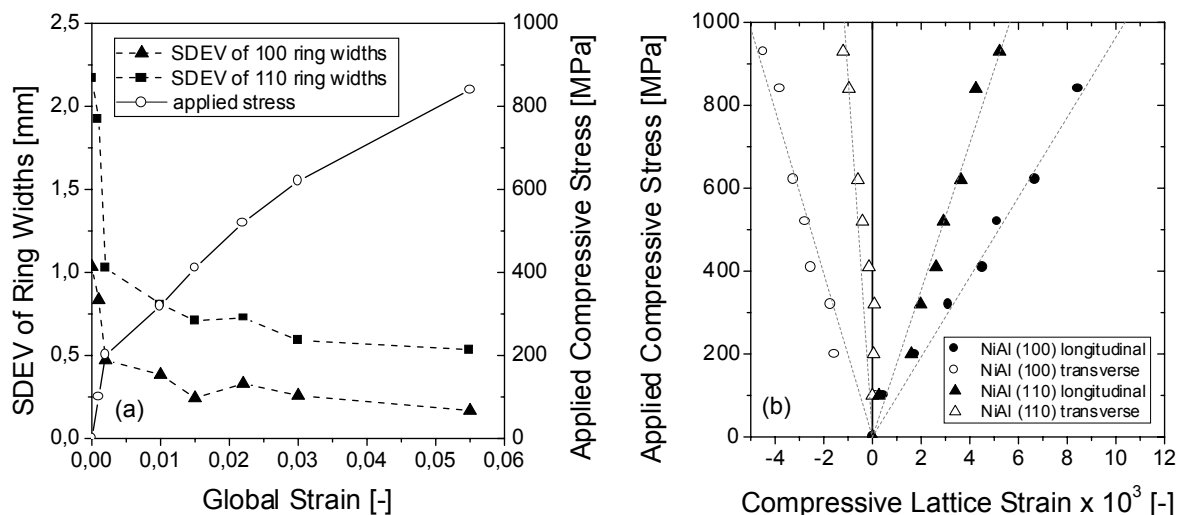


Figure 5.12: (a) Global stress-strain curve (open symbols) as well as evolution of the diffraction ring graininess, characterized by the standard deviation (SDEV) of the ring widths. (b) Applied stress vs. lattice strain for 100 and 110 oriented grains

A closer look at the different diffraction patterns reveals that the diffraction rings undergo a significant change in morphology. This effect is shown in Figure 5.13, where the evolution of a small part of the diffraction rings is shown for the different load steps. In the undeformed state, the rings are "spotty", i.e., they are not very well defined and exhibit speckles. During deformation, the rings became much smoother. A measure for the degree of spottiness is the standard deviation (SDEV) of the ring width values determined at different azimuthal positions around the ring (Wanner and Dunand (2000)). This quantity was determined for each load step. The results are also shown in Figure 5.12a for the (100) and (110) diffraction rings as a function of the total specimen strain. It is apparent that significant smoothing takes place already at a very early stage of plastic deformation (the largest smoothing can be seen between the second and the third load step, see also Figure 5.12a).

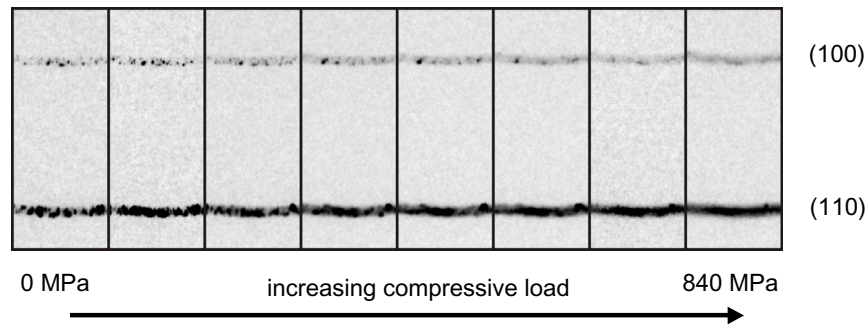


Figure 5.13: Evolution of the morphologies of the 100 and 110 diffraction rings with increasing compressive load. The initially grainy rings become much smoother during deformation.

5.2 Low-Energy Experiments – Thin Films

In the following, the experimental results of the *in situ* tensile tests on thin Au and Cu films are presented. The focus of the studies was to characterize the mechanical behavior of ultrathin Au and Cu films in the thickness range below 300 nanometers. All samples consisted of a thin film sputtered on a 125 μm thick polyimide substrate, which is nearly transparent for X-rays. The mechanical properties of the metal films were studied on polyimide substrates in order to achieve large total strains up to several percent.

5.2.1 Au Thin Films

First, results obtained from an *in situ* X-ray tensile test of a 20 nm thin Au film are presented in order to demonstrate potential of the stress evaluation procedure. In Figure 5.14a, a typical diffraction pattern obtained in $\sin^2\psi$ geometry is shown. One sickle-like ring stemming from the strongly $\langle 111 \rangle$ fiber textured Au film and two continuous rings from the W powder can be seen. The plot below the image shows the integral intensity profile over the area delineated in Figure 5.14a. The two peaks of the W powder were used for calibration. The peak centroids obtained by Gaussian peak fits to the profile were used to calculate single data points for the $\sin^2\psi$ plot as shown in Figure 5.15a showing a typical $\sin^2\psi$ -plot obtained for the $\{111\}$ lattice planes of a 20 nm thick Au film. The equibiaxial residual stress state obtained for this particular example was negative.

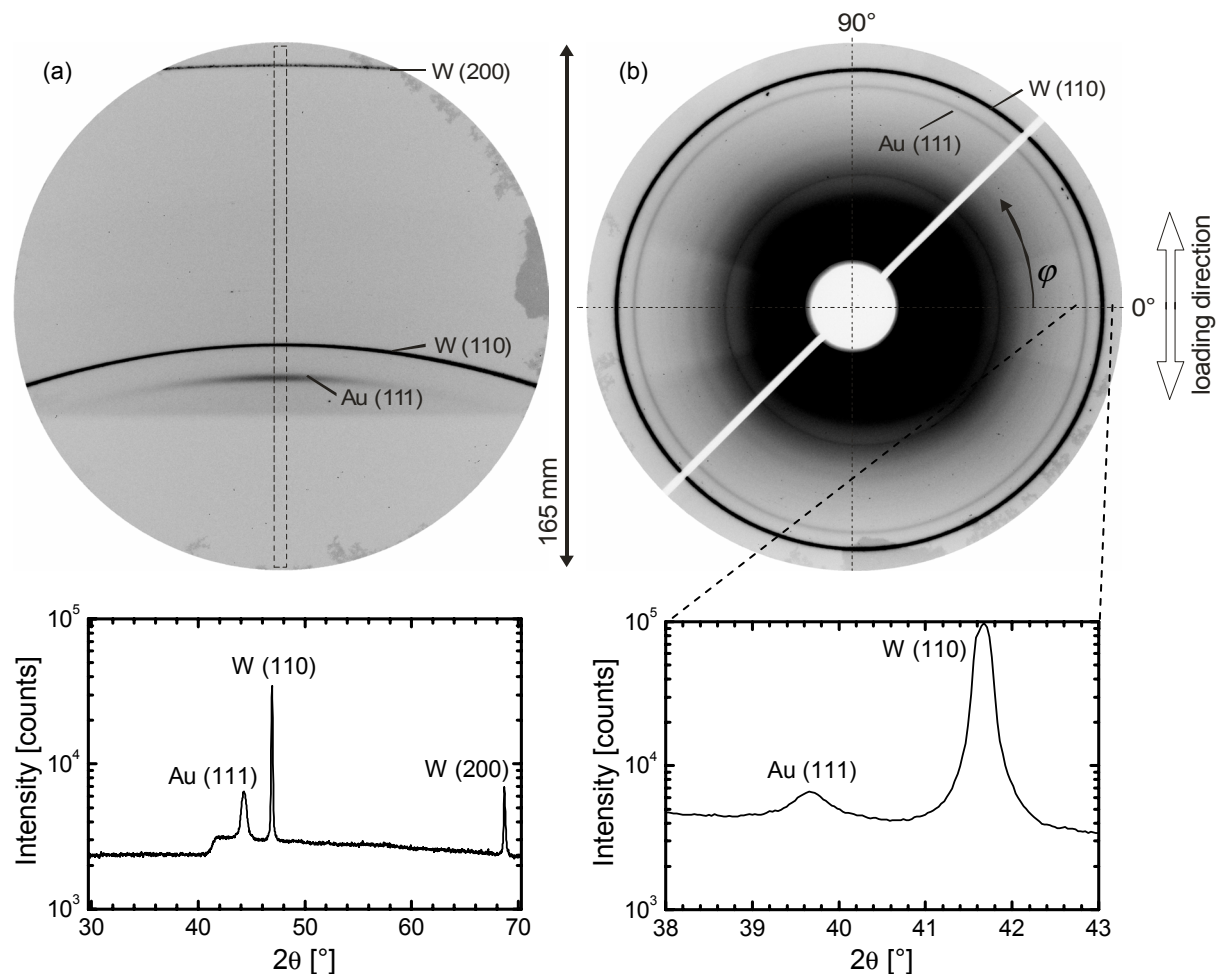


Figure 5.14: (a) Diffraction pattern showing partial Debye-Scherrer rings of a 20 nm Au film and W calibration powder. This pattern was recorded using the following parameters: $\lambda = 1.7735 \text{ \AA}$, $\alpha = 22.67^\circ$, $\delta = 50^\circ$, exposure time: 30 s. The intensity profile corresponds to the integral over the delineated area of the diffraction pattern. (b) Complete Debye-Scherrer rings recorded in normal-incidence geometry used for $\sin^2\phi$ measurements at $\lambda = 1.5577 \text{ \AA}$, $L = 83 \text{ mm}$, exposure time 30 s. The intensity profile was obtained at $\phi = 0^\circ$ by integrating over an azimuthal range of $\Delta\phi = \pm 0.25^\circ$.

Figure 5.14b shows an example of a full diffraction pattern recorded in the normal-incidence geometry. The diffuse rings near the center stem from the polyimide, the strong ring belongs to the W calibration powder and the weaker ring to the sample. The plot below the image shows a typical radial intensity profile obtained by integrating over an azimuthal ϕ range of 0.5° and subsequent fast fourier (FFT) smoothening.

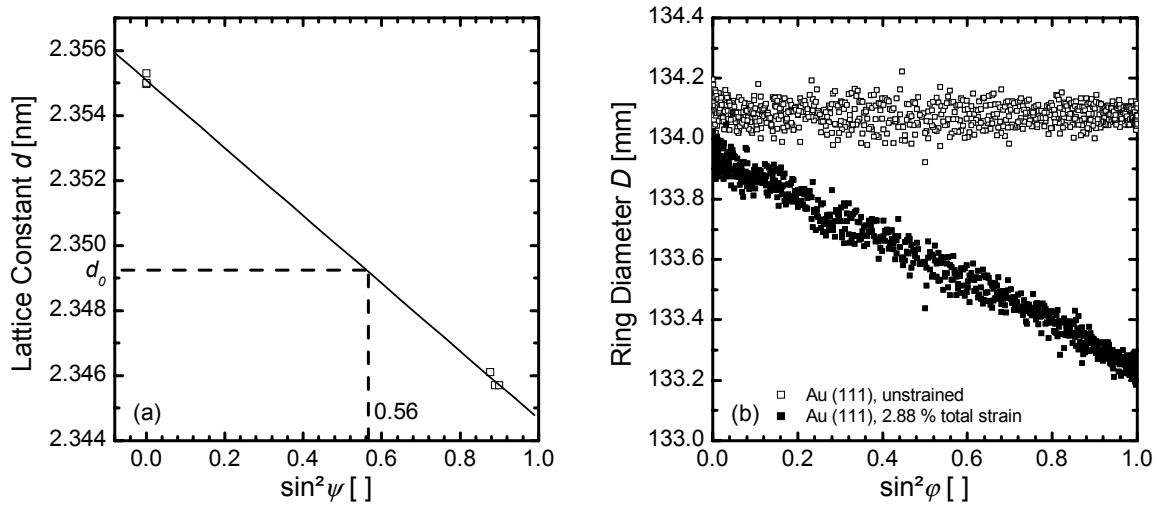


Figure 5.15: (a) Evaluation of the initial stress state by the $\sin^2\psi$ method. The lattice constant d is plotted versus $\sin^2\psi$ for the (111) lattice planes of Au. The unstressed lattice constant d_0 can be obtained for Au at $\sin^2\psi = 0.56$. The initial stress was calculated by fitting a straight line and extrapolating to $\sin^2\psi = 0$ and $\sin^2\psi = 1$. (b) Strain evaluation procedure for the $\sin^2\phi$ method. The diameter of the Au (111) Debye-Scherrer ring is plotted against $\sin^2\phi$, where ϕ is the azimuthal angle. As the sample is deformed to a total strain of 2.88%, the Debye-Scherrer ring is distorted elliptically. The two main axes of the ellipse are obtained by a linear fit and extrapolation to $\sin^2\phi = 1$ (longitudinal direction) and $\sin^2\phi = 0$ (transverse direction).

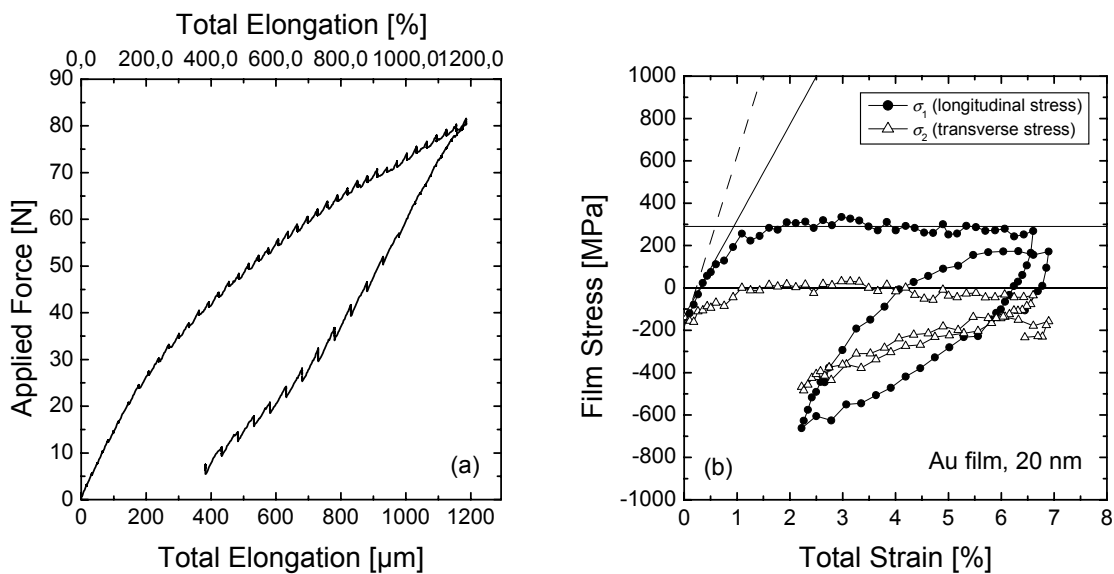


Figure 5.16: 20 nm thin Au film directly sputtered on a 125 μm thick polyimide substrate; (a) Applied force vs. total elongation curve (first cycle); (b) Stress evolution in longitudinal and transverse direction. Straight line: linear fit to the first five data points. Dashed line: Slope of the Young's modulus for an Au single crystal loaded in $\langle 110 \rangle$ direction $E_{110}^{\text{Au}} = 81$ GPa.

Figure 5.16a shows the applied force vs. total strain curve of the sample as recorded by the load cell and the LVDT. This curve mainly represents the mechanical behavior of the polyimide substrate. The specimen was monotonically loaded up to a total strain of 6.5% and subsequently unloaded again. The kinks in the curve are due to stress relaxation during the hold times of 90 s in which the X-ray exposures were taken.

In Figure 5.16b the stress evolution in the Au film is shown as a function of total strain applied in direction S_1 . In the as-deposited state, the Au film exhibits a compressive residual stress of about 140 MPa. This compressive stress has been developed during cooling from the deposition temperature due to thermal mismatch between the Au film and the polyimide substrate. During the tensile test, a monotonic stress increase is observed in the elastic regime both in longitudinal (σ_1) and transverse (σ_2) direction. The initial slope corresponds to a biaxial modulus of about 48.8 GPa. However, the nonlinearity of the stress-strain curve shows clearly that the film yet undergoes plastic deformation. A stress-plateau at a stress level of around 290 MPa is reached after a total strain of about 1.5%. The unloading curve shows even more clearly that there is almost no regime of linear elasticity. The slope steadily decreases from around 85 GPa down to around 20 GPa. Upon unloading, a compressive but non equibiaxial residual stress is reached. The absolute compressive stress values are higher than in the as-deposited state in both principal directions. Error propagation calculations yield a maximum error of ± 50 MPa for the initial residual stress measurement and ± 50 MPa for the stress changes during the tensile test. The total error thus adds up to ± 100 MPa. However, the stress difference between individual data points can be determined with a much higher accuracy which leads to well defined stress-strain curves.

In Figure 5.17 two stress-strain cycles for two different 20 nm thin Au films are shown. Sample 2 corresponds to the stress-strain cycle already shown in Figure 5.16b. It is obvious that sample 1 shows no residual stresses in the as-deposited state, like all the other thicker Au samples from 40 nm – 1000 nm (see Figure 5.18a-f). Sample 2 shows a residual stress of about -150 MPa the origin of which is not clear, because the samples were not annealed after sputtering, which means that no thermally induced residual stresses should appear. However, the plateau stress is the same for both 20 nm thin Au films, and the two elastic slopes obtained by linear fits of the first 5 data points from the first cycle coincide very well. The unloading

curves have also the same shape. Sample 1 was strained up to a higher total strain than sample 2 before unloading. The compressive stress before reloading again is higher for sample 1 (about 650 MPa) than for sample 2 (about 400 MPa). The unloading cycle of sample 1 could not be completed because of beam loss during the experiment.

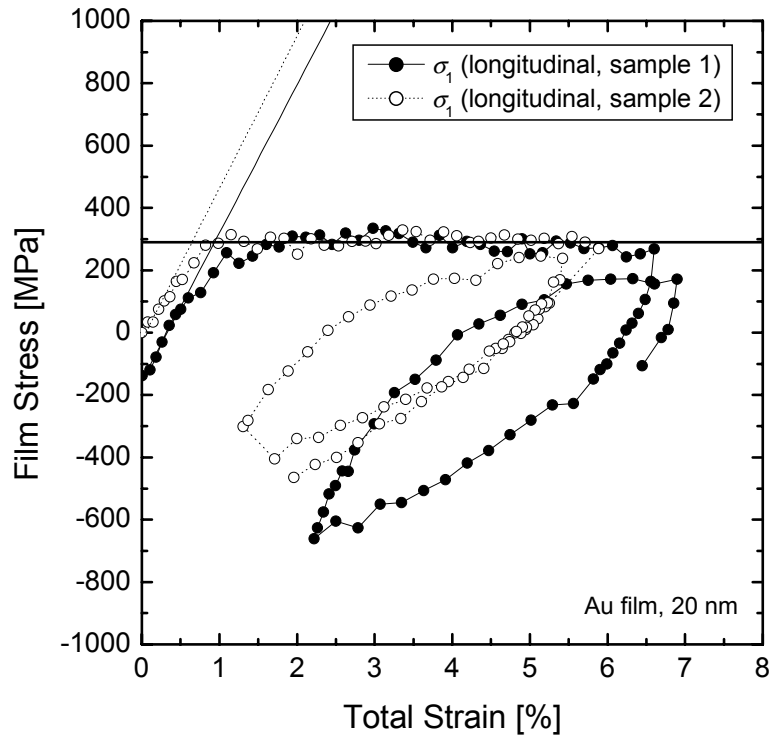


Figure 5.17: Stress evolution in two different 20 nm thin Au films directly sputtered on a 125 μm thick polyimide substrate. For clarity only the longitudinal stresses are shown. Both lines show linear fits to the first five data points.

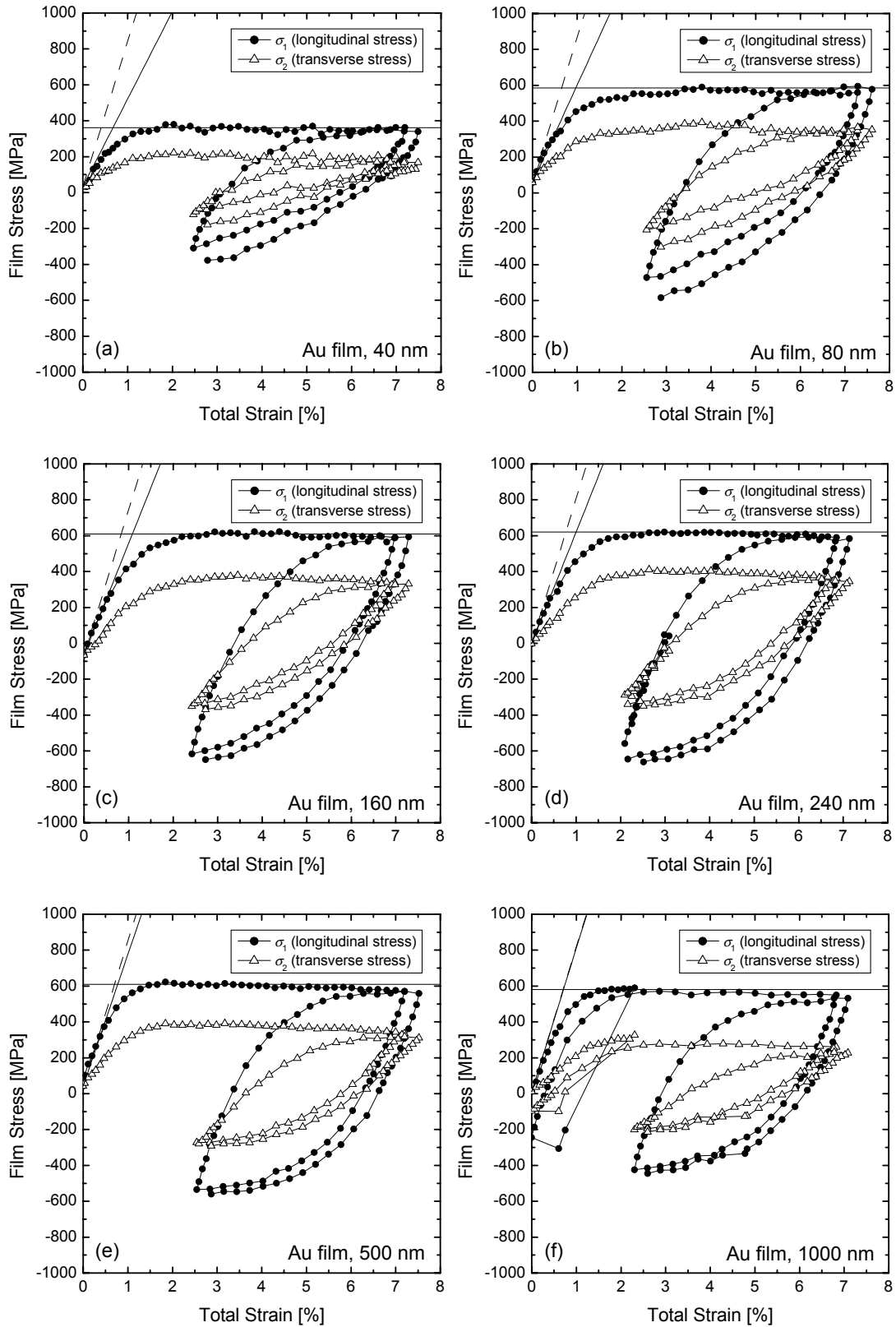


Figure 5.18: Stress evolution in (a) 40 nm, (b) 80 nm, (c) 160 nm, (d) 240 nm, (e) 500 nm and (f) 1000 nm thin Au films on a 125 μm thick polyimide substrate. Straight line: linear fit to the first five data points. Dashed line: Slope of the Young's modulus for an Au single crystal loaded in $\langle 110 \rangle$ direction $E_{110}^{\text{Au}} = 81$ GPa.

In Figure 5.18a-f the thickness dependency of the Au films is shown in the thickness range between 40 nm and 1000 nm. Above 80 nm, no difference in the longitudinal plateau stress can be seen. Only for the 20 nm (see Figure 5.16b) and 40 nm Au film is the longitudinal plateau stress value lower than 600 MPa (about 380 MPa for the 40 nm film and about 300 MPa for the 20 nm film). Thus, for thin Au films there is a large thickness range above 80 nm in which the longitudinal plateau stress stays constant and a decrease for the 40 nm and 20 nm thick films. All stress-strain curves are highly reproducible which can be seen by comparing the curve of the second cycle to that of the first cycle. In all experiments, the plateau stress is reached again in the second loading cycle and the unloading curves of the first and the second cycle have the same shape. Within a uniaxial tensile test on $\langle 111 \rangle$ fiber textured films, the crystallites are subjected to a tensile load in $\langle 110 \rangle$ direction (longitudinal direction). The slope calculated according to Equation (2.9) for an Au single crystal subjected to a tensile load in $\langle 110 \rangle$ direction (dashed lines, for elastic constants see Appendix A) agrees well with the slope obtained by linear fits to the first five data points for the thicker Au films. However, the two slopes differ for the thinner films, which is a sign for aberrations from linear elasticity in the early stage of deformation.

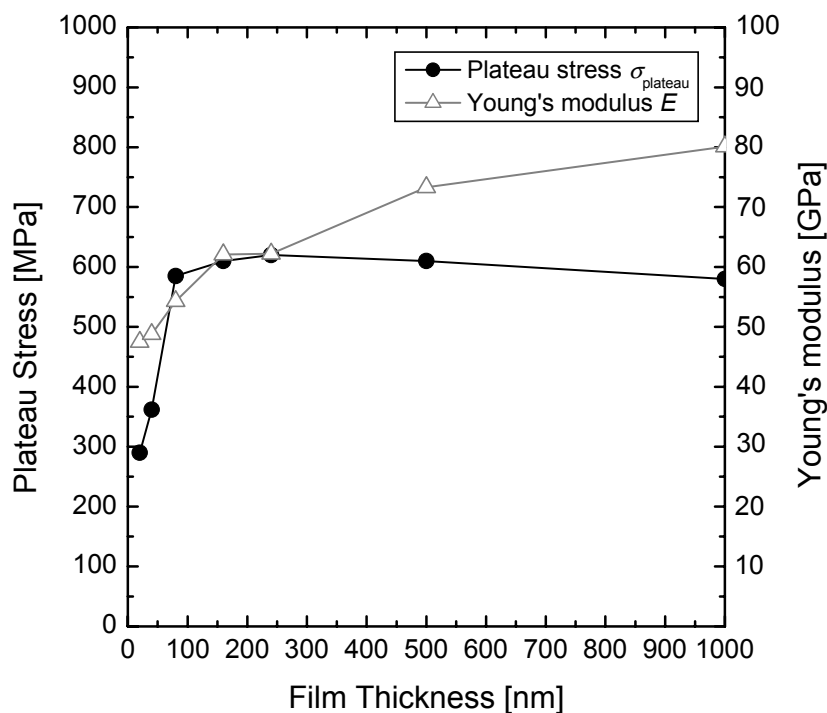


Figure 5.19: Film thickness dependence of plateau stress (filled circles) and Young's modulus (open triangles).

The thickness dependence of the plateau stresses and Young's modulus is shown in Figure 5.19. The plateau stress stays constant at about 600 MPa for all gold films thicker than 80 nm. For the 40 nm and 20 nm thin gold films the plateau stress values clearly decrease and the 20 nm thin gold film shows only half of the value of the thicker films. The Young's modulus steadily increases with increasing gold film thickness which can also be seen by comparing the different elastic slopes in Figure 5.18a – f.

5.2.2 Cu Thin Films

The atomic mass Z of copper is by a factor of 2.7 smaller compared to gold ($Z_{\text{Cu}} = 29$, $Z_{\text{Au}} = 79$), which suggests that the scattered X-ray intensity is also much smaller for the same film thickness. The requirements for *in situ* X-ray tensile tests on copper are therefore much higher than for gold. Nevertheless, it was still possible at the synchrotron to obtain enough scattered intensity from an only 20 nm thick copper film with a 10 nm thick top- and underlayer. The tungsten underlayer was used in order to enhance the $\langle 111 \rangle$ fiber texture of the film, the toplayer was used to prevent the Cu film from oxidating. Figure 5.20a shows the diffraction image of the film. Note that no Debye-Scherrer rings from the tantalum underlayer are visible. The intensities of these rings are expected to be much lower than those of the Au film because of the lower thickness, lower atomic number, and lower crystal symmetry (thin sputtered tantalum has a β -Ta modification which has a tetragonal structure with a β -Uranium structure containing 30 atoms per unit cell, as recently found by Jiang et al. (2003) by extended X-ray absorption fine structure (EXAFS) measurements). Furthermore, not much diffracted intensity is expected from the tantalum layers since the photon energy was tuned for the $\langle 111 \rangle$ fiber texture of copper and not for the tantalum.

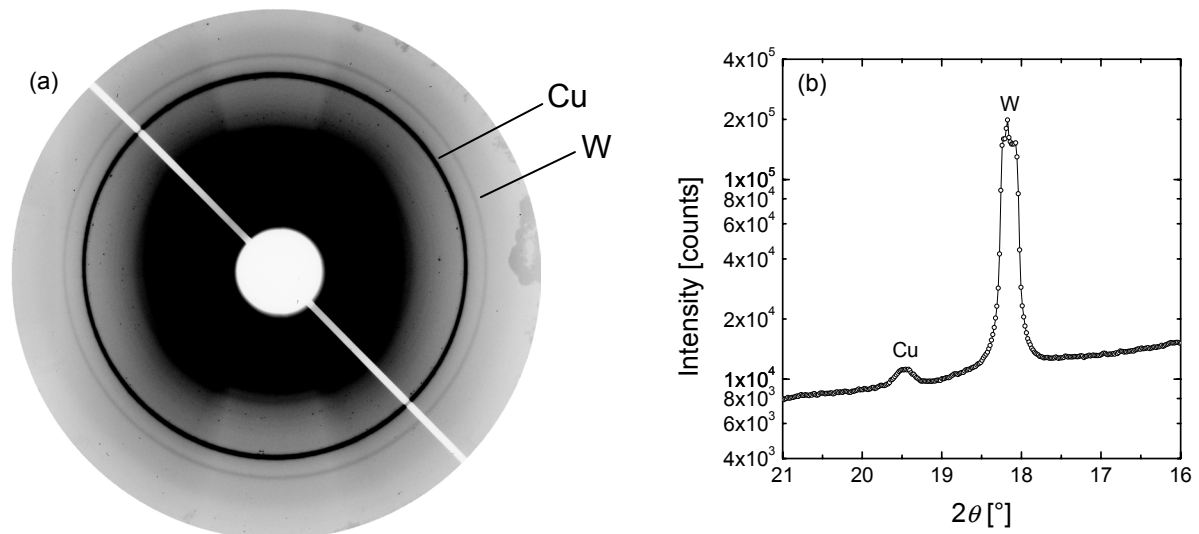


Figure 5.20: (a) Debye-Scherrer ring of a 20 nm thick copper film with a 10 nm thick top- and underlayer on a 125 μm thick polyimide substrate (weak diffraction ring). The strong Debye-Scherrer ring belongs to the tungsten calibration powder which was applied on the back side of the polyimide substrate. The grayscale values were scaled in order to visualize a good contrast for the weak copper diffraction ring leading to a large "overexposed" black area in the center of the frame which stems from amorphous scattering of the polyimide substrate as well as from air scattering of the incident beam. (b) Peak intensity profile integrated over the an azimuthal range of 1° along the line shown in (a).

Two exemplary $\sin^2\phi$ -plots for 0 MPa and 1500 MPa longitudinal film stress are shown in Figure 5.21a. The scatter of the individual points is about 10 pixels. However, due to the good statistics of 1600 data points, the absolute error of the semiaxes is much lower (0.2 pixel corresponding to 16 μm with a 80 μm pixel size of the marccd detector) as determined by the absolute error of the linear fits to all data points. This leads to an absolute error of 50 MPa for the film stress values, the evolution of which is shown in Figure 5.21b. A drastic stress drop at 2.3 % total strain and a longitudinal film stress of 1500 MPa is visible in both longitudinal and transverse direction. This stress drop is likely due to cracking of the 10 nm thick tantalum underlayer as observed by SEM investigations which are presented further below.

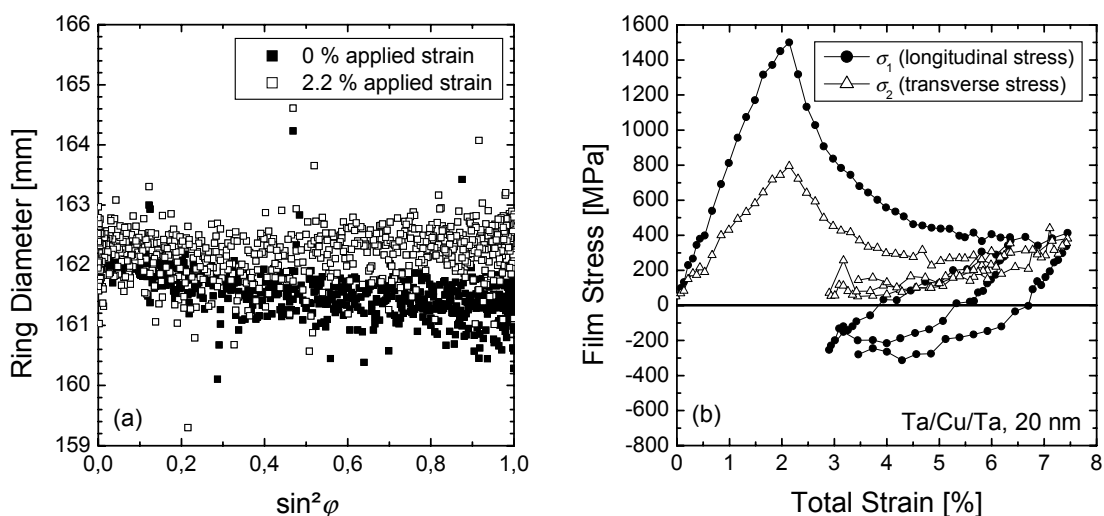


Figure 5.21: (a) $\sin^2 \phi$ strain evaluation for the copper layer of a 10/20/10 nm Ta/Cu/Ta layer system on a polyimide substrate. (b) Film stress vs. total strain for the 20 nm thick Cu layer. The graph shows the first and the second loading cycle.

Figure 5.22a shows the evolution of the longitudinal and transverse strains for a 10/50/10 nm Ta/Cu/Ta thin film system on a 125 μm thick polyimide substrate. The longitudinal peak stress is 1200 MPa, and a dramatic stress decrease is again visible above 2.5% total strain. During the second loading cycle the longitudinal stresses again decreases slightly with increasing strain (total strain range between 5.5 % and 7.5 %). This behavior indicates ongoing cracking in the tantalum underlayer for larger total strains. In Figure 5.22b, the longitudinal- and transverse stress-strain cycles for a Cu film thickness of 300 nm are presented. The longitudinal stress reaches a maximum of 700 MPa at 2.3 % total strain and a slight stress decrease is visible up to the maximum total strain of 7 %. Figure 5.22c shows a stress decrease in the 300 nm tick Cu layer for large total strains (up to 26 %). Thus, a different stress decrease after can be observed between (b) and (c). The stress decrease in (c) is much higher than in (b) although both samples were strained with the same strain rate. For this film thickness the stress decrease varies from sample to sample. In Figure 5.22d, the same plot is shown for a 500 nm thin copper film. A wide stress plateau stretching from 2.0 to 7.5 % total strain can be seen. Clearly no stress drop is visible for this film thickness.

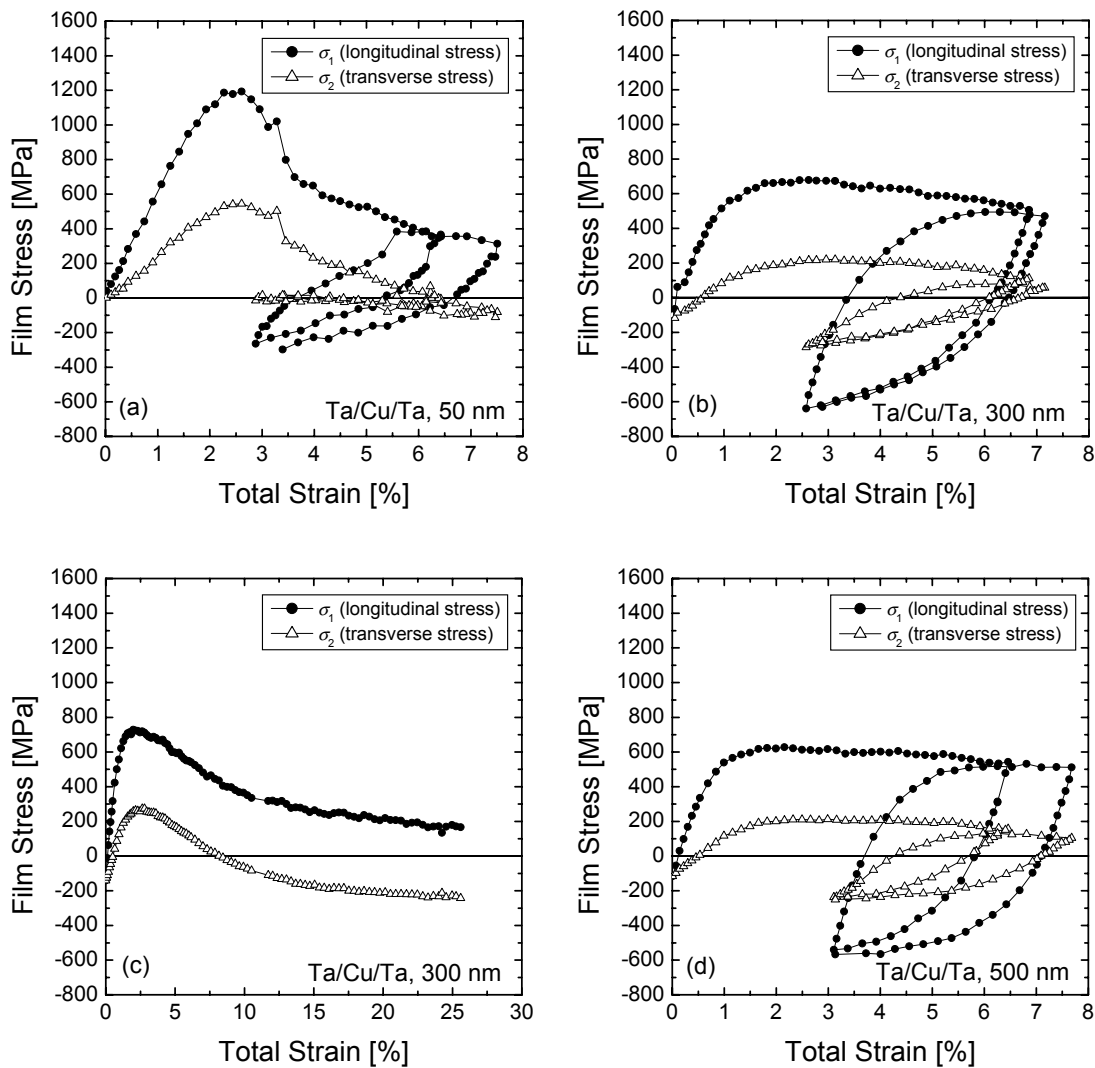


Figure 5.22: Evolution of the longitudinal- and transverse stresses of Ta/Cu/Ta thin film systems (a) copper film thickness: 50 nm (b) copper film thickness: 300 nm. (c) copper film thickness: 300 nm, large total strain of 26 %, loading curve only. (d) copper film thickness: 500 nm.

In Figure 5.23a and b the stress evolution in the copper layer of a Ta/Cu thin film system with a 160 nm (a) and 640 nm (b) thick copper layer sputtered on a 10 nm thick tantalum underlayer without a toplayer is shown. The $\sin^2\psi$ stress measurements performed in the as-deposited state show a compressive residual stress of 280 MPa (160 nm Cu) and 110 MPa (640 nm Cu), respectively. The thinner 160 nm thick Cu film shows again a stress decrease at 2.3 % total strain while the thicker 640 nm thick Cu film shows a constant stress plateau of about 450 MPa up to 9.3 % total strain.

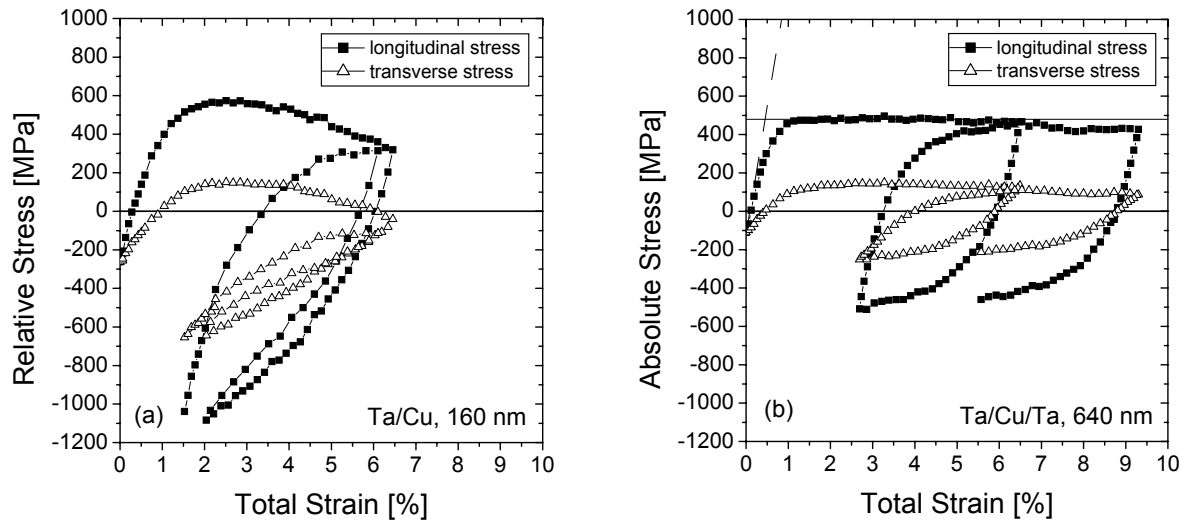


Figure 5.23: Evolution of the longitudinal- and transverse stresses of Ta/Cu thin film systems (a) copper film thickness: 160 nm (b) copper film thickness: 640 nm.

In Figure 5.24a and b two SEM images of a pre-stressed 10/100/10 nm Ta/Cu/Ta sample are shown which was strained *ex situ* up to a total strain of about 6 % as measured roughly by a sliding rule. The images show cracks which propagated perpendicular to the loading direction. The median crack distance could be determined to about 11.5 μm by the line intersecting method. These images support the idea that the stress drop measured for the Cu films shown above is due to the stress relief associated with such cracks.

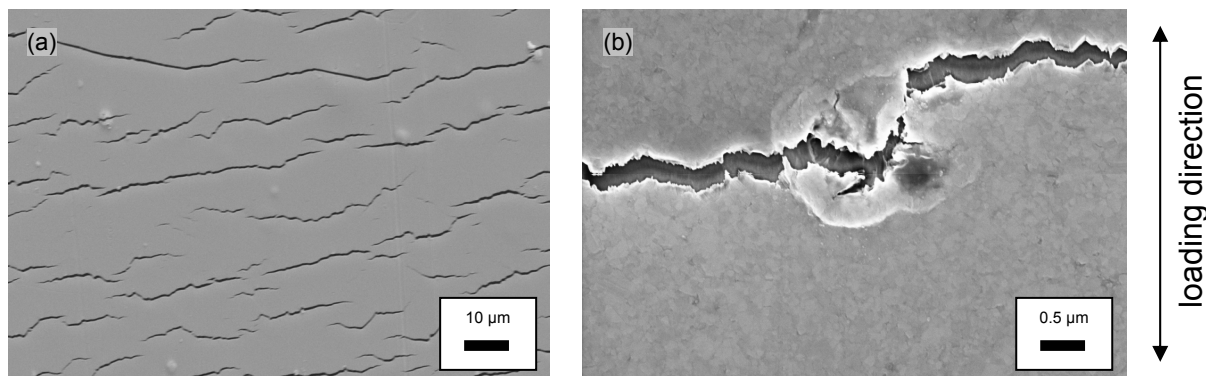


Figure 5.24: Top view of cracks in a 10/100/10 nm thick Ta/Cu/Ta thin film system (SEM image). The cracks go through the intermediate copper layer and the top tantalum layer to the surface.

In Figure 5.25 first results of an 80 nm thin copper film which was directly sputtered on the 125 μm thick polyimide substrate without a tantalum underlayer are shown. The film shows a plateau stress of 540 MPa. No stress drop is visible, which suggests that the formation of crack patterns in the Ta/Cu/Ta and the Ta/Cu films is caused by the 10 nm thin tantalum underlayer.

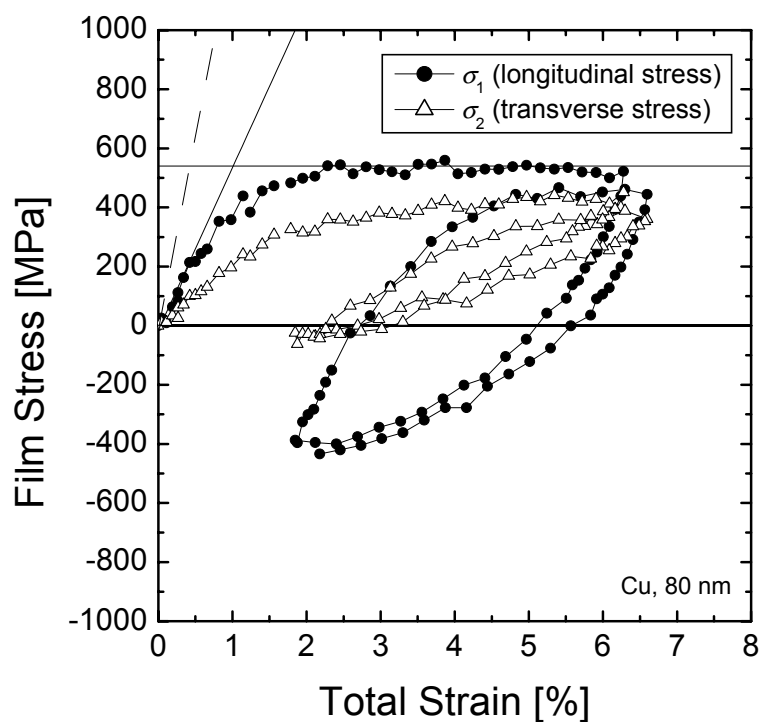


Figure 5.25: Evolution of the longitudinal- and transverse stresses of an 80 nm thin Cu film directly sputtered on a 125 μm thick polyimide substrate. Straight line: linear fit to the first five data points. Dashed line: Slope of the Young's modulus for an Cu single crystal loaded in $\langle 110 \rangle$ direction $E_{110}^{\text{Cu}} = 131$ GPa (calculated according to Equation (2.9) using the elastic constants given in Appendix A).

5.3 Summary of Results

1. The lattice strain measurements performed on Cu/Mo composites at HASYLAB were highly reproducible and comparable to those obtained by Wanner and Dunand (2000) using a different experimental setup at the APS.
2. The Ti-based alloy showed a linear elastic behavior within the whole range of strain. Different slopes were obtained for different Debye-Scherrer rings due to elastic anisotropy. The slopes calculated from the elastic constants agree well with the measured values.
3. Using an enlarged experimental setup, i.e. increasing the specimen-to-detector distance by one order of magnitude increases the strain resolution by one order of magnitude. A much higher signal-to-noise ratio is obtained for minority phases. This was demonstrated by the results obtained for a γ -TiAl alloy.
4. The (001)-oriented grains of γ -TiAl show a different stress-strain behavior at high temperatures compared to room temperature. Deviation from linear elastic behavior occurs at a much lower applied stress.
5. A pressure-induced martensitic phase transformation in NiAl was not found. Only elastic anisotropy was found during the room-temperature compression tests.
6. Using high-energy synchrotron radiation decreases the measuring times for *in situ* strain measurements to about 1 minute per data point. This is a reduction by one order of magnitude compared to neutron diffraction, which takes about several hours per data point.
7. The $\sin^2\phi$ method is capable of measuring stresses in ultrathin films by one single X-ray exposure. The exposure times could be reduced to several seconds per data point using low-energy synchrotron radiation. Strain rates in the order of 10^{-4} could be achieved.
8. *In situ* tensile tests on strongly fiber-textured 20 nm thin Cu and Au films are possible using the $\sin^2\phi$ method. Tunable, brilliant synchrotron X-ray sources are required.
9. The yield stress of Au films was constant within the film thickness range between 80 nm and 1000 nm. Below 80 nm a decrease of the yield stress was observed.
10. A stress decrease was found above a total strain of 2.5% for Cu films with a Ta underlayer. Crack formation was found in these samples. A Ta underlayer is thus not very suitable for tensile tests with large total strains.

6 Discussion

This thesis focuses on the development of a new technique for mechanical tests on bulk samples as well as ultrathin films. Because it also provides new materials insight, the discussion will be divided into two main parts: methodological aspects and materials aspects. First, the $\sin^2\varphi$ technique will be critically discussed stressing its advantages, draw-backs, and potential for further improvement. Second, the micro- or nanomechanics of the investigated materials will be assessed.

6.1 Methodology

The results of the present work show that high-energy synchrotron X-ray diffraction experiments can provide a wealth of information on bulk lattice strains and load partitioning in multiphase alloys. This is also possible if both phases exhibit relatively high atomic numbers and X-ray absorption factors (Mo, Cu, Ti). So far, most studies are based on neutron diffraction experiments and there are only very few studies based on high-energy synchrotron radiation. A comprehensive study was carried out on Cu-Mo composites by Daymond et al. (1999) using a pulsed, polychromatic beam of neutrons produced at a spallation source. If one compares the high-energy X-ray results obtained by Wanner and Dunand (2000) and the results of this work to these neutron diffraction measurements, the data acquisition times were more than one order of magnitude shorter. At the synchrotron X-ray exposure times of several seconds or minutes could be achieved. Neutron diffraction experiments require several hours per data point. The gauge volume required at the synchrotron was about three orders of magnitude smaller. For neutrons, the penetration depth is by about one order of magnitude larger which allows the investigation of much thicker samples. Also the spot size of the incident beam is much larger for neutron experiments leading to a much larger diffracting volume. However, this large gauge volume is a prerequisite for neutron diffraction experiments due to the inherently weak interaction of neutrons with mass. Thus, high-resolution strain mapping experiments, which are in principle possible with synchrotron X-rays (see Spolenak et al. (2002)), are not possible with neutrons. The sample size can also be smaller for the synchrotron experiments. This is beneficial for *in situ* tensile tests, especially if materials with high strength are investigated. The cross-sectional area can then be reduced, which allows much higher applied stresses on the sample with a relatively

compact tensile machine. The small diffracting volume limits the application of the synchrotron method to relatively fine grained materials, but it has been shown in this work that this limitation can be overcome by enlarging the experimental setup.

The results obtained for γ -TiAl (see chapter 5.1.3) have demonstrated that the enlarged experimental setup realized at beamline PETRA 2 of HASYLAB offers a wide potential for micromechanical studies on polycrystalline materials. The disadvantages from not being able to record full Debye-Scherrer diffraction rings are more than compensated by the much better resolution of the partial patterns recorded at a greater distance from the specimen. The influence of specimen-to-detector distance on strain resolution is shown in Figure 6.1. The strain resolution $\Delta\varepsilon$ is directly proportional to the sample movements Δx and inversely proportional to the detector distance L . A better strain resolution can thus be achieved by either using a calibration substance or by increasing the detector distance. A substantially increased specimen-to-camera distance therefore also diminishes the effects of unintentional specimen movements on the lattice strain results, which is the reason why measurements can be made without a calibration substance if necessary. This facilitates *in situ* experiments significantly, especially if elevated testing temperatures are involved.

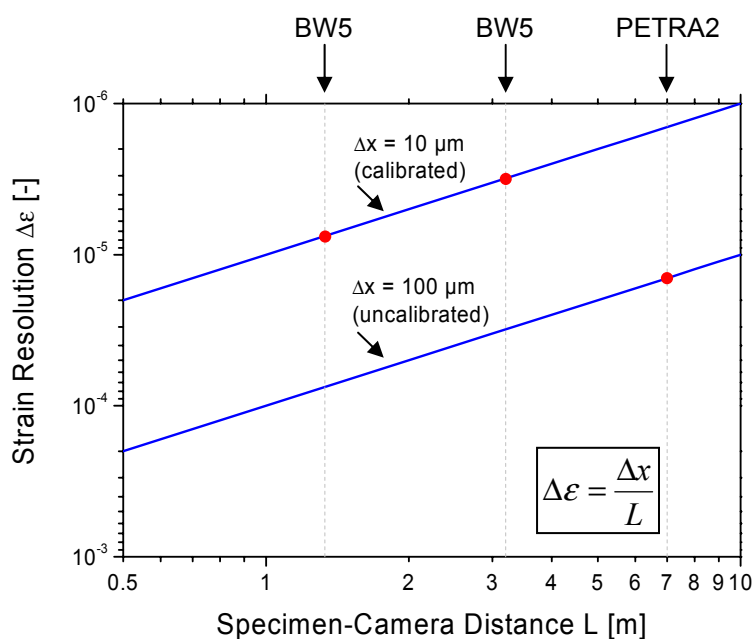


Figure 6.1: Influence of specimen-to-camera distance and use of a calibration substance on the strain resolution.

It has been shown in chapter 4.3 that the $\sin^2\varphi$ method can be successfully applied to *in situ* tensile tests on thin film materials using the theoretical concepts which have been introduced in chapter 3.2. The results of the present studies on Au and Cu films show that the described low-energy synchrotron method is a viable technique for measuring stresses in ultrathin crystalline films at data collection times feasible for fast *in situ* X-ray tensile tests. The signal-to-noise ratio was very good even in the case of the thinnest Cu films investigated, which suggests that the method can be applied to even thinner films.

The major advantages compared to established techniques are that no relative motion of sample, X-ray source and detector is required for the $\sin^2\varphi$ measurements, and that intense, low-index reflections can be used without sacrifice concerning strain resolution. The experimental setup is simple (apart from the fact that an appropriate synchrotron X-ray source and a high-resolution area detector are needed) and requires no elaborate alignment. Longitudinal and transverse strains can be determined simultaneously with the same precision, making it possible for the first time to characterize *in situ* the evolution of the plane stress state with high accuracy. It has been shown in chapter 5.2 that the stress state in the stressed film is far from being uniaxial, which underlines that it is essential to determine the complete stress state in order to derive accurate materials parameters. In this sense, this newly developed technique offers a huge improvement for thin film studies in general, including thicker films in the micron thickness range. During the tensile test, only measurements *relative* to the initial stress state are required thus making the $\sin^2\varphi$ method the ideal method of choice.

The results of the present work obtained for thin copper and gold films show that data collection times of the order of 10 s per data point are possible for films thinner than 100 nm, which allows the evolution of stress in such thin films to be monitored at strain rates of up to 10^{-4} s^{-1} . High-index lattice planes (high scatter angles) are used in order to increase the strain resolution. However, such planes exhibit low scattered intensities making them inappropriate for studies on ultrathin films (film thicknesses range below 100 nm). It is remarkable that a strain resolution better than 10^{-4} can be achieved using $\{111\}$ planes. The key issue in achieving such a high strain resolution is the superior statistics of the $\sin^2\varphi$ method. The

number of data points extracted from one CCD frame is at least two orders of magnitude higher compared to the conventional $\sin^2\psi$ method (see Figure 5.15a and b for comparison).

In Figure 6.2 the experimental results of the synchrotron measurements are compared to $\sin^2\psi$ -measurements at the laboratory source as they were also carried out by Hommel and Kraft (2001). Within the source of error, no significant differences can be observed between the two *in situ* tensile tests performed at two different strain rates for a 1.5 μm thick Cu film. However, the method is capable of performing *in situ* X-ray studies of the time dependent behavior of thin films, even in the film thickness range below 100 nm.

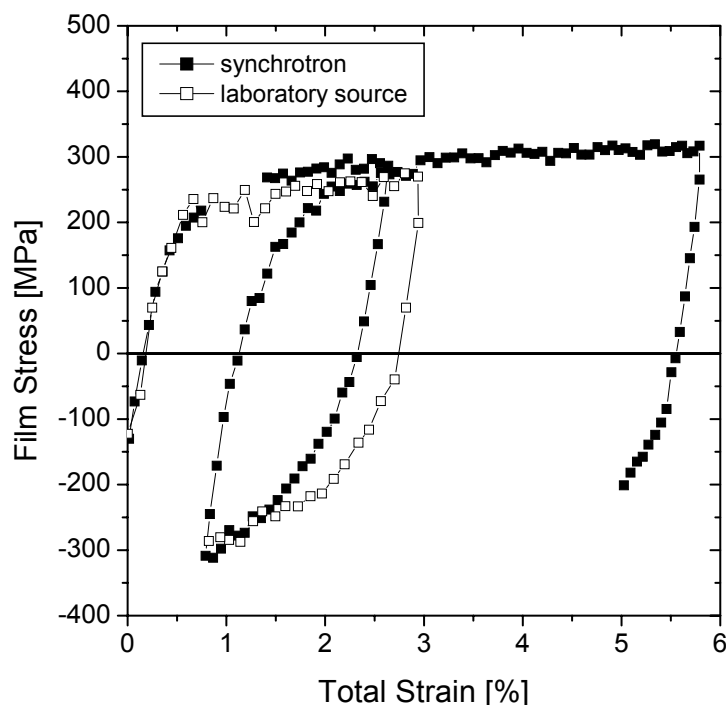


Figure 6.2: Comparison of two different *in situ* tensile tests performed on 1.5 μm thin Cu films with different strain rates. The tensile test at the laboratory source (D5000 from Siemens AG, Germany) was performed with a total exposure time of about 1 h per data point, the synchrotron measurements were performed with an exposure time of only 15 s per data point. The strain rate of the synchrotron measurements is thus about two orders of magnitude higher than the measurements at the laboratory source ($5 \cdot 10^{-5} \text{ s}^{-1}$ compared to $3 \cdot 10^{-7} \text{ s}^{-1}$). The synchrotron measurements were continued to higher strains.

Unintentional sample movements during the tensile test would lead to significant measurement errors if unaccounted for. This reveals the necessity for applying a calibration substance to the sample. Tungsten powder embedded in vacuum grease turned out to be a very suitable calibration substance. However, its application as grease makes thickness

control difficult, which needs to be further improved for the initial $\sin^2\psi$ measurements determining the as-deposited residual stress state. The effective distance between the scattering centers of the film and the calibration substance (mainly determined by the substrate thickness) strongly affects the $\sin^2\psi$ results. Precise control of the thickness of the calibration substance would therefore be desirable. As a first step a defined thickness of the calibration substance could be achieved by using a mask for its application.

Using a dedicated, tunable and brilliant synchrotron source is a prerequisite for X-ray stress measurements on ultrathin and strongly fiber textured films on polyimide substrates. The high flux provided by such a source is needed to produce sufficient diffracted intensities, and its wavelength tuneability is required to fulfill the Bragg condition for the texture component used. The $\sin^2\phi$ method can thus not be applied straightforwardly at high energies for thin textured films. As the present results show, an optimum configuration for $\langle 111 \rangle$ fiber textured fcc films can be defined. It should be noted, however, that this will be more difficult for films exhibiting different textures or less symmetric crystal structures and it may not always be possible to find low-index reflections that fulfill the texture requirements and can be accessed within the available wavelength range of the synchrotron source.

The sharpness of the texture turned out to be crucial for measurements at the end of the thickness range where $\sin^2\phi$ X-ray strain measurements are possible. Even with the high flux of a synchrotron, the success of the measurements depends on the texture sharpness of the film. This can be seen on the results obtained for ultrathin copper films: while it was possible to obtain good results for a 20 nm thin copper film with a tantalum underlayer supporting the $\langle 111 \rangle$ fiber texture, strain evaluation was not possible for a 20 nm thin copper film which was directly sputtered on the polyimide substrate due to the very low signal-to-noise ratio. For comparison, in Figure 6.3a the peak intensity profiles for 10/20/10 nm Ta/Cu/Ta films are shown. Since the tantalum underlayer increases the $\langle 111 \rangle$ fiber texture of the Cu film, the resulting sharp texture yields a weak but evaluable Cu peak. In Figure 6.3b the peak intensity profile for a 30 nm thin Cu film is shown, which was directly sputtered on the polyimide substrate. Although the Cu film in (b) is 10 nm thicker than that in (a), the Cu peak is too weak for evaluation, i.e. the signal-to-noise ratio is too low for appropriate peak fitting. The reason for this is the broader $\langle 111 \rangle$ fiber texture which leads to less scattered intensity for the

Cu film. Thus, it was only possible to obtain reasonable stress-strain results for an 80 nm thin Cu film, which was directly sputtered on polyimide (see Figure 5.25).

The texture measurements performed on the gold films have been shown in Figure 4.8, and the result for strain evaluation is in principle the same as for copper: in case of the Au films a titanium underlayer enhances the $\langle 111 \rangle$ fiber texture and thus leads to more diffracted intensity along the (111) Debye-Scherrer rings. However, due to the higher atomic mass of gold compared to copper, the (111) diffraction ring of gold exhibits much more intensity which will make possible strain evaluation in even thinner than 20 nm Au films without a titanium underlayer.

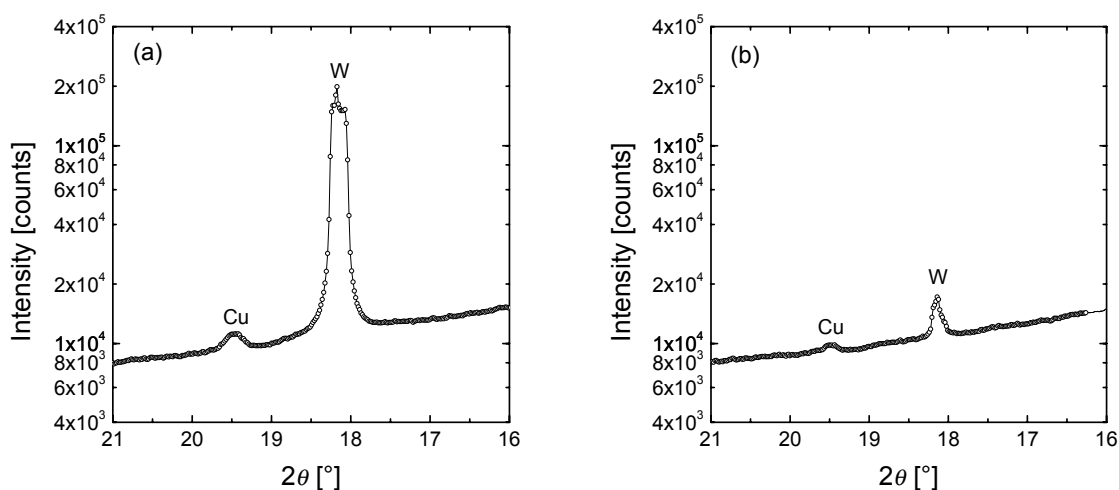


Figure 6.3: (a) Peak intensity profile for 10/20/10 nm Ta/Cu/Ta films on 125 μm polyimide substrate. (b) Peak intensity profile for 30 nm Cu film without Ta layers on 125 μm polyimide substrate.

6.2 Material Aspects

6.2.1 Ti-Based Material

The studies on the Ti-based material were primarily performed in order to observe the elastic anisotropy of the material. Since the volume content of the TiB whiskers and TiC particles is much too low (see also Figure 4.5a) no influence of the reinforcements on the mechanical behavior of the titanium matrix material was expected. The material serves thus as a sample material to check the functionality of the $\sin^2\phi$ method. Due to the elastic anisotropy of titanium, the following hkl -dependent Young's moduli E_{hkl} can be calculated from the elastic constants of titanium using Equation (2.10) (see also Figure 2.1): $E_{101} = E_{102} = 92$ GPa,

$E_{103} = 102$ GPa, $E_{100} = E_{110} = 104$ GPa, $E_{002} = 146$ GPa. As can be seen in Figure 5.3, a linear elastic behavior is obtained for all observed hkl -dependent lattice strains, and the calculated slopes fit well to the measured results. The applied force vs. total strain curve of the material was accessible only from the crosshead displacement of the tensile tester and is therefore just a rough estimate. However, the absence of plasticity agrees well with the results obtained by Lu et al. (2001) for the same material. They measured linear-elastic behavior during a uniaxial tensile test. At 0.75% total strain these authors report an applied stress of about 1 GPa which yields a Young's modulus of about 130 GPa for this material. Due to the hexagonal lattice of titanium the Young's modulus cannot be calculated after Voigt and Reuss according to Equations (2.11) and (2.12) since these Equations are only valid for cubic polycrystals. More advanced models are required for this task, e.g. the model reported by Evenschor et al. (1971). These polycrystal calculations are not the intention of this thesis and are not further discussed in detail. From the methodological point of view, the $\sin^2\varphi$ method is capable of monitoring the elastic anisotropy within the bulk of a titanium-based material with sufficient strain resolution *in situ* during an uniaxial tensile test. This is the basis for measuring deviations from linearity, i.e. monitoring the load partitioning between different phases in a material.

6.2.2 γ -TiAl

The applied stress vs. lattice strain results presented in Figure 5.7 on page 69 show that the data obtained in the two different experiments (conventional and enlarged setup) agree very well, especially in the longitudinal direction. Stresses were calculated from lattice strains with Hooke's Law according to Equation (2.4). The Voigt Model was used for the polycrystal assuming iso strains, see chapter 2.1.3. In the following, stresses for one individual phase (e.g. the γ -TiAl phase) obtained in this way will be called *phase stresses*. In Figure 6.4 the phase stress of the γ -TiAl phase calculated from the strains of (222) lattice planes is shown. At stresses below 450 MPa (i.e. in the linear-elastic regime according to Figure 5.4 on page 66), the data points follow a straight line. The apparent Young's modulus calculated from the slope of this line is 208 GPa, which is close to the Young's modulus $E_{111} = 216$ GPa reported by He et al. (1995) for a γ -TiAl single crystal (see Table 6). This indicates that within the linear-elastic regime no pronounced load-partitioning exists between the γ -TiAl phase and the other constituents of the alloy.

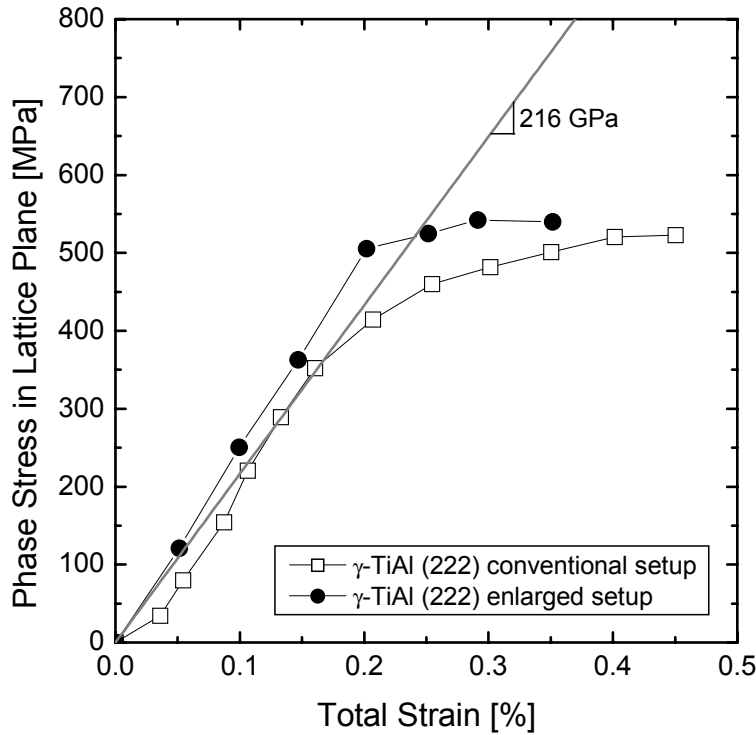


Figure 6.4: Phase stress of the γ -TiAl (222) lattice planes calculated from the elastic lattice strains shown in Figure 5.7b measured in the plane normal to the incident beam containing the longitudinal direction (tensile stress). The stresses were calculated with Hooke's Law (see Equation (2.4)) according to the Voigt Model (iso strains, see chapter 2.1.3) using the elastic constants given in Table 6 (for tetragonal stiffness matrix see Appendix B).

Table 6: Single crystal elastic constants of tetragonal γ -TiAl (composition 46at.%Al) according to He et al. (1995) and Tanaka et al. (2003).

C_{11} [GPa]	C_{12} [GPa]	C_{13} [GPa]	C_{33} [GPa]	C_{44} [GPa]	C_{66} [GPa]	T [°C]
205	77	50	232	61	64	25
187	77	52	210	52	55	700
180	77	52	208	50	52	800

An apparent Poisson's ratio ν can be obtained by normalizing the slope of the straight line describing the experimental transverse strains to the slope of the line describing the longitudinal strains in Figure 5.7. Linear fits yield $\nu = 0.23$ for both experiments performed at room temperature. In order to compare this apparent Poisson's ratio to elastic constants reported in the literature, the normal elastic strains existing in the $\langle 111 \rangle$ direction of an *isolated*, unconstrained γ -TiAl single-crystal subjected to uniaxial stress in either the $\langle 111 \rangle$

direction, the $\langle 1\bar{1}0 \rangle$ direction, or the $\langle 11\bar{2} \rangle$ direction have been calculated. These three directions are nearly orthogonal since the c/a lattice constant ratio of γ -TiAl is close to unity.

For this particular stress state, the following stress tensor expressed in terms of the compliances S_{ij} is obtained by coordinate transformation:

$$\sigma'_{ij} = \begin{pmatrix} \frac{1}{3}(S_{11} + S_{12} + S_{23}) & \frac{1}{6}S_{66} & \frac{1}{6}S_{44} \\ \frac{1}{6}S_{66} & \frac{1}{3}(S_{11} + S_{12} + S_{23}) & \frac{1}{6}S_{44} \\ \frac{1}{6}S_{44} & \frac{1}{6}S_{44} & \frac{1}{3}(2S_{13} + S_{33}) \end{pmatrix}. \quad (6.1a)$$

The required strain tensor can easily be obtained by inverting the stress tensor of Equation (6.1a). This operation was done numerically using any common spreadsheet software like Microsoft Excel or analytically using a computer algebra software package like Maple V. Using the single-crystal elastic constants given in Table 6, the computations yield the following results: $\epsilon_{111}^{111} = 0.46 \times 10^{-11}$, $\epsilon_{111}^{1\bar{1}0} = 0.12 \times 10^{-11}$, and $\epsilon_{111}^{11\bar{2}} = 0.05 \times 10^{-11}$. This means that two possible maximum and minimum Poisson's ratios exist which can be defined based on these elastic strains: $\nu_{111}^{1\bar{1}0} = -\epsilon_{111}^{1\bar{1}0} / \epsilon_{111}^{111} = 0.26$, and $\nu_{111}^{11\bar{2}} = -\epsilon_{111}^{11\bar{2}} / \epsilon_{111}^{111} = 0.10$. These calculations show that a wide distribution of Poisson's ratios is expected for the individual grains in a γ -TiAl polycrystal. The experimentally measured apparent Poisson's ratio ($\nu = 0.23$, see above) is an effective value of a large number of grains.

The deviation from linearity observed at higher stresses in the applied stress vs. lattice strain plot (see Figure 5.7) indicates that load transfer from the 111 γ -TiAl grains to other constituents takes place in the plastic regime. The deviation between the two transverse strain curves observed at high applied stresses is not clear. For a more detailed analysis of this process it would be required to measure the lattice strains in γ -TiAl-grains with lattice planes other than (222) and in other phases of the alloy, especially within the α_2 -Ti₃Al minority phase.

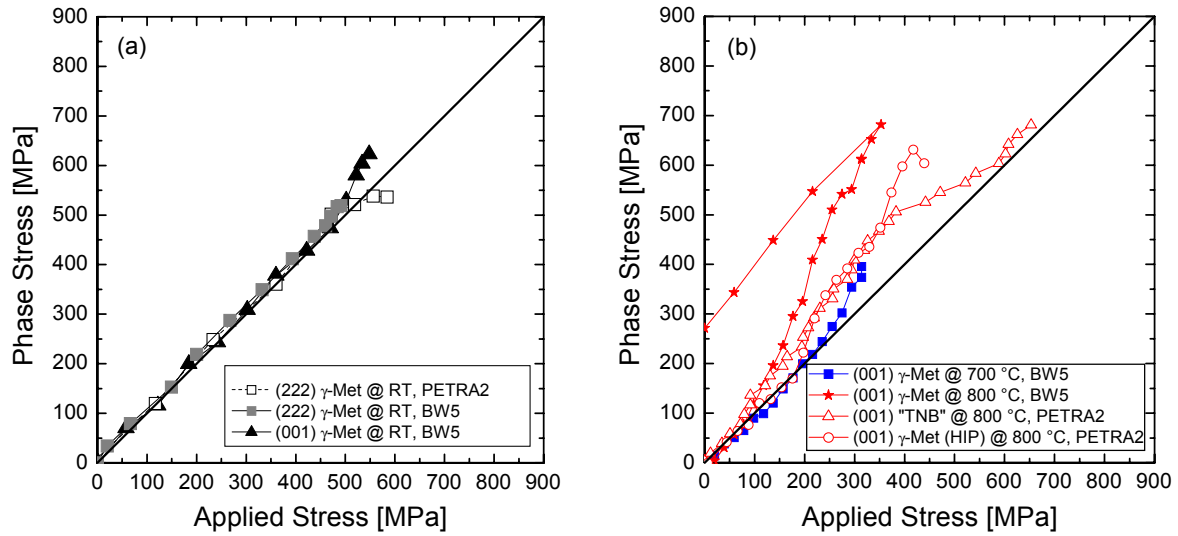


Figure 6.5: Estimated phase stresses calculated by Hooke's Law (see Equation (2.4)) according to the Voigt Model (iso strains, see chapter 2.1.3) using the elastic constants given in Table 6 (for tetragonal stiffness matrix see Appendix B). (a) Room-temperature phase stresses of the γ -TiAl phase acting on different crystallographic lattice planes plotted against the applied stress as measured by the load cell of the in situ tensile tester. (b) Same plot as in (a) for the high-temperature experiments.

In Figure 6.5a the phase stresses of the γ -TiAl phase which act on the (222) and the (001) lattice planes are plotted against the applied stresses. As long as no load transfer occurs, the data points follow a straight line with a slope of 1. It can be seen that load transfer occurs at room temperature only near fracture at stress levels higher than 550 MPa. While the stress increases normal to the (001) lattice planes, the stress decreases normal to the (222) lattice planes which means that before fracture, a stress increase along the $\langle 001 \rangle$ direction can be observed. This behavior can also be seen for the high-temperature experiments (Figure 6.5b): in direction normal to the (001) lattice planes the stress increases before fracture, but the deviation from linearity starts at much lower applied stress levels.

Plastic deformation of γ -TiAl may be best described by the lack of sufficient ductility at room temperature as well as at intermediate temperatures, and yielding at high temperatures. This deformation behavior is mainly attributed to the presence of two independent slip systems both of which operate simultaneously over the entire temperature range in the polycrystal. According to Mecking et al. (1997), there are 4 possible ordinary slip systems of the type $\{111\} \frac{1}{2} \langle 110 \rangle$, 8 superdislocation slip systems of the type $\{111\} \langle 101 \rangle$ and 4 unidirectional twinning systems of the type $\{111\} \langle 11\bar{2} \rangle$. Based on the assumption of classical crystal and

polycrystal plasticity models, single crystal level dislocation glide and twinning are assumed to be the only available mechanisms of plastic deformation in γ -TiAl. The results shown in Figure 5.7b and Figure 5.8 demonstrate that the lattice strains obtained for the (001) lattice planes of the γ -TiAl polycrystal show a negative deviation from linear elasticity which is very pronounced at high temperatures. The evolution of stresses shown in Figure 6.5a and b was calculated based on the simple Voigt Model and can therefore be considered only as a rough estimate. In this case, the calculations yield a strong increase for the stress acting perpendicular to the (001) lattice planes. Calculating the Schmid Factor for ordinary slip and superdislocation slip in $\langle 001 \rangle$ direction yields a Schmid Factor 0 for ordinary slip and 0.41 for superdislocation slip. For γ -TiAl the $\langle 001 \rangle$ orientation is thus a pronounced hard orientation. This is the reason why a stress increase can be seen in Figure 6.5a and b for the $\langle 001 \rangle$ orientation in the plastic range of deformation. In order to describe polycrystal deformation the critical resolved shear stress should be calculated based on more advanced models like the self-consistent Hutchinson model (Hutchinson (1970), see also chapter 2.1.3] taking also the texture of the material into account. For applying this model, some more grain orientations would be necessary which are not available so far. The evolution of texture could in principle also be obtained *in situ* during the tensile test if the sample would be rotated around the tensile axis. The experimental realization of this would be the next step in order to obtain texture and strain information simultaneously during the tensile test. The fast data acquisition time of the high-energy $\sin^2\varphi$ method would also be advantageous for this task.

6.2.3 NiAl

The different slopes observed for the $\langle 100 \rangle$ and the $\langle 110 \rangle$ orientation of NiAl appear to be primarily the result of elastic anisotropy. No signs of plasticity can be observed in Figure 5.12b. If plastic anisotropy is present, usually a change in slope is observed at the transition from the elastic to the elastic-plastic regime as reported by Clausen et al. (1999). According to the applied stress vs. total strain curve shown in Figure 5.12a, this transition takes place at about 200 MPa. The absence of pronounced nonlinearities in Figure 5.12b is surprising, given that NiAl single crystals are known to exhibit pronounced plastic anisotropy (Miracle (1993)). Since no calibration substance could be attached due to limited space around the small samples, measurement errors were larger than usual due to uncompensated

specimen movements. Bulging of the sample in the plastic regime could occur during the compression test, which then would lead to distorted stress-strain curves.

The occurrence of a pressure-induced martensitic phase transformation could not be found. There could be three reasons for the absence of additional diffraction rings during compression: (1) there is indeed no martensitic phase transformation (2) the volume content of the martensitic phase is too low and cannot be detected by the image plate detector due to an unfavorable signal-to-noise ratio (3) the pressure was too low. It is assumed that the diffraction ring smoothening is caused by a combination of the following two effects: (1) subgrain formation, resulting in a better grain statistics, and (2) Bragg peak broadening due to an increase in dislocation density. Note that the diffraction rings become smoother but not broader (see Figure 5.12a), which shows that the Bragg peak broadening is much smaller than the width of the diffraction ring defined by the diameter of the incident beam and the specimen thickness.

6.2.4 Plasticity of Thin Cu and Au Films

The mechanical properties of thin films differ considerably from the bulk values (Freund (1987), Nix (1989), Thompson (1990), Arzt (1998)). Their flow stresses are much higher compared to that of the bulk, and often an inverse proportionality of flow stress and film thickness is observed, i.e. the flow stress increases with decreasing film thickness (Nix (1989)). Up to now, the origin of the internal stresses acting in the film is not fully understood. Microstructural effects correspond to the film itself, i.e. the microstructure and its influence on dislocation motion. External effects correspond to interactions between film and substrate. Often both effects influence each other and are not strictly distinguishable. However, the essential experimental observation reported so far is that the stresses in thin films are higher, the thinner the film thickness (Keller et al. (1998), Hommel and Kraft (2001)). Additional films, i.e. passivation layers can further increase the stresses in the film (Nix (1998)).

The results obtained for the gold films as presented in Figure 5.18a-f show a plateau stress value of about 600 MPa for all films thicker than 80 nm. This thickness independence reveals that there are no size effects in the plastic flow behavior due to dimensional constraints

regarding the film thickness in the tested gold films. Although this observation is first of all against the common trend, it can be explained by the history of the gold films: unlike the copper films, the gold films have not been annealed after deposition, i.e. no grain growth occurred leading to a very fine-grained microstructure. Thus, it is very likely that not the film thickness but the grain size defines the size limit of the plastic behavior of the gold films investigated. Since all films should exhibit the same grain size, a plateau stress is thus understandable, if the size limit is given by the grain size. However, the decrease of the plateau stress for the 40 and 20 nm thin gold films is unexpected and so far not understood as it cannot be explained by this assumption. This behavior is against the common trend that the yield stress of thin films either increases for thinner films or stays at a constant plateau value. Although the signal obtained from the 20 nm thin gold films is very weak, the strain evaluation was highly reproducible. This has been shown in Figure 5.17 for two different 20 nm thin gold films which both show almost the same plateau stress values of about 300 MPa. This work focuses on methodological developments and the questions of film thickness dependent behavior will be discussed in much more detail in the ongoing Ph.D. thesis of Patric Gruber (Universität Stuttgart).

The stress evolution results obtained by the present work for all thin copper and gold films on polyimide substrates show that the stress states in the films evolving during uniaxial tensile testing are neither uniaxial nor equibiaxial. The measured values of σ_1 and σ_2 depend on the residual stresses introduced during fabrication as well as on the elastic and plastic properties of both the film and the substrate. One interesting point observed in the case of the gold as well as the copper films is the evolution of a *tensile* stress within the film in transverse direction. This implies that the Poisson's ratio of the film must be larger compared to that of the substrate. Indeed, the elastic in-plane Poisson's ratio of $\langle 111 \rangle$ textured Au is $-S_{12}/S_{11}=0.57$ and of $\langle 111 \rangle$ textured Cu $-S_{12}/S_{11}=0.50$ (for compliance constants see Appendix A). According to the supplier, the Poisson's ratio of the polyimide foil is only 0.34 (see DuPont (1996)). These considerations underline the importance of characterizing the complete stress tensor (σ_1 and σ_2).

In order to compare the stress-strain results to yield stresses in the literature obtained from "real" uniaxial tensile tests on free standing films or from wafer-curvature measurements, a

stress invariant like the von Mises stress should be considered. This is shown in Figure 6.6a and b. In that diagram the von Mises stress is plotted against the total strain for a 40 nm thick Au film on a polyimide substrate and compared to the principal stress σ_I . This quantity is reported in most of the published studies (e.g. Kuschke and Arzt (1994), Kretschmann et al. (1997), Kang et al. (1997), Tregilgas and Strumpell (1998), Kraft et al. (2000), Hommel and Kraft (2001)).

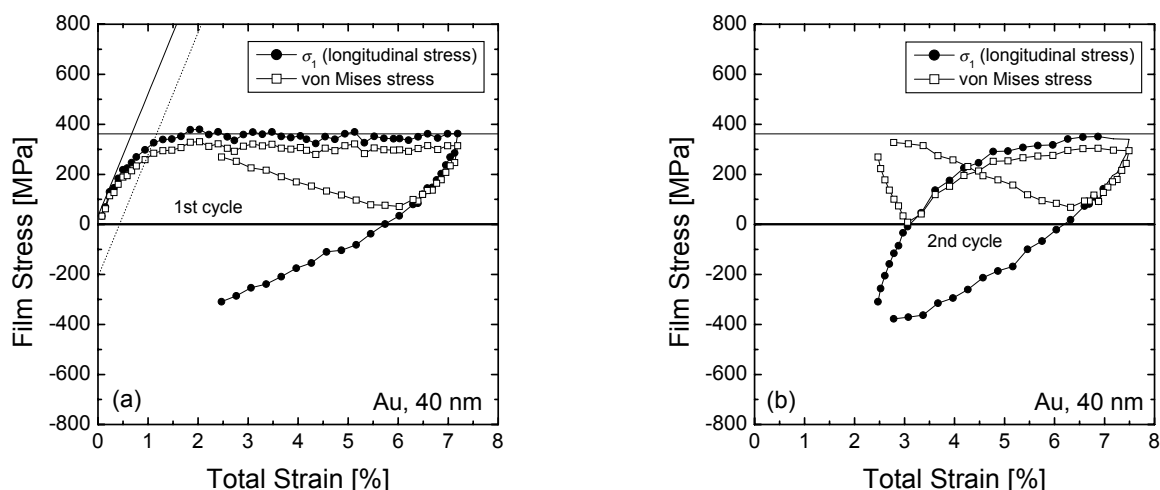


Figure 6.6: Von Mises stress for a 40 nm Au film compared to the longitudinal stress σ_I . (a) first loading-unloading cycle. (b) Second loading-unloading cycle.

At large strains, σ_I is up to about 15% higher than the von Mises stress, leading to corresponding overestimation of the yield stress if the biaxiality of the stress state is neglected. At low strains, this discrepancy is even more pronounced. Since no linearity can be seen in the von Mises stress the definition of a yield stress is not trivial. Thus the following procedure is suggested: First a straight line is fitted to the elastic regime of σ_I (see Figure 6.6a). This line is then shifted by a strain of 0.5% (corresponding to a $\sigma_{0.5}$ yield criterion). In the end, the intersection of this shifted line with the von Mises curve determines the flow stress σ_y , which is in this case of the 40 nm thick Au film about 290 MPa. This value compares very well with the results by Leung et al. (2000) obtained by wafer-curvature measurements on Au films. The choice of 0.5% in strain is rather arbitrary but coincides with other published criteria (see Hommel and Kraft (2001)) and agrees well with the amount of plastic strain observed in most substrate-curvature experiments.

7 Conclusions

1. In this work it was shown that the $\sin^2\phi$ method can be used for a wide spectrum of materials science-related questions. Methodological improvements could be achieved due to the following recently available developments: (1) large, high-resolution area detectors, (2) storage and computing capacity for data evaluation, (3) experimental endstations dedicated for synchrotron X-ray experiments.
2. For the first time, it could be shown experimentally how the limitation of the high-energy X-ray technique to very fine-grained materials can be overcome by enlarging the experimental setup by one order of magnitude, including the diameter of the incident beam.
3. It was possible to reduce the sensitivity to unintentional specimen displacements along the beam axis, which have to be eliminated by using a calibration substance attached to the sample such that it is not strained during the tensile test. No further calibration substance was required using the enlarged experimental setup.
4. The absence of a calibration substance facilitates *in situ* tensile tests at high temperatures since applying a high-temperature resistant calibration substance would be very crucial and very impractical. First high-energy X-ray strain measurements during high-temperature *in situ* tensile tests have been successfully performed on a TiAl-based material.
5. The lattice strain measurements on Cu/Mo at HASYLAB were very reproducible and comparable to those obtained by Wanner and Dunand (2000) obtained by a different experimental setup at the Advanced Photon Source (APS).
6. The titanium-based material showed a linear-elastic behavior within the whole strain range. Because of elastic anisotropy different slopes were obtained in the stress-strain plot for different Debye-Scherrer rings. The calculated elastic constants agree with the measured values.
7. (001)-oriented γ -TiAl grains show a different stress-strain behavior at room temperature and at high temperatures. At high temperatures a deviation from linear elastic behavior occurs at much lower applied stresses compared to room temperature.
8. A pressure-induced phase transformation could not be found for NiAl. No signs of plasticity could be found at room temperature.

9. The $\sin^2\phi$ method was successfully adapted to thin film applications using tunable, high-flux, low-energy synchrotron X-rays. This was demonstrated by measuring the evolution of biaxial stresses during *in situ* tensile tests for ultrathin copper and gold films down to a film thickness of 20 nm.
10. Due to the normal-incidence geometry, the complete evolution of the biaxial stress state in thin films can be monitored by only one measurement using a high-resolution CCD area detector. This increases the possible strain rate at least by a factor of 6 compared to the established $\sin^2\psi$ method. Both, longitudinal and transverse stresses are measured with the same accuracy.
11. The flow stress of thin gold films was constants in the film thickness range between 80 nm and 1000 nm. Below 80 nm a decreaseing flow stress was observed.
12. Thin copper films with tantalum underlayer showed a stress decrease above 2.5% total strain. Crack formation was observed of these films. A tantalum underlayer is not suitable for measurements at large total strains.

8 Outlook

Figure 8.1 shows a schematic of the new HARWI II beamline which will be built and operated by GKSS and HASYLAB by the end of 2004. The fundamental issues of using an enlarged setup entered the design of this new beamline which will provide a large specimen-to-detector distance as well as two movable area detectors.

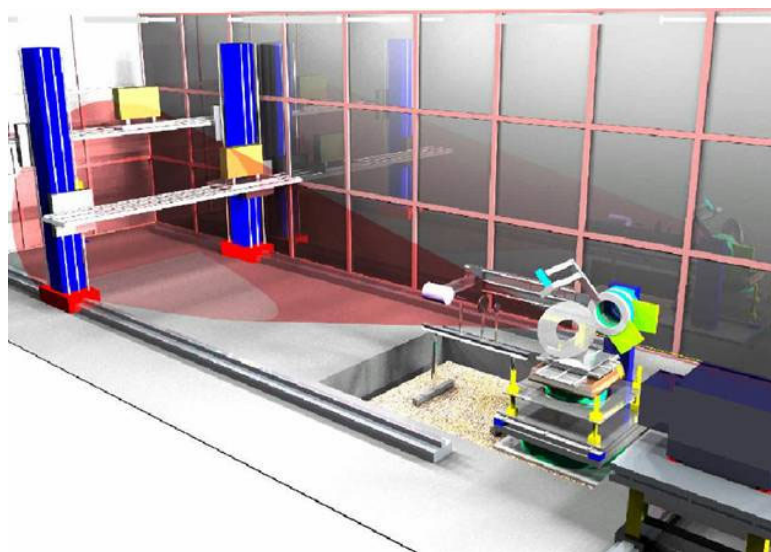


Figure 8.1: 3D-CAD drawing of the HARWI 2 beamline which will become available in the fall of 2004 (image courtesy of GKSS).

9 References

Advanced Photon Source (2003). www.aps.anl.gov

ANKA (2003). www.fzk.de/anka

Arzt, E. (1998), Size effects in materials due to microstructural and dimensional constraints: a comparative review, *Acta mater.*, **46** No.16, 5611-26.

Arzt, E., Grahle, P. (1996), Dispersion Strengthening of Disordered and Ordered Metallic Materials: From Dislocation Mechanisms to New Alloys, *Z. Metallkd.* **87**, 874-884.

Bartels, A., Schillinger, W. (2001), Micromechanical mechanism of texture formation in γ -TiAl, *Intermetallics* **9**, 883-889.

Bartels, A., Hartig, C., Willems, S., Uhlenhut, H. (1997), Influence of the Deformation Conditions on the Texture Evolution in Gamma-TiAl, *Mater. Sci. Eng. A* **239/240**, 14-22.

Besser, P.R., Brennan, B., Bravman, J.C. (1994), An x-ray method for direct determination of the strain state and strain relaxation in micron-scale passivated metallization lines during thermal cycling, *J. Mater. Res.*, **9** No.1, 13.

Biermann, H., Grossmann, B.V., Mechsner, S., Mughrabi, H., Ungar, T., Snigirev, A., Snigireva, I., Souvorov, A., Kocsis, M., Raven, C. (1997), Microbeam synchrotron radiation diffraction study of a monocrystalline nickel-base turbine blade after service, *Scripta Materialia*, **37**, 1309-1314.

Böhm, J., Wanner, A., Kampmann, R., Franz, H., Liss, K.-D., Schreyer, A., Clemens, H. (2003), Internal stress measurements by high-energy synchrotron X-ray diffraction at increased specimen-detector distance, *Nuc. Inst. and Meth. Phys. Res. B*, **200**, 315-322.

Böhm, J., Gruber, P., Spolenak, R., Stierle, A., Wanner, A., Arzt, E. (2004), Tensile Testing of Ultrathin Polycrystalline Films: A New Synchrotron-Based Technique, *Rev. Sci. Instr.*, **75** No.4, 1110-1119.

Clausen, B. (1997), Characterisation of Polycrystal Deformation by Numerical Modelling and Neutron Diffraction Measurements, Ph.D. thesis, Risø-R-985(EN), Risø National Laboratory and Technical University of Denmark.

Clausen, B., Lorentzen, T., Bourke, M.A.M., Daymond, M.R. (1999), Lattice strain evolution during uniaxial tensile loading of stainless steel, *Mater. Sci. Eng. A* **259**, 17-24.

Clemens, H., Kestler, H., Eberhardt, N., Knabl, W. (1999), Processing of γ -TiAl-Based Alloys on an Industrial Scale, *Gamma Titanium Aluminides*, Eds. Y.-W. Kim, D. M. Dimiduk and M.H. Loretto, TMS, Warrendale, PA, USA, 209-223.

- Daymond, M.R., Withers, P.J. (1996), A synchrotron radiation study of transient internal strain changes during the early stages of thermal cycling in an Al/SiC_w MMC, *Scripta Materialia*, **35**, 1229-1234.
- Daymond, M.R., Lund, C., Bourke, M.A.M., Dunand, D.C. (1999), Elastic phase-strain distribution in a particulate-reinforced metal-matrix composite deforming by slip or creep, *Metallurgical & Materials Transactions A-Physical Metallurgy & Materials Science*, **30A** No.11, pp.2989-97.
- Dölle, H. (1979), The influence of multiaxial stress states, stress gradients and elastic anisotropy on the evaluation of (Residual) stresses by X-rays, *J. Appl. Crystallogr.*, **12**, 489-501.
- DuPont (1996), Materials data sheet for Kapton[®], type HN, 5.
- European Synchrotron Radiation Facility (2003). <http://www.esrf.fr>
- Evenschor, P.D., Fröhlich, W., Hauk, V. (1971), Berechnung der röntgenographischen Elastizitätskonstanten aus den Einkristallkoeffizienten hexagonal kristallisierender Metalle, *Z. für Metallkunde*, **62**, 38-42.
- Ewald, P.P. (1920), *Zeitschrift für Physik*, **2**, 332.
- Feiereisen, J.P., Ferry, O., Jacques, A., George, A. (2003), Mechanical testing device for in situ experiments on reversibility of dislocation motion in silicon, *Nuc. Inst. and Meth. Phys. Res. B*, **200**, 339-345
- Flinn, P.A., Chiang, C. (1990), X-ray diffraction determination of the effect of various passivations on stress in metal films and patterned lines, *J. Appl. Phys.*, **67**, 2927-31
- Freund, L. B. (1987), The stability of a dislocation threading a strained layer on a substrate, *J. of Appl. Mech.*, **54** No.3, 553-557.
- Gehlen, C. (2003), www.physik.rwth-aachen.de/~hebbeker/lectures/sem0102/gehlen2.pdf
- Gelinck, G.H., Huitema, H.E., van Veenendaal, E., Cantatore, E., Schrijnemakers, L., van der Putten, J.B.P.H., Geuns, T.C.T., Beenhakkers, M., Giesbers, J.B., Huisman, B.-H., Meijer, E.J., Benito, E.M., Touwslager, F.J., Marsman, A.W., van Rens, B.J.E., de Leeuw, D.M. (2004), Flexible active-matrix displays and shift registers based on solution-processed organic transistors, *nature materials*, advance online publication (25.01.2004), www.nature.com/naturematerials, doi:10.1038/nmat1061.
- Glocker, R., Gisen, F., Osswald, E. (1936), *Z. Tech. Physik*, **17**, 145.
- Goens, E., Weerts, J. (1936), Principal elastic constants of single crystals of copper, gold and lead, *Physik. Z.*, **37**, 321-326.

Grummon, D. S., LaGrange, T. (2000), *Proc. SMST-2000*, Shape-Memory and Superelastic Technologies, Asilomar California, April 31, 2000.

Haque, M.A., Saif, M.T.A. (2002), Mechanical behavior of 30–50 nm thick aluminum films under uniaxial tension, *Scripta Mater.* **47**, 863-867.

HASYLAB (2003), www-hasyllab.desy.de

Hauk, V. (1998), Structural and residual stress analysis by nondestructive methods, Amsterdam, Elsevier.

He, Y., Schwarz, R.B., Migliori, A., Whang, S.H. (1995), Elastic constants of single crystal gamma-TiAl, *J. Mater. Res.*, **10** No.5, 1187-95.

Hommel, M., Kraft, O. (2001), Deformation behavior of thin copper films on deformable substrates, *Acta Mater.* **49**, 3935-47.

Hutchinson, J.W. (1970), Elastic-plastic Behaviour of Polycrystalline Metals and Composites, *Proc. Roy. Soc. Lond.*, **A319**, 247 (as cited in Clausen (1997)).

Inkson, B. J., Clemens, H. (1999), Microstructure of rolled Ti-46.5Al-4(Cr, Nb, Ta, B), *Mater. Res. Soc. Symp. Proc.* **552**, KK3.12.1-6.

Jiang, A., Yohannan, A., Nnolim, N.O., Tyson, T.A., Axe, L., Lee, S.L., Cote, P. (2003), Investigation of the structure of β -tantalum, *Thin Solid Films*, **437**, 116–122.

Kampmann, R., Lippmann, T., Burmester, J., dos Santos, J. F., Franz, H., Haese-Seiller, M., Marmotti, M. (2001), Upgrading of the PETRA-2 beamline at HASYLAB for materials science analyses, *Nuc. Inst. and Meth. Phys. Res. A*, **467-468**, 1261-1264.

Kang, Y.S., Ho, P.S., Knipe, R., Tregilgas, J. (1997), Film thickness effect on tensile properties and microstructures of submicron aluminum thin films on polyimide, *Mater. Res. Soc. Symp. Proc.*, **436**, 35-40.

Keller, R.-M., Baker, S.P., Arzt, E. (1998), Quantitative analysis of strengthening mechanisms in thin Cu films: Effects of film thickness, grain size, and passivation, *J. Mater. Res.*, **13**, 1307-17.

Kelly, A., Groves, G.W. (1970), Crystallography and Crystal defects, Longmans, New York (as cited in Wieder, (1997)).

Kockelmann, H., Schwarz, T. (1993), Die Bohrlochmethode - ein für viele Anwendungsbereiche optimales Verfahren zur experimentellen Ermittlung von Eigenspannungen, *MTB HBM* **29**, **2**, 33-38.

Kolodner, P. (2002), Optical Fiber Communications (OFC 2002), www.lucent.com/livellink/0900940380008740_Technical_material.PDF.

- Korsunsky, A.M., Wells, K.E., Withers, P.J. (1998), Mapping two-dimensional state of strain using synchrotron X-ray diffraction, *Scripta Materialia*, **39**, 1705-1712.
- Kraft, O., Hommel, M., Arzt, E. (2000), X-ray diffraction as a tool to study the mechanical behaviour of thin films, *Mater. Sci. Eng.*, **A288**, 209-216.
- Kretschmann, A., Kuschke, W.-M., Baker, S. P., Arzt, E. (1997), Plastic Deformation of Thin Copper Films Determined by X-Ray Microtensile Tests, *Mater. Res. Soc. Symp. Proc.*, **436**, 59-64.
- Kröner, E. (1958), *Kontinuumstheorie der Versetzungen und Eigenspannungen* - Berlin: Springer.
- Kuhlmann, U., Rink J. (1998), Terabytes in Plastikfolie, *c't Magazin für Computertechnik*, **3**, 18.
- Kuschke, W.M., Arzt, E. (1994), Investigation of the stresses in continuous thin films and patterned lines by x-ray diffraction, *Appl. Phys. Lett.*, **64**, 1097-99.
- von Laue, M. (1962), *Röntgenstrahlinterferenzen*, Akademie Verlag, Berlin (1962).
- Leung, O. S., Munkholm, A., Brennan, S., Nix, W. D. (2000), A search for strain gradients in gold thin films on substrates using x-ray diffraction, *J. Appl. Phys.*, **88** No.3, 1389-1396.
- Liss, K.-D., Bartels, A., Schreyer, A., Clemens, H. (2003), High Energy X-Rays: A Tool for Advanced Bulk Investigations in Materials Science and Physics, Textures and Microstructures, *Textures and Microstructures*, **35** No.3/4, 219-252.
- Lorentzen, T., Faurholdt, T., Clausen, B., Danckert, J. (1998), Characterization of Residual Stresses Generated During Inhomogeneous Plastic Deformation, *J. of Strain Analysis*, **33** No.3, 243-252.
- Lu, W.J., Zhang, D., Zhang, X.N., Wu, R.J., Sakata, T., Mori, H. (2001), Microstructure and tensile properties of in situ (TiB+TiC)/Ti6242 (TiB:TiC=1:1) composites prepared by common casting technique, *Mat. Sci. Eng. A*, **311**, 142-150.
- Lysak, M., Gumbsch, P., Wanner, A. (2001), Besonderheiten der Schallemission bei der plastischen Verformung der intermetallischen Phase NiAl, in "13. Kolloquium Schallemission", DGZfP-Berichtsband BB78, (DGZfP), Berlin, 89-100.
- Macherauch, E., Kloos, K.H. (1986), *Residual Stresses in Science and Technology 1*, **3**.
- Marmotti, M., Burmeister, J., Haese-Seiller, M., Kampmann, R. (2002), Two-dimensional position-sensitive detectors for high resolution diffraction with neutrons and high energy synchrotron radiation, *Nuclear Instruments and Methods in Physics Research A*, **477**, 347-352.

- Mecking, H., Hartig, C., Kocks, U. (1996), Deformation Modes in Gamma-TiAl as Derived from the Single Crystal Yield Surface, *Acta Mater.*, **44**, 1309-21.
- Miracle, D.B. (1993), The physical and mechanical properties of NiAl, *Acta metall. mater.*, **41**, 649-684.
- Nix, W.D. (1989), Mechanical properties of thin films, *Metall. Trans.*, **20A**, 2217-2245.
- Nix, W.D. (1998), Yielding and strain hardening of thin metal films on substrates, *Scripta Mater.*, **39**, 545-554.
- Noyan, I.C., Cohen, J.B. (1987), Residual Stress: Measurement by Diffraction and Interpretation, New York, NY, Springer, p. 117.
- Noyan, I.C., Sheikh, G. (1992), X-ray tensile testing of thin films, *J. Mater. Res.*, **8**, 764.
- Plansee AG (2003), www.plansee.com.
- Pyzalla, A., Reimers, W., Liss, K.-D. (2000), A Comparison of Neutron and High Energy Synchrotron Radiation as Tools for Texture and Stress Analysis, *Materials Science Forum*, **347-349**, 34-39.
- Pyzalla, A., Jacques, A., Feiereisen, J.-P., Buslaps, T., d'Almeida, T., Liss, K.-D., In - situ Analyses of the Microstraons during Tensile Deformation of an AlSi-MMC at Room Temperature and Elevated Temperature, *Journal of Neutron Research*, **9**, 435-442.
- Renault, P.-O., Badawi, K.F., Bimbault, L., Goudeau, Ph., Elkaim, E., Lauriat, J. (1998), Poisson's ratio measurement in tungsten thin films combining an x-ray diffractometer with in situ tensile tester, *Appl. Phys. Lett.*, **73**, 1952-54.
- Reuss, A. (1929), Berechnung der Fließgrenze von Mischkristallen auf Grund der Plasticitätsbedingung für Einkristalle, *Z. angew. Math. Mech.*, **9**, 49-54.
- Röntgen, W.C. (1895), *Würzburg Physical and Medical Society*, Translated by Arthur Stanton, On a new kind of rays, *Nature* **53** (1896), 274-276.
- Royer, A., Jacques, A., Bastie, P., Veron, M. (2001), The evolution of the lattice parameter mismatch of nickel based superalloy: an in situ study during creep deformation, *Mat. Sci. and Eng. A*, **A319-321**, 800-804.
- Rusović, N., Warlimont, H. (1977), The elastic behaviour of β_2 -NiAl alloys, *Phys. stat. sol. A*, **44**, 609-619.
- Sachs, G. (1928), Zur Ableitung einer Fließbedingung, *Z. Ver. Deu. Ing.*, **72**, 734 (as cited in Clausen (1997)).
- Saif, M.T.A., Zhang, S., Haque, A., Hsia, K.J. (2002), Effect of Native Oxide on the Elastic Modulus of Nanoscale Aluminum Films, *Acta Mater.*, **50**, 2779-2786.

- Sanchez Jr, J.E., Arzt, E. (1992), Effects of grain orientation on hillock formation and grain growth in aluminum films on silicon substrates, *Scripta Metall. et Mater.*, **27**, 285-290.
- Spolenak, R., Tamura, N., Valek, B.C., MacDowel, A.A., Celestre, R.S., Padmore, H.A., Brown, W.L., Marieb, T., Batterman, B.W., Patel, J.R. (2002), High resolution microdiffraction studies using synchrotron radiation, *American Institute of Physics Conference Proceedings*, **612**, 217-228.
- Tanaka, K. (2003), Kyoto University, Japan, unpublished data.
- Taylor, G.I. (1938), Plastic Strain in Metals, *J. Inst. Metals*, **62**, 307 (as cited in Clausen (1997)).
- Thompson, C.V. (1990), Grain Growth in Thin Films, *A. Rev. Mater. Sci.*, **20**, 245-268.
- Thompson, C. V. (1993), The yield stress of polycrystalline thin films, *J. Mater. Res.*, **8** No.2, 237-238.
- Thompson, A., Vaughan, D. (2003), X-ray Data Booklet, xdb.lbl.gov.
- Thompson, C. V., Carel, R. (1995), Texture Development in Polycrystalline Thin Films, *Mater. Sci. Eng.*, **B32**, 211-219.
- Timoshenko, S., Goodier, J. N. (1951). *Theory of Elasticity*, second edition. New York: McGraw-Hill Book Company, Inc.
- Tregilgas, J.H., Strumpell, M. (1998), Tensile testing of ultra-thin-film materials deposited on polyimide for MEMS applications, *Mater. Res. Soc. Sympos. Proc.*, **518**, 179-184.
- Venkatraman, R., Bravman, J. C. (1992), Separation of film thickness and grain boundary strengthening effects in Al thin films on Si, *J. Mater. Res.*, **7** No.8, 2040-48.
- Voigt, W. (1928), *Lehrbuch der Kristallphysik*, Teubner, Berlin.
- Wanner, A., Dunand, D.C. (2000), Synchrotron X-Ray Study of Bulk Lattice Strains in Externally-Loaded Cu-Mo Composites, *Met. Mat. Trans. A*, **31A**, 2949-62.
- Wanner, A., Dunand, D.C. (2001), Methodological aspects of the high-energy synchrotron X-ray diffraction technique for internal stress evaluation, *J. Neutron Res.*, **9**, 495-501.
- Wanner, A., Schietinger, B., Bidlingmaier, T., Zalkind, H., Arzt, E. (1995), Monitoring of Deformation Induced Microcracking in Polycrystalline NiAl, *Mat. Res. Soc. Symp. Proc.*, **364**, 543-548.
- Wcislak, L., Klein, H., Bunge, H.J., Garbe, U., Tschentscher, T., Schneider, J.R. (2002), Texture analysis with high-energy synchrotron radiation, *Journal of Applied Crystallography*, **35** No.1, 82-95.

Welzel, U. (2002), Diffraction Analysis of Residual Stress; Modelling Elastic Grain Interaction, Ph.D. thesis, Bericht Nr. 124, Max-Planck-Institut für Metallforschung Stuttgart und Universität Stuttgart.

Wieder, T. (1997), Realstrukturaufklärung polykristalliner dünner Schichten mittels Röntgenbeugung, Habilitationsschrift, FB Materialwissenschaft, TH Darmstadt, Kassel University Press. <http://www.upress.uni-kassel.de>.

Appendix

10.1 Appendix A – Elastic Constants for <111> Fiber Textured Au and Cu

For a cubic material exhibiting a perfect <111> fiber texture the relationship between the elastic constants in specimen coordinates and the elastic constants in crystal coordinates can be obtained by coordinate transformation (Besser et al. (1994)). The results are:

$$C'_{11} = \frac{C_{11} + C_{12} + 2C_{44}}{2}, \quad (10.1a)$$

$$C'_{12} = \frac{C_{11} + 5C_{12} + 2C_{44}}{6} \quad (10.1b)$$

$$C'_{13} = \frac{C_{11} + 2C_{12} - 2C_{44}}{3} \quad (10.1c)$$

$$C'_{15} = \frac{C_{11} - C_{12} - 2C_{44}}{\sqrt{3}\sqrt{6}} \quad (10.1d)$$

$$C'_{25} = \frac{-C_{11} + C_{12} + 2C_{44}}{\sqrt{3}\sqrt{6}}, \quad (10.1e)$$

$$C'_{33} = \frac{C_{11} + 2C_{12} + 4C_{44}}{3}, \quad (10.1f)$$

$$C'_{44} = \frac{C_{11} - C_{12} + C_{44}}{3}, \quad (10.1g)$$

$$C'_{46} = \frac{-C_{11} + C_{12} + 2C_{44}}{\sqrt{3}\sqrt{6}}, \quad (10.1h)$$

$$C'_{66} = \frac{C_{11} - C_{12} + 4C_{44}}{6}. \quad (10.1i)$$

The single-crystal elastic constants of Au in crystal coordinates are $C_{11} = 186$ GPa, $C_{12} = 157$ GPa, and $C_{44} = 42$ GPa (Goens and Weerts (1936)). The stiffness and compliance matrices of a <111>-textured polycrystalline Au film in sample coordinates are thus

$$C'_{ij} = \begin{pmatrix} 214 & 148 & 139 & 0 & -13.0 & 0 \\ 148 & 214 & 139 & 0 & 13.0 & 0 \\ 139 & 139 & 223 & 0 & 0 & 0 \\ 0 & 0 & 0 & 23.7 & 0 & 13.0 \\ -13.0 & 13.0 & 0 & 0 & 23.7 & 0 \\ 0 & 0 & 0 & 13.0 & 0 & 32.8 \end{pmatrix} \text{GPa},$$

and

$$S'_{ij} = \begin{pmatrix} 12.4 & -7.06 & -3.30 & 0 & 10.6 & 0 \\ -7.06 & 12.4 & -3.30 & 0 & -10.6 & 0 \\ -3.30 & -3.30 & 8.60 & 0 & 0 & 0 \\ 0 & 0 & 0 & 53.9 & 0 & -21.3 \\ 10.6 & -10.6 & 0 & 0 & 53.9 & 0 \\ 0 & 0 & 0 & -21.3 & 0 & 38.9 \end{pmatrix} \text{TPa}^{-1}.$$

The single-crystal elastic constants of Cu in crystal coordinates are $C_{11} = 168$ GPa, $C_{12} = 121$ GPa, and $C_{44} = 75$ GPa (Goens and Weerts (1936)). The stiffness and compliance matrices of a $\langle 111 \rangle$ -textured polycrystalline Cu film in sample coordinates are thus

$$C'_{ij} = \begin{pmatrix} 220 & 104 & 86.6 & 0 & -24.2 & 0 \\ 104 & 220 & 86.6 & 0 & 24.2 & 0 \\ 86.6 & 86.6 & 237 & 0 & 0 & 0 \\ 0 & 0 & 0 & 40.7 & 0 & 24.2 \\ -24.2 & 24.2 & 0 & 0 & 40.7 & 0 \\ 0 & 0 & 0 & 24.2 & 0 & 57.8 \end{pmatrix} \text{GPa},$$

and

$$S'_{ij} = \begin{pmatrix} 7.69 & -3.84 & -1.41 & 0 & 6.87 & 0 \\ -3.84 & 7.69 & -1.41 & 0 & -6.87 & 0 \\ -1.41 & -1.41 & 5.26 & 0 & 0 & 0 \\ 0 & 0 & 0 & 32.8 & 0 & -13.8 \\ 6.87 & -6.87 & 0 & 0 & 32.8 & 0 \\ 0 & 0 & 0 & -13.8 & 0 & 23.1 \end{pmatrix} \text{TPa}^{-1}.$$

10.2 Appendix B – Stiffness- and Compliance Matrices for the Hexagonal and Tetragonal Lattice

For all classes of the hexagonal lattice, the stiffness matrix has the following form:

$$C_{ij} = \begin{pmatrix} C_{11} & C_{12} & C_{13} & 0 & 0 & 0 \\ C_{13} & C_{11} & C_{13} & 0 & 0 & 0 \\ C_{13} & C_{13} & C_{33} & 0 & 0 & 0 \\ 0 & 0 & 0 & C_{44} & 0 & 0 \\ 0 & 0 & 0 & 0 & C_{44} & 0 \\ 0 & 0 & 0 & 0 & 0 & \frac{1}{2}(C_{11} - C_{12}) \end{pmatrix}. \quad (10.2)$$

For the tetragonal lattice, the stiffness matrix has the following form (classes $4mm$, $42m$, 422 , $4/mmm$):

$$C_{ij} = \begin{pmatrix} C_{11} & C_{12} & C_{13} & 0 & 0 & 0 \\ C_{13} & C_{11} & C_{13} & 0 & 0 & 0 \\ C_{13} & C_{13} & C_{33} & 0 & 0 & 0 \\ 0 & 0 & 0 & C_{44} & 0 & 0 \\ 0 & 0 & 0 & 0 & C_{44} & 0 \\ 0 & 0 & 0 & 0 & 0 & C_{66} \end{pmatrix}. \quad (10.3)$$

10.3 Appendix C – Angle between two directions for the hexagonal lattice

The angle between two directions $[h_1, h_2, h_3]$ and $[l_1, l_2, l_3]$ for the hexagonal lattice with the lattice constants a and c is given by the following relationship:

$$\cos \alpha = \frac{h_1 l_1 + h_2 l_2 + \frac{1}{2}(h_1 l_2 + l_1 h_2) + \frac{3}{4}(a/c)^2 h_3 l_3}{\sqrt{h_1^2 + h_2^2 + h_1 h_2 + (3/4)(a/c)^2 h_3^2} \sqrt{l_1^2 + l_2^2 + l_1 l_2 + (3/4)(a/c)^2 l_3^2}} \quad (10.4)$$

10.4 Appendix D – Calibration Procedure for $\sin^2\psi$ Measurements

The calibration powder embedded in vacuum grease was applied to the reverse side of the substrate to convert positions on the camera screen into diffraction angles and to compensate for sample positioning errors. The calibration layer and the thin film are separated by the 125 μm thick polyimide substrate. Thus the relative positions of the peak maxima on the camera screen must be corrected. The film thickness can be neglected which may not be the case for the thickness of the calibration substance. Assuming that the Au layer is located in the rotation centre of the diffractometer, only the positions of the calibration rings must be shifted accordingly. The effective distance Δx between the scattering centre of the W powder and the thin film is a function of the inclination angle α :

$$\Delta x = \frac{125 \mu\text{m}}{\sin \alpha}, \quad (10.5)$$

This leads to a displacement of the calibration ring Δc on the camera depending on the Bragg-angle θ_{cal} of the considered calibration ring and the camera angle δ :

$$\Delta c = \frac{\Delta x \cdot \sin 2\theta_{cal}}{\cos(\delta - 2\theta_{cal})}, \quad (10.6)$$

Since the microtensile tester was not built symmetrically, the whole apparatus had to be rotated in order to perform $\sin^2\psi$ measurements. During this rotation the calibration substance is either located up- or downstream with respect to the substrate. Thus the displacement Δc has to be added or subtracted from the original position.

The corrected positions of both calibration peaks can be used to determine the sample-to-detector distance L . Both the determination of L and the evaluation of the Bragg-angle of the film θ_s are made in the plane which is defined by the loading axes and the primary beam. Within this plane L can be obtained by geometric considerations and the positions of the peak maxima of the two calibration peaks x_{cal1} and x_{cal2} , their Bragg-angles $\theta_{cal1,2}$ ($\theta_{cal1} < \theta_{cal2}$) as well as the camera angle δ can be calculated. All parameters are can be found in Table 5 on page 62. In the case of the Au films, one obtains for the sample-to-detector distance L :

$$L = \frac{(x_{cal1} - x_{cal2}) \cdot \cos(2\theta_{cal2} - \delta) \cdot \cos(\delta - 2\theta_{cal1})}{\sin(2\theta_{cal2} - 2\theta_{cal1})}, \quad (10.7)$$

In the same way the Bragg-angle of the sample layer θ_s can be calculated from the position of the sample peak x_s and the detector distance L :

$$2\theta_s = \delta - \arctan\left(\tan(\delta - 2\theta_{cal1}) + \frac{x_{cal1} - x_s}{L}\right). \quad (10.8)$$

After determining θ_s for all inclination angles ψ , the corresponding lattice spacings d_ψ can be calculated using Bragg's Equation (2.14). The d_ψ values obtained by this procedure are finally the basis for residual stress analysis using the $\sin^2\psi$ method.

10.5 Appendix E – Selected IDL 6.0 routines

File – I/O for reading RAW files as recorded by the MAR CCD camera and the MAR area detector:

```
filename = DIALOG_PICKFILE(/READ, /MULTIPLE_FILES, GET_PATH=pfad) ; file request
OPENR, 1, filename[i] ; open RAW file
    PICSIZE = 2048 ; ANKA marCCD files
    frame = UINTARR(2048, 2048, /NOZERO) ; frame is stored in an unsigned integer array
    header = BYTARR(2, 2048, /NOZERO) ; file header is stored in a byte array
    READU, 1, header ; read header
    READU, 1, frame ; read whole frame
CLOSE, 1 ; close file
TVSCL, frame ; show frame in actual display
```

Polar rebinning routine:

```
sinus = dblarr(1601)
cosinus = dblarr(1601)
ws = 0
we = 1600

FOR winkel = ws, we, 1 DO BEGIN
    sinus(winkel) = Double(sin(!dpi*winkel/800.00))
    cosinus(winkel) = Double(cos(!dpi*winkel/800.00))
ENDFOR

REPEAT BEGIN
if reseti eq 1 then exitloop = 1
FOR winkel = ws, we, 1 DO BEGIN
```

```

FOR RStep = 0, 400, 1 DO BEGIN
  Rx = (Rminn + RStep * Rinkrem) * cosinus(winkel)
  X1pos = Xcenter + Rx
  Ry = (Rminn + RStep * Rinkrem) * sinus(winkel)
  If (X1pos(0) LT (picsize-1) and X1pos(0) GT 0.00) then begin
    Y1pos = Ycenter + Ry
    if (Y1pos(0) LT (picsize-1) and Y1pos(0) GT 0.00) then begin
      Radialbild(Rstep,winkel) = bild(X1pos(0)+0.5,Y1pos(0)+0.5)
    endif
  endif
ENDIFOR
ENDFOR

```

Perform radial Gaussian peak fits:

```

FOR w = ws, we, 1 DO BEGIN
  profil1 = Radialbild[0:400,w,*]
  result1 = GAUSSFIT (X, profil1, A1, NTERMS=3)
  profil2 = Radialbild[0:400,(w+800) MOD 1600,*]
  result2 = GAUSSFIT (X, profil2, A2, NTERMS=3)
  if (A1[1]*Rinkrem(0)+Rminn(0)+A2[1]*Rinkrem(0)+Rminn(0)) gt 2*Rminn(0) and
    (A1[1]*Rinkrem(0)+Rminn(0)+A2[1]*Rinkrem(0)+Rminn(0)) lt 2*Rmaxx(0) then begin
    wcounter = wcounter + 1
    writeu, 1, string(0.225*w, A1[0]), string(A1[2]*Rinkrem(0)), string(A1[1]*Rinkrem(0)+Rminn(0)),
      string(A1[1]*Rinkrem(0)+Rminn(0)+A2[1]*Rinkrem(0)+Rminn(0)),
      string(sin(0.225*w*!PI/180)^2),STRING([10B])

    resultarray[wcounter,0] = 0.225*w
    resultarray[wcounter,1] = A1[0]
    resultarray[wcounter,2] = A1[2]*Rinkrem(0)
    resultarray[wcounter,3] = A1[1]*Rinkrem(0)+Rminn(0)
    resultarray[wcounter,4] = A1[1]*Rinkrem(0)+Rminn(0)+A2[1]*Rinkrem(0)+Rminn(0)
    resultarray[wcounter,5] = sin(0.225*w*!PI/180)^2
  endif
ENDIFOR

```

11 Deutsche Zusammenfassung

11.1 Grundlagen

11.1.1 Grundlagen der röntgenographischen Spannungsmessung

Spannungen, die aufgrund makroskopischer Ursachen entstehen, werden Spannungen vom Typ-I genannt. Dies können Spannungen in einem Bauteil sein, die von der Oberflächenbehandlung oder der thermischen Behandlung herrühren, oder auch Spannungen in dünnen Schichten, die durch Kornwachstum während der Auslagerung verursacht werden. Kohärenzspannungen in epitaktischen Schichten sind ein Spezialfall solcher Spannungen. Spannungen auf Kristallitebene werden Spannungen vom Typ-II genannt. Sie unterscheiden sich von Korn zu Korn aufgrund von Kornwechselwirkungen sowie Spannungsinhomogenitäten an den Korngrenzen. Aufgrund von elastischer Anisotropie weisen im Allgemeinen unterschiedlich orientierte Körner auch unterschiedliche Spannungen auf. Auf mikroskopischem Subkornlevel treten schließlich Spannungen vom Typ-III auf, die auf sich auf der Skala des Kristallgitters abspielen. Solche Spannungen werden von Kristalldefekten wie Versetzungen oder Punktdefekten verursacht.

Innere Spannungen werden zerstörungsfrei üblicherweise mit Beugungsmethoden gemessen. Solange alle dabei auftretenden Dehnungen im elastischen Bereich liegen, sind röntgenographische Spannungsmessungen möglich. In auf Seite 18 wird der Unterschied zwischen Makrodehnung und Gitterdehnung am Beispiel einer polykristallinen dünnen Schicht gezeigt. Die Gitterdehnung erhält man direkt aus der differenzierten Form der Bragg'schen Gleichung:

$$\varepsilon = \frac{\Delta d}{d_0} = -\cot\theta \cdot \Delta\theta, \quad (11.1)$$

Die auf die gesamte Probe wirkende Spannung nennt man Makrospannung; Spannungen, die eine Bragg Peak Verschiebung verursachen werden Mikrospannungen genannt.

Die Gitterdehnung für einen bestimmten Reflex hkl erhält man über die röntgenographisch gemessenen Netzebenenabstände $d_{\varphi\psi}$ nach folgender Beziehung:

$$(\varepsilon'_{33})_{\varphi\psi} = \frac{d_{\varphi\psi} - d_0}{d_0}, \quad (11.2)$$

wobei φ den Azimutwinkel und ψ den Kippwinkel der jeweiligen Netzebenen bezeichnet. Das dazugehörige Koordinatensystem ist in Figure 2.4 dargestellt. Der Index 0 steht dabei für den ungedehnten Ausgangszustand.

Durch geeignete Koordinatentransformation (siehe Gleichung (2.17) auf Seite 19) kann die im Laborkoordinatensystem gemessene Gitterdehnung ε'_{33} durch die Dehnungen im Probenkoordinatensystem ε_{ij} mit Hilfe folgender Gleichung beschrieben werden:

$$\begin{aligned} (\varepsilon'_{33})_{\varphi\psi} = & \varepsilon_{11} \cos^2 \varphi \sin^2 \psi + \varepsilon_{12} \sin 2\varphi \sin^2 \psi + \varepsilon_{22} \sin^2 \varphi \sin^2 \psi + \varepsilon_{33} \cos^2 \psi \\ & + \varepsilon_{13} \cos \varphi \sin 2\psi + \varepsilon_{23} \sin \varphi \sin 2\psi. \end{aligned} \quad (11.3)$$

Gleichung wird Fundamentalgleichung der röntgenographischen *Dehnungsmessung* genannt.

11.1.2 Biaxiale Eigenspannungsmessung – Die $\sin^2\psi$ Methode

Die $\sin^2\psi$ Methode wird üblicherweise zur röntgenographischen *Spannungsmessung* verwendet. Das Verfahren wird in dieser Arbeit zur Eigenspannungsmessung in metallischen Dünnschichten eingesetzt. Der Spannungstensor ist im Falle einer polykristallinen dünnen Schicht auf einem Substrat biaxial im Bereich der Gitterebenen, die durch den Röntgenstrahl erfasst werden. In diesem Fall verschwinden die Dehnungen mit den gemischten Indizes aus Gleichung , und mit Hilfe von Gleichung lässt sich folgender Zusammenhang zwischen dem Netzebenenabstand d und den Kippwinkel ψ der jeweiligen Netzebenen bestimmen:

$$d_{\psi} = d_0 \left((\varepsilon'_{33})_{\psi} + 1 \right) = d_0 (\varepsilon_{11} - \varepsilon_{33}) \sin^2 \psi + d_0 (\varepsilon_{33} + 1), \quad (11.4)$$

Wobei d_0 wieder den ungedehnten Gitterparameter bezeichnet.

Aus Gleichung ist ersichtlich, dass alle auftretenden Dehnungen unabhängig vom Azimutwinkel φ sind. Gleichung hat weiterhin die Form einer Geradengleichung $d_{\psi} = m \sin^2 \psi + b$, wobei man die beiden Parameter m und b durch Auftragen von d_{ψ} gegen $\sin^2\psi$ erhält. Diese Auftragung gab der $\sin^2\psi$ Methode ihren Namen.

Im äquibiaxialen Fall gilt weiterhin $\varepsilon_{11} = \varepsilon_{22}$, und es lässt sich mit Hilfe des Hooke'schen Gesetzes, das die gemessenen Dehnungen mit den Spannungen verknüpft, folgende Gleichung zur Bestimmung des äquibiaxialen Eigenspannungszustandes herleiten (siehe Gleichung (2.23) und (2.24a-d)):

$$\sigma_{11} = \sigma_{22} = \frac{(C'_{12} + C'_{13})C'_{33} + 2C'^2_{13}}{2C'_{13} + C'_{33}} (\epsilon_{11} - \epsilon_{33}) \approx \frac{(C'_{12} + C'_{13})C'_{33} + 2C'^2_{13}}{2C'_{13} + C'_{33}} \frac{m}{b}. \quad (11.5)$$

C_{ij} bezeichnet die elastischen Konstanten des zu untersuchenden Materials, C'_{ij} steht für die röntgenographischen elastischen Konstanten im transformierten Koordinatensystem, und $\sigma_{11} = \sigma_{22}$ bezeichnet schließlich die äquibiaxiale Spannung. Da lediglich das Verhältnis m/b in die Berechnung der Spannungen eingeht, ist eine genaue Kenntnis des ungedehnten Gitterparameters d_0 nicht nötig, da das Spannungsergebnis nach Gleichung durch die Quotientenbildung in Gleichung unabhängig von d_0 ist.

Die $\sin^2\psi$ Methode ist eine etablierte Methode zur Messung des äquibiaxialen Eigenspannungszustands in einer frisch abgeschiedenen Schicht. Um die biaxiale Spannungsentwicklung während eines Zugversuchs zu charakterisieren müssen $\sin^2\psi$ Messungen bei $\varphi = 0^\circ$ und $\varphi = 90^\circ$ durchgeführt werden, um sowohl in Längs- als auch in Querrichtung die gleiche Genauigkeit zu erreichen. Dadurch werden für jeden Azimutwinkel φ mindestens 6 unabhängige Messungen bei verschiedenen ψ Winkeln benötigt, wodurch diese Methode sehr zeitaufwendig wird und letztendlich nur sehr geringe Dehnraten im Zugversuch erreicht werden können.

11.1.3 Messung von Gitterdehnungen mit hochenergetischer Röntgenstrahlung

Um makroskopische inneren Spannungen (Typ-I Spannungen, siehe Kapitel 2.2.2) mit Beugungsmethoden zu messen, wird die Abweichung des gemessenen Gitterparameters vom Gitterparameter des spannungsfreien Materials bestimmt. Meistens sind die gemessenen makroskopischen Spannungen verbunden mit plastischer Verformung des Materials. Tritt Plastizität auf, sind die Beziehungen von Spannungen und Dehnungen im Allgemeinen nicht mehr linear. Ein solches Verhalten kann Hinweise auf das Vorhandensein von plastischer Anisotropie liefern, wenn für unterschiedliche hkl -Richtungen nichtlineare Beziehungen gefunden werden.

Um innere Spannungen in Vollmaterialien mit Röntgenmethoden messen zu können, wurden verschiedene Techniken entwickelt: Laue Beugungsmethoden wurden erfolgreich zur Messung an Einkristallen oder einzelnen Körnern mit Hilfe von fokussierten Mikroröntgenstrahlen angewandt [Biermann et al. (1997)]. Weiterhin wurden Debye-Scherrer

Beugungsmethoden entwickelt um über das Beugungsvolumen gemittelte Ergebnisse an polykristallinen Proben zu erhalten [Royer et al. (2001), Daymond and Withers (1996), Korsunsky et al. (1998)]. Eine interessante Methode wurde von Wanner and Dunand (2000) etabliert, bei der die Probe mit hochenergetischem, monochromatischem Röntgenlicht durchstrahlt wird und kontinuierliche Debye-Scherrer Ringe mit einem hochauflösenden Flächendetektor aufgenommen werden. Die Gitterdehnungen erhält man anschließend durch Analyse der elliptischen Verzerrung dieser Beugungsringe während der Probenverformung. Dieses Verfahren ermöglicht die experimentelle Messung von Spannungsumlagerungen in mehrphasigen Materialien und kann eine Vielzahl von neuen Erkenntnissen über die Mikromechanik während der Verformung liefern.

11.2 Methodik

11.2.1 Spannungsentwicklung in Vollmaterialien – Die Hochenergie- $\sin^2\varphi$ Methode

Von Daymond und Withers (1996) wurde der erste typische experimentelle Versuchsaufbau zur Messung von Gitterdehnungen beschrieben, bei dem hochenergetische Röntgenstrahlung unter senkrechtem Einfall die Probe durchstrahlt und die Verzerrung von Debye-Scherrer Ringen analysiert wird. Die Gitterdehnungen erhält man dabei gemittelt über das gesamte durchstrahlte Probenvolumen in der Ebene senkrecht zum einfallenden Röntgenstrahl. Der Versuchsaufbau ist auf Seite 27 in Figure 3.1 schematisch dargestellt. In Figure 3.2 sind typische Debye-Scherrer Beugungsringe gezeigt, wie sie mit einem hochauflösenden Flächendetektor aufgenommen werden. Zunächst werden die Beugungsringe indiziert und die ungefähren Ringdurchmesser über den Abstand von Probe zur Kamera ermittelt. Anschließend wird der Mittelpunkt über horizontale und vertikale Linienprofile ermittelt. Von diesem Mittelpunkt ausgehend wird nun ein genügend breiter Streifen um einen gesamten Beugungsring gewählt, der keinen Überlapp mit anderen Ringen gewährleistet. Innerhalb dieses Streifens werden nun in radialer Richtung Intensitätsprofile für jeden azimutalen Winkel bestimmt und die Lage des jeweiligen Peakmaximums über Gauß'sche Peakpassung bestimmt. Zuletzt werden für jeweils gegenüberliegende Azimutwinkel die Ringdurchmesser aus den Ringradien berechnet. Trägt man nun die so erhaltenen Durchmesser gegen das Sinusquadrat des Azimutwinkels ($\sin^2\varphi$) auf, erhält man Punkte, die auf einer Geraden liegen. Extrapolation nach $\sin^2\varphi = 0$ bzw. $\sin^2\varphi = 1$ liefert die Ringdurchmesser in Longitudinal-

bzw. Transversalrichtung. Die Änderung der Gitterdehnungen kann nun nach Gleichung (2.15) auf Seite 17 über die so erhaltenen Ringdurchmesser berechnet werden.

Der größte Nachteil dieser "klassischen" $\sin^2\varphi$ Methode ist, dass sie nur für sehr feinkörnige polykristalline Materialien verwendet werden kann, da sehr viele einzelne Kristallite die Beugungsbedingung erfüllen müssen, um einen möglichst glatten und kontinuierlichen Beugungsring zu erhalten. Ein weiterer Nachteil ist die starke Empfindlichkeit des Verfahrens gegen unerwünschte Probenbewegungen entlang der Richtung des einfallenden Röntgenstrahls. Solche Probenbewegungen wirken sich unmittelbar auf die Beugungsringdurchmesser aus und stellen die Hauptfehlerquelle der Methode dar. Zur Kompensation ist daher eine auf die Probe aufgebrachte Kalibriersubstanz, die nicht mit der Probe gedehnt wird, unabdingbar.

Vergrößerter Versuchsaufbau

In dieser Arbeit wurde den Überlegungen von Wanner and Dunand (2001) folgend eine neue $\sin^2\varphi$ Methode entwickelt und experimentell umgesetzt, bei der diese Einschränkungen wegfallen. Die Strategie beruht dabei auf einer Vergrößerung des gesamten Versuchsaufbaus um ungefähr eine Größenordnung bei gleicher Probengeometrie (siehe auf Seite 29). Im Wesentlichen wird dabei der Abstand von Probe zu Detektor erheblich verlängert, wodurch die Durchmesser der Beugungsringe ebenfalls vergrößert werden. Der Messeffekt, d.h. die elliptische Verzerrung der Ringe bei Anlegen einer äußeren Dehnung, wird dadurch ebenfalls größer und die Empfindlichkeit für kleine Probenbewegungen entlang der Strahlachse somit geringer. Das Verhältnis von Ringbreite zu Ringdurchmesser bestimmt weiterhin die Genauigkeit, mit der die elliptische Verzerrung analysiert werden kann. Schmale Beugungsringe sind daher vorteilhaft zur Bestimmung der exakten Lage der Peakmaxima. Da die Ringbreiten hauptsächlich durch den Strahlquerschnitt des Primärstrahls vorgegeben werden, ist dafür in möglichst feiner Röntgenstrahl notwendig. Mit solch einem feinen Strahl lässt sich allerdings nur ein sehr kleines Beugungsvolumen erfassen, wodurch sich nur sehr wenige Einzelkristallite in Beugungsbedingung befinden. Man erhält dann keine kontinuierlich durchgehenden Debye-Scherrer Ringe sondern "gefleckte" Ringe mit den jeweiligen Einzelreflexen. Um eine Dehnungsauflösung besser als 10^{-4} zu erreichen benötigt man jedoch eine ausreichende Kornstatistik, d.h. ausreichend viele Datenpunkte im $\sin^2\varphi$ Diagramm. Der Strahlquerschnitt des Primärstrahls sollte daher gerade so groß sein, dass man

möglichst glatte und kontinuierliche Debye-Scherrer Ringe erhält. Dies ist der Grund für die Limitierung auf sehr feinkörnige Materialien, da man den Strahlquerschnitt nicht beliebig groß machen kann, da sonst die Beugungsringe zu breit werden und die geringen elliptischen Verzerrungen nicht mehr analysierbar sind. Vergrößert man allerdings den Abstand von Probe zu Detektor, erhält man bei größerem Primärstrahlquerschnitt ein wesentlich besseres Verhältnis von Ringbreite zu Durchmesser, was letztendlich Experimente an grobkörnigeren Materialien ermöglicht.

Ein vergrößerter experimenteller Versuchsaufbau bedeutet daher eine Verlängerung des Abstandes von Probe zu Detektor, wodurch die Empfindlichkeit auf unerwünschte Probenbewegungen entlang der Richtung des Primärstrahls abnimmt, sowie eine Vergrößerung des Strahlquerschnitts, wodurch mehr Einzelkristallite in Beugungsbedingung gebracht werden. Durch das verbesserte Verhältnis von Ringbreite zu Durchmesser erhält man eine bessere Dehnungsauflösung und es können wesentlich grobkörnigere Materialien untersucht werden.

11.2.2 Spannungsentwicklung in ultradünnen Schichten – Die Niedrigenergie- $\sin^2\varphi$ Methode

In der vorliegenden Arbeit wurde ein neuer experimenteller Ansatz realisiert, wodurch es erstmals möglich ist die Entwicklung des vollständigen biaxialen Spannungszustands in dünnsten metallischen Schichten sehr schnell und effizient mit der $\sin^2\varphi$ Methode zu charakterisieren. Die metallischen Dünnschichten wurden nach einem etablierten Verfahren auf flexiblen Polyimid-Substraten mittels Magnetron-Sputtern abgeschieden. Schicht und Substrat wurden im uniaxialen Zugversuch gleichzeitig gedehnt, und die Spannungsentwicklung in der Schicht wird mittels Röntgenbeugung gemessen. Bisher wurden solche Experimente nach dem $\sin^2\psi$ -Verfahren an Labor-Röntgenquellen durchgeführt, das sehr gut für Schichtdicken im Mikrometerbereich funktioniert. Für erheblich dünnere Schichtdicken wurden die Zählzeiten durch Abnahme des Beugungsvolumens deutlich erhöht. Weiterhin erhielt man ein schlechtes Signal-zu-Rauschverhältnis, da die amorphe Struktur des Polyimids ein beträchtliches Hintergrundrauschen verursacht. Ergebnisse röntgenographischer Spannungsmessungen an dünnen Schichten in Verbindung mit *in situ* Zugversuchen lagen daher bisher nur für Schichtdicken größer als 300 nm vor. Um zu noch dünneren Schichtdicken vorzudringen, wurde in dieser Arbeit ein Verfahren entwickelt, das Gebrauch von drei Entwicklungen

macht, die in jüngster Zeit zur Verfügung stehen: (1) Synchrotronstrahlung mit hohem Fluss und einstellbarer Energie, (2) große, hochauflösende Flächendetektoren mit geringem Signalrauschen (3) Speicher- und Auswertekapazität für die großen Datenmengen, die solche Detektoren produzieren. Die Kombination aller drei Entwicklungen ermöglicht erstmals *in situ* Zugversuche im Schichtdickenbereich von nur wenigen Nanometern.

Für die $\sin^2\psi$ Methode ist eine Verkippung der Probe relativ zur Röntgenquelle und zum Detektor notwendig. Daher wurde dieses Verfahren nur zur Messung des äquibiaxialen Eigenspannungszustandes vor dem Zugversuch verwendet. Während des Zugversuchs kam das $\sin^2\phi$ Verfahren zum Einsatz, bei dem keine weiteren Absolutmessungen mehr durchgeführt werden. Die Änderung des biaxialen Spannungszustandes kann dann durch Aufnahme eines einzigen Debye-Scherrer Beugungsbildes charakterisiert werden. Dadurch kann der Zugversuch erheblich beschleunigt werden. Die überlegene Kornstatistik ermöglicht zudem eine sehr hohe Dehnungsauflösung.

Beim $\sin^2\phi$ Verfahren ist die Probe senkrecht zum einfallenden Primärstrahl orientiert, der die gesamte Probe durchdringt. Der experimentelle Aufbau ist in Figure 3.7 schematisch dargestellt. Dünne Metallschichten mit kubischem Kristallgitter weisen üblicherweise eine scharfe random-planare $\langle 111 \rangle$ Textur auf, was bedeutet, dass alle Körner (111) Netzebenen aufweisen, die senkrecht zum einfallenden Strahl orientiert sind, die einzelnen Körner allerdings zufällig innerhalb der Probenebene verdreht sind. Es stehen daher lediglich $\{\bar{1}11\}$ Netzebenen zur Röntgenbeugung zur Verfügung. Um konstruktive Interferenz zu erhalten, muss daher die Energie des Röntgenlichts exakt auf diese Textur eingestellt werden, um die Bragg-Bedingung zu erfüllen. Dies ist nur mit Synchrotronstrahlung möglich. Übliche Wellenlängen liegen im Niedrigenergiebereich zwischen 7 und 10 keV.

Durch die Verwendung von niedrigen Energien sind die Beugungswinkel relativ groß, was bedeutet, dass der Abstand von Probe zu Flächendetektor im Vergleich zur Hochenergie-Methode deutlich reduziert werden muss, damit vollständige Debye-Scherrer Ringe aufgenommen werden können. Dadurch wird die Verwendung einer Kalibriersubstanz zur Kompensation von Probenbewegungen während des Zugversuchs unvermeidbar. In

Vakuumm fett fein dispergiertes Wolframpulver hat sich für diesen Zweck als sehr geeignet herausgestellt.

11.3 Experimente

Die $\sin^2\varphi$ -Methode wurde bei Hochenergie-Experimenten an Vollmaterialproben sowie bei Niedrigenergie-Experimenten an dünnen Metallschichten eingesetzt. Die Hochenergie-Experimente wurden am Hamburger Synchrotronstrahlungslabor (HASYLAB) des Deutschen Elektronensynchrotrons (DESY) an den Beamlines BW5 und PETRA 2 durchgeführt. BW5 stand für den „konventionellen“ Versuchsaufbau mit relativ kurzem Abstand von Probe zu Detektor (~ 1 m) zur Verfügung. Dabei kam ein mar345 image-plate Detektor zum Einsatz. Der vergrößerte Versuchsaufbau (siehe Kapitel 3.1.2) konnte bei PETRA 2 mit einem Detektorabstand von ca. 7 m realisiert werden. Es wurden Messungen sowohl mit einem mar345 Detektor als auch mit zwei Drahtdetektoren gleichzeitig durchgeführt, wobei ein Detektor die Dehnungen in Longitudinal- und der zweite die Dehnungen in Transversalrichtung aufnahm. Es wurden folgende Materialien untersucht: (1) ein Cu/Mo Verbundwerkstoff, der zum Vergleich der Messungen mit früheren Arbeiten diente. (2) Ein Titan-Werkstoff, an dem die elastische Anisotropie untersucht wurde. (3) Eine NiAl-Superlegierung, bei der das Vorhandensein einer möglichen spannungsinduzierten Phasenumwandlung untersucht wurde. (4) γ -TiAl Legierungen, an denen die Spannungsumlagerungen sowohl bei Raumtemperatur als auch bei hohen Temperaturen (bis 800 °C) untersucht wurden. Die Hochtemperaturversuche wurden in Kooperation mit Dr. Alain Jacques von der École des Mines (Nancy, Frankreich) durchgeführt, der den Hochtemperatur-Zugofen zur Verfügung stellte. Dieser Ofen wurde bereits bei Spannungsmessungen an der Synchrotronstrahlungsquelle ESRF (Grenoble) unter Verwendung einer energiedispersiven Methode eingesetzt.

Die Niedrigenergie- $\sin^2\varphi$ Experimente an dünnen Metallschichten wurden an der Beamline des Max-Planck-Instituts für Metallforschung Stuttgart (MPI-MF) bei der Angströmquelle Karlsruhe (ANKA) im Forschungszentrum Karlsruhe (FZK) durchgeführt. Die Beugungsringe wurden dort mit einem hochauflösenden marCCD-Flächendetektor aufgenommen. Die dünnen Kupfer- und Goldschichten wurden auf 125 μm dicken Polyimidsubstraten (Kapton[®], DuPont) mittels UHV Magnetronspütern an der Zentralen

Wissenschaftlichen Einrichtung (ZWE) Dünnschichtlabor des Max-Planck-Instituts Stuttgart hergestellt. Die Schichten zeigen eine für kubische Metallschichten typische $\langle 111 \rangle$ Fasertextur. Es wurden Kupferschichten im Schichtdickenbereich von 20 – 640 nm sowie Goldschichten im Schichtdickenbereich von 20 – 1000 nm untersucht.

11.4 Ergebnisse

1. Die Messungen der Gitterdehnungen an Cu/Mo Verbundmaterialien, die am HASYLAB durchgeführt wurden, waren sehr reproduzierbar und vergleichbar mit denen, die von Wanner and Dunand (2000) mit einem anderen Setup an der Advanced Photon Source (APS) erhalten wurden.
2. Der Titanwerkstoff zeigte ein linear-elastisches Verhalten im ganzen untersuchten Dehnungsbereich. Aufgrund von elastischer Anisotropie wurden unterschiedliche Steigungen im Spannungs-Dehnungsdiagramm für verschiedene Debye-Scherrer Ringe erhalten. Die aus den elastischen Konstanten berechneten Steigungen stimmen gut mit den gemessenen Werten überein.
3. Mit einem vergrößerten Versuchsaufbau kann eine bessere Dehungsauflösung erreicht werden. Weiterhin wird ein wesentlich höheres Signal-zu-Rauschverhältnis für Minoritätsphasen erzielt. Dies konnte am Beispiel der Messungen an γ -TiAl experimentell gezeigt werden.
4. (001)-orientierte γ -TiAl Körner zeigen ein unterschiedliches Spannungs-Dehnungsverhalten bei Raumtemperatur und bei hohen Temperaturen. Bei hohen Temperaturen findet eine Abweichung vom linear-elastischen Verhalten bei wesentlich niedrigeren angelegten Spannungen statt als bei Raumtemperatur.
5. Eine spannungsinduzierte Phasenumwandlung bei NiAl wurde nicht gefunden. Außerdem wurde keinerlei Anzeichen von plastischer Anisotropie bei Raumtemperatur Druckversuchen gefunden.
6. *In situ* Röntgenzugversuche an stark fasertextureierten 20 nm dünnen Kupfer- und Goldschichten sind möglich mit der neuen Niedrigenergie- $\sin^2\varphi$ Methode. Dazu wird eine in der Energie einstellbare Synchrotronstrahlungsquelle mit hoher Brillianz sowie ein hochauflösender Flächendetektor benötigt.

7. Die Fließspannung dünner Goldschichten war konstant im Schichtdickenbereich von 80 nm bis 1000 nm. Unterhalb von 80 nm Schichtdicke wurde eine Abnahme der Fließspannung beobachtet.
8. Bei den Kupferdünnschichten wurde eine Spannungsabnahme oberhalb von 2.5% Gesamtdehnung gefunden. In diesem Bereich kam es zur Rissbildung in Proben mit Tantal-Zwischenschicht, die als Haftvermittler zwischen Kupfer und Polyimid sowie zur Ausbildung einer schärferen Fasertextur diente. Eine solche Zwischenschicht ist für Zugversuche bis zu hohen Gesamtdehnungen nicht geeignet.